BOSTON UNIVERSITY

SCHOOL OF MEDICINE

Dissertation

PREFRONTAL RHYTHMS FOR COGNITIVE CONTROL

by

JASON SHERFEY

B.E., Vanderbilt University, 2006

Submitted in partial fulfillment of the

requirements for the degree of

Doctor of Philosophy

2017

Approved by

First Reader _____

Nancy Kopell, Ph.D.
Professor of Mathematics and Statistics

Second Reader _____

Daniel Bullock, Ph.D.
Professor of Psychological and Brain Sciences

Third Reader _____

Helen Barbas, Ph.D.
Professor of Anatomy and Neurobiology

"Where I come from we say that rhythm is the soul of life, because the whole universe revolves around rhythm, and when we get out of rhythm, that's when we get into trouble."

- Babatunde Olatunji

"Great minds are related to the brief span of time during which they live as great buildings are to a little square in which they stand: you cannot see them in all their magnitude because you are standing too close to them."

- Arthur Schopenhauer

DEDICATION

I dedicate this thesis to my dearest, Natalie, for her love, support, and tolerance while I completed this work, to our joyous dog, Isis, and to my parents, Sharman and Steve, for bringing me into this world and encouraging me through everything.

ACKNOWLEDGMENTS

PREFRONTAL RHYTHMS FOR COGNITIVE CONTROL

JASON SHERFEY

Boston University School of Medicine, 2017

Major Professor: Nancy Kopell, Ph.D., Professor of Mathematics & Statistics

ABSTRACT

Goal-directed behavior requires flexible selection among action plans and updating behavioral strategies when they fail to achieve desired goals. Lateral prefrontal cortex (LPFC) is implicated in the execution of behavior-guiding rule-based cognitive control while anterior cingulate cortex (ACC) is implicated in monitoring processes and updating rules. Rule-based cognitive control requires selective processing while process monitoring benefits from combinatorial processing. I used a combination of computational and experimental methods to investigate how network oscillations and neuronal heterogeneity contribute to cognitive control through their effects on selective versus combinatorial processing modes in LPFC and ACC.

First, I adapted an existing LPFC model to explore input frequency- and coherence-based output selection mechanisms for flexible routing of rate-coded signals. I show that the oscillatory states of input encoding populations can exhibit a stronger influence over downstream competition than their activity levels. This enables an output driven by a weaker resonant input signal to suppress lower-frequency competing responses to stronger, less resonant (though possibly higher-frequency) input signals. While signals are encoded in population firing rates, output selection and signal routing can be governed independently by the frequency and coherence of oscillatory inputs and

their correspondence with output resonant properties. Flexible response selection and gating can be achieved by oscillatory state control mechanisms operating on input encoding populations. These dynamic mechanisms enable experimentally-observed LPFC beta and gamma oscillations to flexibly govern the selection and gating of rate-coded signals for downstream read-out. Furthermore, I demonstrate how differential drives to distinct interneuron populations can switch working memory representations between asynchronous and oscillatory states that support rule-based selection.

Next, I analyzed physiological data from the LeBeau laboratory and built a *de novo* model constrained by the biological data. Experimental data demonstrated that fast network oscillations at both the beta- and gamma frequency bands could be elicited *in vitro* in ACC and neurons exhibited a wide range of intrinsic properties. Computational modeling of the ACC network revealed that the frequency of network oscillation generated was dependent upon the time course of inhibition. Principal cell heterogeneity broadened the range of frequencies generated by the model network. In addition, with different frequency inputs to two neuronal assemblies, heterogeneity decreased competition and increased spike coherence between the networks thus conferring a combinatorial advantage to the network.

These findings suggest that oscillating neuronal populations can support either response selection (routing), or combination, depending on the interplay between the kinetics of synaptic inhibition and the degree of heterogeneity of principal cell intrinsic conductances. Such differences may support functional differences between the roles of LPFC and ACC in cognitive control.

TABLE OF CONTENTS

LIST OF TABLES

LIST OF FIGURES

LIST OF ABBREVIATIONS

β ....Beta-frequency (12-35Hz) population rhythm

γ.. Gamma-frequency (35-100Hz) population rhythm

ACC ....Anterior Cingulate Cortex

AMPA ....α-amino-3-hydroxy-5-methyl-4-isoxazolepropionic acid

BG ....Basal Ganglia

CB+..Calbindin-positive

CR+...Calretinin-positive

EEG...Electroencephalogram

FR.. Mean Firing Rate

FS ....Fast spiking

GABA .... γ-aminobutyric acid

gAHP.. .Slow afterhyperpolarizing potassium conductance

gCaN ....High-threshold N-type calcium conductance

gCaT...Low-threshold T-type calcium conductance

gKCa ....Calcium-dependent potassium conductance

gKDR, gK ....Fast delayed rectifier potassium conductance

gKs ....Slow (M-type) potassium conductance

gNaF, gNa .... .Fast sodium conductance

gNaP.. .Persistent sodium conductance

HH... Hodgkin-Huxley

iFR... Instantaneous Firing Rate

IN ....Interneuron

LFP..Local Field Potential

LIP...Lateral Intraparietal Cortex

LTS .... Low-Threshold Spiking

MUA .... Multi-Unit Activity

NMDA .... .N-methyl-D-aspartate

OFC..Orbitofrontal Cortex

PC.. Principal Cell

PFC ....Prefrontal Cortex

PMd.. Dorsal Premotor Cortex

PV+ ....Parvalbumin-positive

SOM+..Somatostatin-positive

STG .... Superior Temporal Gyrus

TRN..Thalamic Reticular Nucleus

WM ....Working Memory

CHAPTER 1

INTRODUCTION

"Experience without theory is blind, but

theory without experience is mere intellectual play."

(Immanuel Kant)

The mysteries of mind have intrigued and bewildered the most brilliant of thinkers through all ages. Scientific empiricism born of the enlightenment has deepened our appreciation for the complexity of those mysteries and at times, perhaps, brought us closer to understanding some limited aspects of them. We know the fluctuations of mind map onto processes in the brain and that the reproducibility of organized mental experience is supported by material mechanisms that all share by virtue of our common genome and developmental programs. The evolution of theories by dedicated researchers in psychology and neuroscience has provided those of us intrigued today with a conceptual framework for our modern inquiry, enabling us to go further and understand more with each generation. This dissertation is a modest attempt to contribute something to that profound body of work produced by thinkers seeking to understand thought.

Our limited understanding of the nature of mind and its relation to brain forces us to work with ideas from both domains and to make strong assumptions about their relation. A foundational assumption from cognitive neuroscience is that mental processes involve information processing and that information is encoded in neural activity.

Abundant evidence from the neurophysiology of sensory and motor systems suggests that the relevant activity encoding information is the rate of spiking in single or populations of neurons. At the same time, the neurophysiology of single neurons, networks of neurons, and large-scale neural systems reveals that neural processes at all scales exhibit periodic fluctuations indicative of oscillatory dynamics. Despite their ubiquity, the relationship between oscillatory dynamics and information processing remains a mystery.

My goal is to understand how rhythmic mechanisms in networks of neurons contribute to cognitively-important neural dynamics. In this dissertation, I will present a combination of experimental and computational modeling techniques to explore the effects of network oscillations on information processing during cognitive processes that direct behavior. In particular, I will describe how network oscillations affect microcircuit operations that select or combine information and map directly onto elementary cognitive operations. In one case, I will show how rhythms can facilitate the selective routing of information (Chapter 2). In a second case, I will show how neuronal heterogeneity disrupts that selectivity and can enable combinatorial processing of inputs from rhythmic networks (Chapter 3). The two cases will be related in terms of cognitive processes to which they contribute.

This chapter begins with an overview of the theories and experimental observations of cognitive control and neural oscillations that have motivated my work. That will be followed by a review of modeling traditions and particular models on which my work builds. The chapter will close with an overview of my approach, aims, and the remaining chapters of this dissertation.

1.1 Background

1.1.1 Cognitive control and prefrontal cortex

It is a remarkable fact that humans are able to achieve goals in the presence of a sea of distracting stimuli and a large repertoire of learned procedures that one could employ. From a cognitive perspective, task-relevant transient sensory information is selected by attention and stored in a short-term working memory (WM) buffer (Atkinson and Shiffrin, 1968). In addition to active maintenance of relevant information, WM involves a so-called central executive sub-system (Baddeley and Hitch, 1974) that governs cognitive control: the process of manipulating information for task-relevant processing while suppressing task-irrelevant distractors. Cognitive control includes processes like updating WM buffers, response inhibition, and task switching.

Dual process theories, in the conditioning literature, propose two processes compete to control our actions at all times (Evans, 2003; Evans, 2008; Gruber and McDonald, 2012): one that is automatic and based on well-learned habitual associations (Yin and Knowlton, 2006; Ashby et al., 2010) and another that is deliberative, goal-directed, and requires cognitive control. The latter is thought to benefit from rules: context-dependent mappings between input conditions and output responses. Rules are like sets of if-then statements selectively engaged to provide appropriate input-output mappings given a particular context. They represent flexible sets of lower-level associations (e.g., stimulus-response, action-outcome) engaged in service of executing higher-level goal-directed actions (Miller and Cohen, 2001; Dayan, 2008) and are

potentially involved in directing the decision making process itself (Dayan, 2007; Schouwenburg et al., 2012).

A wide range of neurophysiology, neuroimaging, and lesion studies have implicated lateral prefrontal cortex (LPFC) in maintenance (ventral LPFC) and cognitive control (dorsal LPFC) aspects of WM (Fuster, 1973; 1988; Funahashi et al., 1989; Goldman-Rakic, 1995). Active maintenance of WM representations is achieved in part through sustained activity (i.e., activity after stimulus offset) in LPFC neurons enabled by slow recurrent excitation among cells of encoding populations (Wang, 1999; Wang et al., 2013). LPFC is thought to maintain information about goals and procedures to achieve those goals while exerting cognitive control by biasing the flow of information between sensory, executive, and motor areas (Miller and Cohen, 2001). Populations encoding rules have been found in DLPFC (Buschman et al., 2012) and are further hypothesized to guide the selection of the appropriate goal-achieving procedure based on present context and stimuli.

The anterior cingulate cortex (ACC) is a structural and functional hub (Park and Friston, 2013) that has been hypothesized to monitor diverse signals (e.g., errors, conflicts, rewards, uncertainty) in order to perform a cost/benefit analysis regulating resource allocation for cognitive control (Shenhav et al., 2013; 2016). It has been shown to rhythmically synchronize with DLPFC during shifts in task demands (Womelsdorf et al., 2014; Vohol et al., 2015) and is thought to be involved in updating behavior-guiding rules. In this work, I will focus on neural mechanisms that serve the operations of rule-based selection in LPFC and input combination for process monitoring in ACC.

1.1.2   Cognitive rhythms

Oscillatory dynamics in prefrontal cortex are ubiquitous, diverse, task-modulated, and correlated with performance; nevertheless, the ways in which such brain dynamics support cognition is only beginning to be addressed. It has been well-established that oscillations are involved in rule-based selection in LPFC and process monitoring in ACC. In LPFC, beta (12-30Hz) and gamma (30-100Hz) frequency rhythms have been observed in delayed-response tasks and tasks with rule-based action (Cho et al., 2006; Tzur and Berger, 2009; Buschman et al., 2012; Siegel et al., 2009). For instance, populations encoding items in DLPFC during a delay are temporally segregated by spiking at different phases of an underlying 32Hz oscillation (Siegel et al., 2009); and populations encoding rules synchronize with a similar high beta-frequency oscillation in DLPFC. Oscillations with widely varying frequencies have been observed in regions monitored by ACC; for instance, 25-35Hz in DLPFC (Buschman et al., 2012), 35-45Hz in amygdala (Popescu et al., 2009), 60Hz in orbitofrontal cortex (OFC) (Pennartz et al., 2011), and 30-100Hz nested in 6-9Hz in hippocampus (Buzsaki, 2002; Csicsvari et al., 2003).

The cellular and network generators of distinct network rhythms have been studied using *in vitro* techniques that isolate microcircuits and drive them using pharmacological agents (Whittington, 1995; Randall et al., 2011). These studies have shown that all regions of PFC are capable of generating fast network oscillations and that different layers within particular regions have intrinsic mechanisms capable of generating different beta and gamma-frequency network oscillations (see Fig. 1.1 and Table 1). This implies that PFC has evolved to produce a diversity of rhythms and that cognitive tasks

selectively engage those rhythmic mechanisms in task-relevant ways. Experimental and theoretical work has revealed functional roles that fast network oscillations can play in mediating communication and the routing of information (described below) (Cannon et al., 2014).

Different regions

Anterior cingulate

Prelimbic cortex

Different layers of ACC
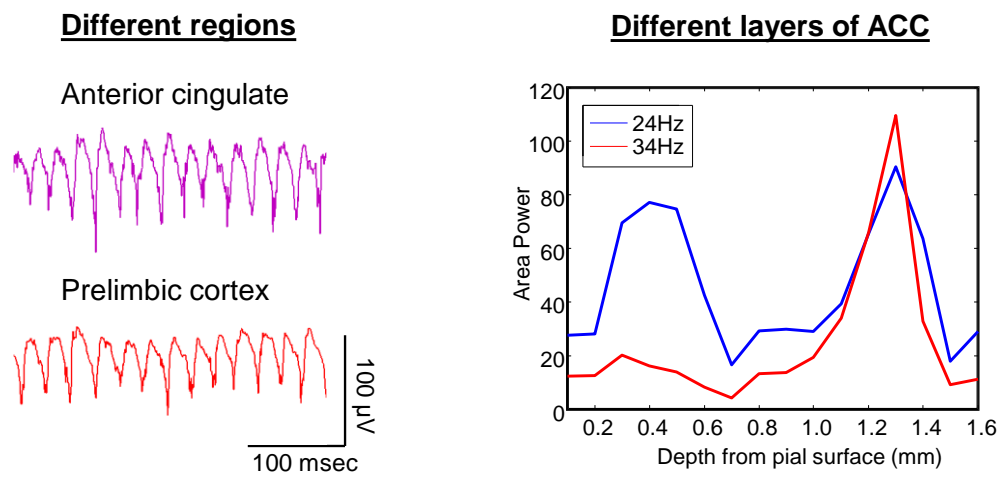
Fig. 1.1. Region- and layer-specific *in vitro* oscillations in rat mPFC. [1]

drug	Anterior Cingulate		Prelimbic Cortex	
	Superficial	Deep	Superficial	Deep
Carbachol:		γ [1]	β_2 , γ [2]	β_2 [2]
Kainate:	β_2 [1]	β_2 , γ [1]		β_2 , γ [1]

Table 1. Summary of region- and layer-specific *in vitro* oscillations in rat mPFC.

---

[1] Unpublished data from LeBeau laboratory at Newcastle University.
[2] Data from Van Aerde et al., 2009.

1.1.3 Computational modeling traditions

Computational modeling coupled with experimentation has advanced understanding beyond what either approach could achieve alone. Two traditions of modeling dynamical systems in computational neuroscience have evolved since the mid-20th century, one inspired by cognitive science and the other by neurophysiology. Both attempted to elucidate neural mechanisms that can account for observed phenomena, but their phenomena of interest differed and, consequently, so did the neural mechanisms they considered important for their purposes. One focused on representation, learning, and information processing while the other focused on intrinsic cell properties, neurotransmission, and neural rhythms. The cognitive tradition began by abstracting neural elements as much as possible in an effort to understand mind while the neurophysiological tradition focused on whatever biological details were relevant at the spatial and temporal scale of their phenomena of interest.

In recent decades, the two traditions have converged increasingly as the more abstract models of mental processes incorporated greater physiological detail and the physiological models increased in spatial scale. One important point of convergence has occurred by virtue of a shared interest in microcircuit operations that govern the flow of information through specific structures in the brain. This dissertation is a result of that convergence in the context of prefrontal cortex and the dynamics it manifests during rule-based cognitive control. Next, we will briefly review models from each tradition, including both foundational models to highlight their original differences as well as the more recent models on which my subsequent work builds.

1.2   Computational models for cognitive control

The first dynamical system models we will review are descendants of a tradition inspired by cognitive science. The tradition began with the advent of connectionism when it was discovered that abstract neural units based on threshold logic coupled into networks with adjustable connection weights could learn arbitrary mappings between input and output representations (McCulloch and Pitts, 1943; Rosenblatt, 1958). These artificial neural networks were viewed as performing computations by virtue of the learned input-output mapping stored in their connection weights; however, such models lack dynamics and biophysical realism.

1.2.1   Attractor networks for working memory and rules

Research into models supporting associative content-addressable memory led to the development of networks with dynamics that represent memories as activity patterns that are stable fixed point attractors of the dynamical system (Amari, 1977; Hopfield, 1982). Memory storage was still based on synaptic weights tuned by learning procedures except now all inputs that move the system to the same basin of attraction result in reactivation of the same memory (i.e., the inputs are associated). While early attractor networks used rate neurons, the development of appropriate mean-field theories (Fusi, 1999) enabled the construction of attractor networks with spiking neurons. One model with special relevance to our work is a WM attractor network with principal cells and fast spiking interneurons constrained by physiological data from the deep layers of rat medial PFC (prelimbic cortex) (Durstewitz et al., 2000). This PFC model of working memory represents one point of convergence between the two traditions of dynamical system

modeling in computational neuroscience and will serve as the basis for some of our work described below.

A more recent model with a hidden layer of mixed selectivity PFC neurons has been used to study rule-based transitions among stable attractors (persistent activity) representing cognitive states (Rigotti et al., 2010), but it only considered ungated actions (cognitive state transitions). While ungated cognitive actions are probably important for the steady flow of natural thought, gating is likely important for the reasons considered next.

1.2.2 *Gated working memory models*

Maintenance versus updating of WM requires a tradeoff between stability and flexibility of representation (Frank and Badre, 2015). One solution involves using the basal ganglia (BG) to gate inputs to WM by mediating disinhibition of thalamic populations delivering inputs to PFC (Frank et al., 2001); when the gate is closed, representations are stable; when the gate is open, representations can be updated. Functionality of the PFC/BG WM system was hard-wired into the network structure of early models with dynamic BG-mediated input gating. More recently, reinforcement learning based on the midbrain dopaminergic system has been incorporated into subsequent versions of the model (O'Reilly and Frank, 2006). These learning mechanisms replaced the need for hard-wiring by the modeler with automated learning of what representations are task relevant and how to gate WM in service of task-specific goals.

In contrast, output gating is necessary for responding with the appropriate action at the appropriate time (Chatham et al., 2014). BG inhibitory gating has been proposed for gating motor outputs (i.e., action plans) among parallel pathways based on competitive dynamics among sources controlling the BG gate through convergent projections to striatum (Brown et al., 2004). Recent experimental work has provided evidence that a similar BG-mediated gating mechanism can gate outputs from WM through PFC/BG interactions (Chatham et al., 2014; Chatham and Badre, 2015).

While these gated WM models incorporate aspects of anatomy and physiology, and have been successful at clarifying some of the challenges inherent in cognitive control, they are rate models and thus unable to account for effects that depend on precise spike timing (e.g., sensitivity to spike coherence); also, they lack oscillatory dynamics and thus cannot account for effects of resonance (e.g., sensitivity to oscillation frequency). I will show in Chapter 2 that these effects can have important consequences for WM output gating and rule-based action.

1.3   Computational models for rhythms and routing

The second group of models we will review descends from a tradition inspired by neurophysiology. This tradition began with the formulation of a nonlinear system based on the dynamics of RC circuits that predicted voltage-dependent changes in transmembrane ionic conductance underlie electrical neurotransmission (Hodgkin and Huxley, 1952). That prediction and others (e.g., transmission speed) were later validated by experiments. Biophysically-detailed models to date employ the same conductance-based framework developed by Hodgkin and Huxley (Traub et al., 2005; Markram et al.,

2015). The physiologically-inspired tradition was further bolstered in the beginning by the discovery of a statistical model predicting that quantal release underlies chemical neurotransmission across synapses (Del Castillo and Katz, 1954); however, modern models often use deterministic mechanisms to approximate the postsynaptic effects of presynaptic events.

1.3.1   *Inhibition-paced network oscillations*

Studying abstract, mass action models, Freeman (1975; 1979) proposed that local feedback inhibition between interacting populations underlies gamma-frequency EEG oscillations observed in olfactory cortex. Support for the model came later from *in vivo* experiments confirming predictions about the activity of populations involved in the oscillation (Eekman and Freeman, 1990). However, these studies did not prove that inhibitory synapses were necessary or that the duration of inhibition played a significant role. The physiology of inhibition-paced network oscillations was conclusively demonstrated first in the context of gamma-frequency oscillations in hippocampus (Whittington, 1995; 1997). It was found that hippocampal networks of mutually inhibitory fast spiking interneurons generated gamma oscillations under tonic drive while excitatory synapses were pharmacologically blocked (Whittington, 1995). This form of interneuron network gamma (ING) was subsequently simulated in a biophysically-detailed hippocampal model (Wang and Buzsaki, 1996). Next, a second form of stimulus-driven network gamma oscillation was identified that depended on pyramidal cells driving fast spiking interneurons through AMPA synapses and interneurons providing feedback inhibition onto the pyramidal cells through GABA$_A$ synapses. The oscillation

frequency of both ING and pyramidal-interneuron network gamma (PING) oscillations depended most strongly on the duration of $GABA_A$-mediated inhibition (i.e., the oscillations were paced by inhibition).

PING oscillations can exist in two forms: one where pyramidal cells spike on every cycle (strong PING) and one where pyramidal cells spike irregularly at low rates (weak PING). A considerable amount of theoretical work has investigated the properties of these gamma rhythms (Borgers et al., 2005; Borgers, 2008; Kopell, 2010). That work demonstrated that gamma rhythms are useful for binding activity into coherent assemblies, mediating inter-regional communication through coherence, and filtering signals using frequency and/or coherence selectivity (Cannon et al., 2014). In Chapter 2, I will demonstrate the importance of weak PING for routing rate-coded signals. In Chapter 3, I will show through experiments and models that the same inhibitory-pacing mechanism underlies the generation of both beta- and gamma-frequency network oscillations in ACC, mediated by different populations of interneurons, and consider consequences relevant to the role of ACC in monitoring processes for the regulation of cognitive control.

1.3.2 *Oscillation-based output gating*

A spiking model with an ING sub-network providing feedforward inhibition to principal cells creates a bandpass filter where principal cells respond selectively to gamma-frequency inputs (Akam and Kullmann, 2010). For asynchronous and oscillatory inputs at lower or higher frequencies, the ING sub-network spikes before the principal cells and prevents them from responding to simultaneous input. However, for inputs at

gamma frequencies, inhibitory cells spike at a later phase of the oscillatory input, enabling the principal cells to spike on each cycle of the input. Filter networks of this sort are able to selectively read-out gamma-frequency signals mixed among distractors in an upstream source network. This enables frequency-dependent output gating (de-multiplexing) of rate-coded signals from oscillatory networks. In Chapter 2, I will demonstrate an alternative resonance mechanism by which weak PING networks enable more flexible frequency-dependent output gating of rate-coded signals.

1.4   Approach and overview of dissertation

So far, we have discussed that cognitive control involves WM in LPFC using rules to bias the selection of input-output mappings governing behavior and ACC monitoring processes to update behavior-guiding rules. We also reviewed computational models demonstrating how rate-based mechanisms can gate (i.e., select) inputs and outputs from WM and how oscillations can be selectively read-out through filter networks. In this dissertation, I will advance ideas on how rate- and oscillation-based gating can coexist in service of selecting rule-based input-output mappings and how heterogeneity in ACC enables the combination of inputs that would otherwise be subject to selective input gating by the same mechanisms. More specifically, I will investigate the effects of inhibition-paced network oscillations in LPFC on output gating for rule-based action and the effects of heterogeneity of intrinsic cell properties in ACC on the ability of ACC to monitor concurrent processes. This work will demonstrate how neurophysiological data can advance our mechanistic understanding of the contributions of oscillatory dynamics and heterogeneity to cognitive control processes.

In Chapter 2, we will address the question of how neural oscillations support output gating and rule-based selection. To do this, I will use computational modeling to explore how a purely feedforward output layer exhibiting physiologically-motivated weak PING dynamics can provide frequency- and coherence-based output gating of rate-coded WM representations in LPFC. I will also demonstrate how differential drives to distinct interneuron populations can switch WM representations of the attractor network between asynchronous and oscillatory states that support rule-based selection of input-output mappings.

In Chapter 3, we will address the question of how the selective mechanisms described in Chapter 2 can be overcome for combining inputs in ACC. To do this, I will use a combination of *in vitro* and computational modeling. First, *in vitro* techniques will be used to characterize the high degree of heterogeneity of intrinsic cell properties in rat ACC. I will then use modeling to explore the effects of observed heterogeneity on the ability of ACC microcircuits to integrate information from source networks in different dynamical states. Mechanistic models of ACC monitoring operations are less developed in the literature than the models of LPFC cognitive control operations reviewed earlier. Chapter 3 presents a first step toward applying neurophysiological constraints to a mechanistic investigation of ACC dynamics serving cognition. We recorded from single cells and network oscillations in rat dorsal ACC, quantified the extensive heterogeneity in intrinsic cell properties, and used computational modeling to explore the implications of heterogeneity on the ability of ACC to combine inputs from diverse sources in service of process monitoring.

1.4.1   Conceptual model of cognitive control-related ACC/LPFC rhythms

The work presented throughout this dissertation is organized around the conceptual model shown in Fig. 1.2. The model is based on the anatomy and physiology of ACC and LPFC and their distinct contributions to cognitive control. It will be introduced briefly here and described in more detail as needed in later chapters. The conceptual model consists of laminar networks in ACC and LPFC with cell types and connections based on primate anatomy. The ACC receives inputs from limbic structures and association cortex, with different natural frequencies, providing information to guide the regulation of cognitive control signals. The LPFC receives feedforward inputs from sensory cortices and modulatory feedback projections from ACC. Rule-related populations exhibit beta-frequency oscillations that enable the selection of context-dependent input-output mappings. Functionally, ACC must combine inputs for monitoring diverse networks and triggering rule updating while LPFC mediates output selection for beta-rhythmic rule application. All task-relevant signals are assumed to be rate-coded and embedded in network oscillations. Importantly, while the conceptual model and example below make assumptions about the functions of specific regions, my results do not depend on those assumptions and will remain significant even if they are proven false.

As an example, consider a person at a gym with the option to either bike or lift weights. If the person "feels like" lifting weights, a 60Hz oscillatory population in OFC may deliver to ACC a stronger value signal for the option to lift weights than a second 60Hz population encoding the value for the option to bike (Pennartz et al., 2011; Holroyd

and Yeung, 2011). A straightforward rate-based comparison in ACC could then trigger the selection of weight lifting rules in DLPFC; a potential mechanism for rule selection will be presented in section 2.5. Rule-related input-output mappings in DLPFC then guide the execution of the weight lifting motor program. My model proposes that rules amplify the appropriate mappings by engaging their input populations in oscillations that are resonant in the output layer. Such oscillation-based gating enables the flexible selection of outputs (e.g., the action plan for lifting weights) without requiring changes in the activity levels of inputs (e.g., visual image or WM representation of the weights).

If the person has sore muscles from a previous workout, a 40Hz amygdala population may deliver to ACC an emotional conflict signal associated with the affective dimension of pain (Neugebauer, 2015). The combination of information from 60Hz OFC and 40Hz amygdala populations in ACC should result in a combinatorial re-evaluation (i.e., cost/benefit analysis) of the available options (Shenhav et al., 2016). However, the difference in OFC and amygdala rhythm frequencies would preclude concurrent processing of the parallel information streams if oscillation-based gating was present in the ACC input layer. My model proposes that PC heterogeneity increases network bandwidth, enabling ACC to respond simultaneously to signals at different frequencies. Thus, heterogeneity could enable a new cost/benefit analysis in ACC to result in the selection of the option to bike and, subsequently, the adjustment of cognitive control by triggering DLPFC to engage the set of rules appropriate for biking.
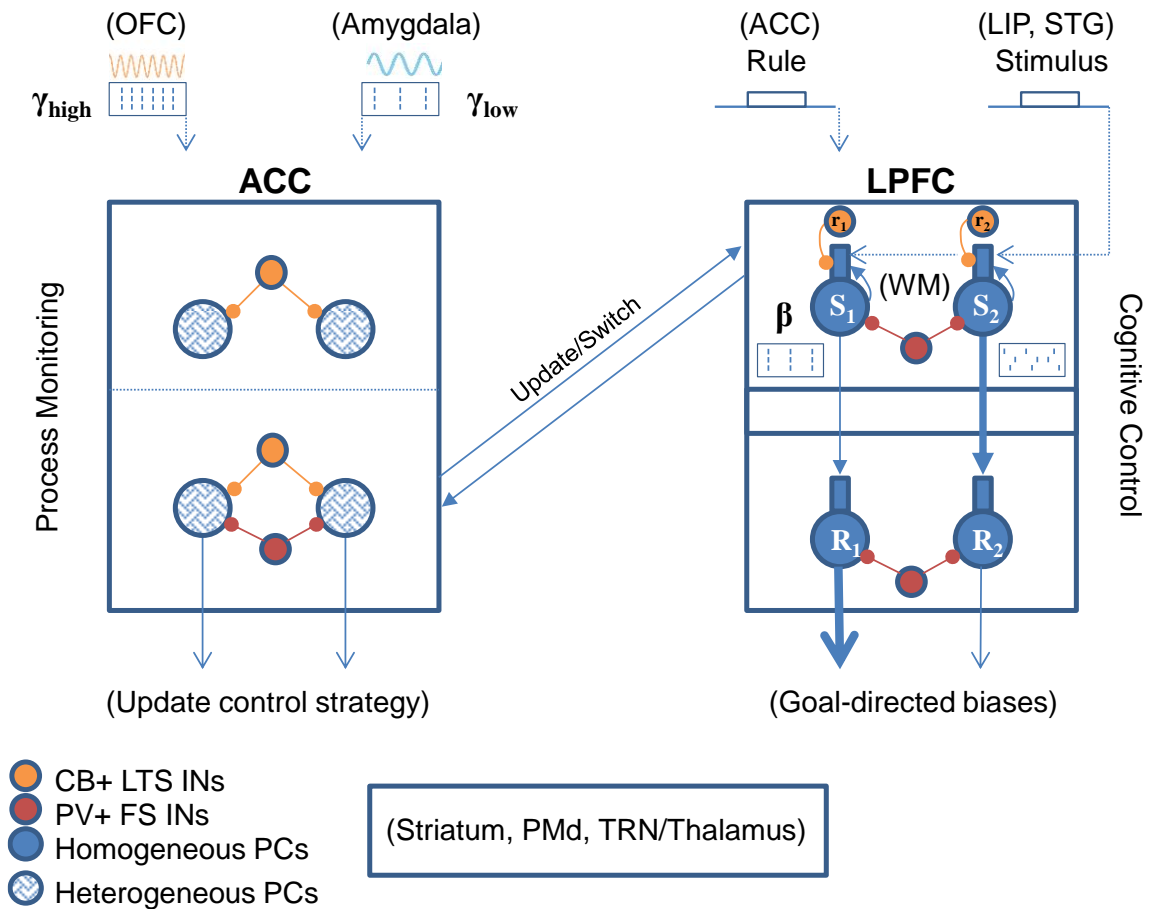
Fig. 1.2. Conceptual model of cognitive control-related ACC/LPFC rhythms.
ACC (left) receives monitoring signals from diverse regions (e.g., OFC, amygdala) with different natural frequencies (e.g., γ_{low}=40Hz, γ_{high}=80Hz). Heterogeneous PC populations enable ACC to respond to concurrent inputs at different frequencies and perform combinatorial evaluation for regulating cognitive control. LPFC (right) receives sensory signals (stimuli; e.g., from LIP and STG) and maintains them in working memory (WM) in superficial layers and delivers goal-directed biases from deep layer PCs to subcortical structures that govern action (e.g., striatum, PMd, TRN/thalamus). Parallel interlaminar pathways represent learned input-output mappings (e.g., $S_1 \rightarrow R_1$, $S_2 \rightarrow R_2$). Superficial LTS cells are rule-selective (e.g., r_1, r_2) and induce β (e.g., 25Hz) rhythmicity in all PCs inhibited by them. In conjunction with deep layer β resonance, this setup enables rule signals driving select LTS cells to amplify all input-output mappings with inputs coupled to the driven LTS cells; the figure shows only one mapping per rule for simplicity. Resonance enables weaker rule-related inputs (thin arrow from $S_1 \rightarrow R_1$) to produce greater output (thick arrow from R_1). Regulatory signals from ACC update rules in LPFC by adjusting drives to LTS cells. PC, principal cell; IN, interneuron; FS, fast spiking; LTS, low threshold spiking.

1.4.2   The DynaSim toolbox

DynaSim is a Matlab/Octave toolbox I developed for rapid prototyping of large neural models, batch simulation management, and efficient model sharing. It was designed to speed up and simplify the process of generating, sharing, and exploring network models similar to those described above. Models can be specified by listing equations or by specifying model composition using lists of predefined, mechanistically-meaningful model objects. Its higher-level specification easily scales to arbitrarily complex population models and networks of interconnected populations.

DynaSim also includes a unique set of features that simplify the processes of exploring model dynamics over parameter spaces, running simulations in parallel on a compute cluster, as well as parallel analysis and plotting of large numbers of simulated data sets. It includes a graphical user interface that supports full functionality without requiring user programming. The design of DynaSim incorporates a simulator-independent model specification to facilitate interoperability with other specifications (e.g., NeuroML, SBML), simulators (e.g., NEURON, Brian), and web-based applications (e.g., Geppetto) outside Matlab. The hope is that this tool will reduce barriers to exploring dynamics in complicated neural models, facilitate collaborative modeling, and complement other tools being developed in the neuroinformatics community. All models in this dissertation were implemented in DynaSim. The details of the DynaSim software will be presented in Appendix A.

1.5   Final remarks

The work to follow builds on the concepts presented in this chapter. We are going to focus on biophysical and network properties that are not accounted for by most models of cognitive control. Specifically, we will focus on the effects of population oscillations and neuronal heterogeneity on microcircuit operations required for cognitive control. I will show that PFC population oscillations support on-demand frequency-based output selection for rule-based action (Chapter 2) and that ACC heterogeneity reduces selectivity and supports combining inputs from multiple sources (Chapter 3), enabling combinatorial information monitoring in service of regulating cognitive control.

CHAPTER 2

PREFRONTAL RHYTHMS BIAS PATHWAYS FOR THOUGHT AND ACTION

2.1 Introduction

Adaptive behavior requires the ability to flexibly shift attention and behavioral strategies in response to a changing environment. For instance, when the phone rings while you are reading a paper you must quickly shift attention to the source of sound, engage the proper motor plan, and prepare the appropriate social program. Shifting attention among stimuli and engaging appropriate context-dependent actions involves re-routing signals through select paths in cortex serving process-specific functions. Signals could be routed using dedicated circuits shaped by past experience, but flexible signal routing for adaptive cognition requires dynamic mechanisms that can route signals in different ways using the same underlying neural circuitry.

Changes in oscillatory synchronization across rate-coding populations of neurons in prefrontal cortex (PFC) have been implicated in a variety of cognitive tasks that require flexible signal routing. For instance, in a task that required a Macaque monkey to saccade either left or right given the same visual stimulus depending on the active behavior-guiding rule, populations of cells in PFC exhibited task-modulated oscillations (20-35Hz) with greater synchrony (coherence) across populations whose firing rates

encoded the active rule (Buschman et al., 2012). Similarly, in premotor cortex of humans and nonhuman primates, behavior-guiding choice representations exhibited task-modulated beta oscillations (20-30Hz) in a vibrotactile comparison task (Herding et al., 2016); and in rodent PFC, behavior-guiding choices were correlated with beta-frequency oscillations (13-30Hz) in a T maze working memory task (Parnaudeau et al., 2013). In all of these cases, synchronous beta-frequency oscillations were present during response preparation in select populations of neurons encoding signals presumably routed downstream to guide action selection mechanisms; populations coding alternative rules or choices exhibited weaker or no beta synchrony.

Routing signals involves selectively propagating activity to downstream populations and depends on both cell firing rates and the dynamical state of input populations. Networks of interacting excitatory (E) and inhibitory (I) cells can exhibit larger firing rate responses to oscillatory inputs with frequencies in a particular range, a phenomenon called firing rate resonance (Richardson et al., 2003). Modeling work has demonstrated that, with sufficient feedforward inhibition, this form of resonance produces a band-pass filter network that can perform selective frequency-based readout of a gamma-rhythmic (40Hz) signal mixed among asynchronous distractors in an input population (Akam and Kullmann, 2010). Similarly, feedback inhibition can suppress responses to less resonant and less coherent inputs delivered to the same output population (Cannon et al., 2014). However, it is not known how input oscillatory states affect output selection in a layer with competing output populations.

Rate-based models of competing populations without input firing-rate oscillations can exhibit winner-take-all dynamics whereby the output population receiving the strongest input tends to silence the more weakly-driven populations (Kaski and Kohonen, 1994). Similar competitive dynamics have been demonstrated in spiking models between gamma-rhythmic populations (Borgers et al., 2005) and cells of a shared gamma-rhythmic network (de Almeida et al., 2009). Specifically, when the competing populations exhibited inhibition-paced gamma oscillations, the larger input resulted in the selective activation of its target population and suppression of competing distractors (Borgers et al., 2005). When different cells of the same gamma-rhythmic population received inputs with different strengths, only those within some percentage of the most strongly driven cell fired (de Almeida et al., 2009). These studies examined the impact of variable-strength inputs approximating asynchronous signals on competition between populations exhibiting oscillatory dynamics at a particular frequency; consequently, they represent mechanisms for input firing rate-based selection of oscillatory outputs and require input firing rate changes to perform signal routing. It remains unknown how competition is affected by oscillatory inputs and how output selection can be performed without requiring input firing rate changes.

In this work we used computational modeling to explore input frequency- and coherence-based output selection mechanisms for flexible routing that conserve rate-coded signals. We show that the oscillatory states of input encoding populations can exhibit a stronger influence over downstream competition than their activity levels (firing rates). This enables an output driven by a weaker frequency-resonant input signal (i.e., a

signal maximizing output population frequency) to suppress lower-frequency competing responses to stronger, less resonant (though possibly higher-frequency) input signals. While signals are encoded in population firing rates, output selection and signal routing can be governed independently by the frequency and coherence of oscillatory inputs and their correspondence with output resonant properties. Flexible response selection and gating can be achieved by control mechanisms that change the oscillatory state of select input encoding populations. The oscillatory state that is preferentially output can be flexibly tuned by nonspecific synaptic inputs and neuromodulation that change resonant properties in the output layer. These dynamic mechanisms could enable the experimentally-observed PFC beta and gamma oscillations to flexibly govern the selection and gating of rate-coded signals for downstream read-out.

This chapter begins with an overview of the modeling methods used and a technical account of how two E/I networks (a classic Hodgkin-Huxley model and a detailed PFC model) respond to population inputs with different dynamical states. Next, we investigate the conditions enabling input oscillatory states to govern selection among competing outputs. Finally, the chapter will close with a discussion of how frequency- and coherence-based output selection can serve flexible output gating from a working memory buffer (with discrete slot-like item encoding or high-dimensional reservoirs of cells with mixed selectivity) and rule-based action selection (stimulus-response mapping) with context-dependent oscillatory states.

2.2 Methods

2.2.1 Network models

The network model represents a cortical output layer with 20 excitatory principal cells (PCs) connected reciprocally to 5 inhibitory interneurons (INs). PC and IN models were taken from a computational representation of a deep layer PFC network consisting of two-compartment PCs (soma and dendrite) with ion channels producing I_{NaF}, I_{KDR}, I_{NaP}, I_{Ks}, I_{Ca}, and I_{KCa} currents (μA/cm^2) and fast spiking INs with channels producing I_{NaF} and I_{KDR} currents (Durstewitz and Seamans, 2002) (Fig. 2.1A; see figure caption for channel definitions). IN cells had spike-generating I_{NaF} and I_{KDR} currents with more hyperpolarized kinetics and faster sodium inactivation than PC cells, resulting in a more excitable interneuron with fast spiking behavior (Durstewitz and Seamans, 2002). In the control case, PC and IN cell models were identical to those in the original published work (Durstewitz and Seamans, 2002). Knockout experiments were simulated by removing intrinsic currents one at a time from the PC cell model.

All cells were modeled using a conductance-based framework with passive and active electrical properties of the soma and dendrite constrained by experimental considerations (Durstewitz et al., 2000). Membrane potential V (mV) was governed by:

$$C_m \frac{dV}{dt} = -I_{inp}(t, V) - \sum I_{int} - \sum I_{syn}$$

where t is time (ms), $C_m = 1$ μF/cm^2 is the membrane capacitance, I_{int} denotes the intrinsic membrane currents (μA/cm^2) listed above, $I_{inp}(t, V)$ is an excitatory current (μA/cm^2) reflecting inputs from external sources described below, and I_{syn} denotes

synaptic currents (μA/cm^2) driven by PC and IN cells in the network. We also explored a simpler classic E/I network model for comparison consisting of one-compartment Hodgkin-Huxley neurons with spike-generating I_{Na} and I_K currents (Hodgkin and Huxley, 1952) grouped into excitatory (E) and inhibitory (I) populations (Fig. 2.1B). See Appendix B for the complete list of model equations.

The output layer had either one or two populations of PC cells with each output population receiving either one or two input signals. Input frequency-dependent response profiles were characterized using a network with one input and one output (Fig. 2.1A-B). Competition between the outputs of parallel pathways was investigated using a network
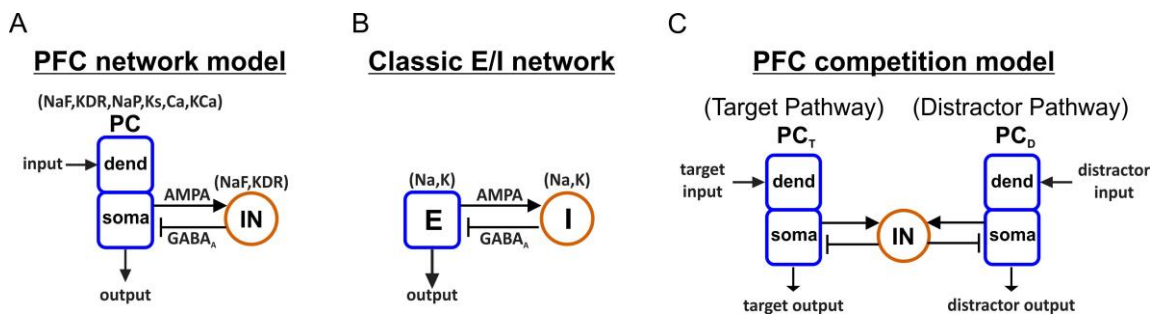
Fig. 2.1. Architecture of output networks.
(**A**) Diagram showing feedforward excitation from external independent Poisson spike trains to the dendrites of 20 two-compartment (soma, dend) principal cells (PCs) receiving feedback inhibition from a population of 5 fast spiking interneurons (INs). All PC and IN cells have biophysics based on rat prelimbic cortex (Ion channel key: NaF = fast sodium channel; KDR = fast delayed rectifier potassium channel; NaP = persistent sodium channel; Ks = slow (M-type) potassium channel; Ca = high-threshold calcium channel; KCa = calcium-dependent potassium channel). (**B**) Diagram showing input to 20 excitatory (E) Hodgkin-Huxley (HH) neurons receiving feedback inhibition from 5 inhibitory (I) HH neurons. All HH neurons have identical biophysics based on the squid giant axon (Ion channel key: Na = sodium channel; K = potassium channel). (**C**) Diagram showing a rhythmically-driven target population of PC cells (PC$_T$) competing with an asynchronously-driven distractor population (PC$_D$) through a shared population of inhibitory IN cells.

with two homogeneous output populations receiving one input each while interacting through a shared population of inhibitory cells (Fig. 2.1C). Output gating of signals from convergent pathways was investigated using two input signals that converged on a single output population.

2.2.2 Network connectivity

PC cells provided excitation to all IN cells, mediated by α-amino-3-hydroxy-5-methyl-4-isoxazolepropionic acid (AMPA) currents. IN cells in turn provided feedback inhibition mediated by γ-aminobutyric acid (GABA$_A$) currents to all PC cells. AMPA currents were modelled by:

$$I_{AMPA} = g_{AMPA}s(V - E_{AMPA})$$

where V is the postsynaptic membrane voltage, g_{AMPA} is the maximal synaptic conductance, s is a synaptic gating variable, and $E_{AMPA}= 0$ mV is the synaptic reversal potential. Synaptic gating was modeled using a first-order kinetics scheme:

$$\frac{ds}{dt} = H(V_{pre})\frac{(1 - s)}{\tau_r} - \frac{s}{\tau_d}$$

where V_{pre} is the presynaptic membrane voltage, $\tau_r = .4$ ms and $\tau_d = 2$ ms are time constants for neurotransmitter release and decay, respectively, and $H(V) = 1 + \tanh(V/10)$ is a sigmoidal approximation to the Heaviside step function. GABA$_A$ currents are modeled in the same way with $E_{GABA} = $ -75mV and $\tau_d = 5$ ms unless otherwise specified. Maximum synaptic conductances for PC-cells were (in mS/cm^2): GABA$_A$ (.1); for IN-cells: AMPA (1).

Effects of recurrent excitation within each output population were investigated in select simulations. In those cases, PC-to-PC excitation was mediated by AMPA and N-methyl-D-aspartate (NMDA) currents:

$$I_{NMDA} = g_{NMDA}M(V)s(V - E_{NMDA})$$

where $M(V) = \frac{1.50265}{1+.33e^{-V/16}}$ is a sigmoidal magnesium block (Durstewitz and Seamans, 2000) and synaptic gating was governed by first-order kinetics with $H(V) = \frac{1}{1+e^{-(V-2)/5}}$, $\tau_r = 10.6$ ms, $\tau_d = 285$ ms, and $E_{NMDA} = 0$ mV. Maximum excitatory synaptic conductances for PC cells were (in mS/cm^2): AMPA (.9), NMDA (.9).

2.2.3 External inputs

Each PC cell received independent Poisson spike trains (Fig. 2.2) with time-varying instantaneous rate $\lambda(t)$ and time-averaged rate $\bar{r}_{inp} = \langle\lambda\rangle$; spikes were integrated in a synaptic gate s_{inp} with exponential AMPAergic decay contributing to an excitatory synaptic current $I_{inp} = g_{inp}s_{inp}(V - E_{AMPA})$ with maximal conductance g_{inp} (mS/cm^2). Input signals were modeled by collections of spike trains with the same instantaneous rate-modulation while collectively encoding representations in their time-averaged rates on a slower time scale. A given input signal to a PC output population can be interpreted as conveying rate-coded information from a source population in a particular dynamical state.

A Asynchronous Input

i Constant spike rate

$\lambda(t) = r_{inp}$

ii Input population spikes

B Oscillatory Inputs

i Square wave: Low sync.

$1/f_{inp}$ δ_{inp}

ii

iii Square wave: High sync.

iv Sine wave

$1/f_{inp}$
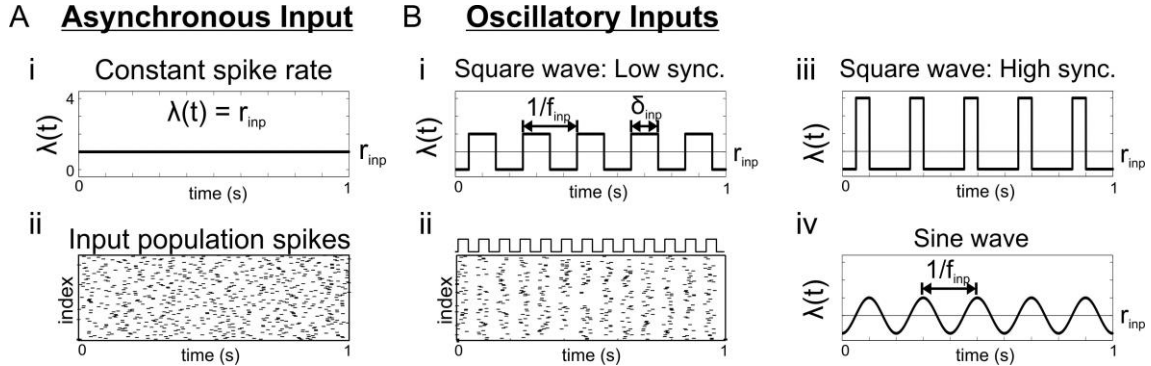
Fig. 2.2. Input network activity.
(**A**) Asynchronous Poisson input with (i) constant instantaneous rate r_{inp} and (ii) raster for 100 input cells with r_{inp} = 10 sp/s (equivalent to 1 input cell with r_{inp} = 1000 sp/s). (**B**) Poisson inputs with oscillatory instantaneous rate-modulation. (i) Instantaneous rate modulated by low synchrony square wave, parameterized by pulse width δ_{inp} and inter-pulse frequency f_{inp}. (ii) raster plot produced by square wave input. (iii) High synchrony, square wave rate-modulation. (iv) sine wave modulation, parameterized by frequency f_{inp}.

Population rate-coding was incorporated into an input signal using a spatial pattern of time-averaged firing rates $\bar{r}_{inp}(x)$ for spike trains driving an output with cells indexed by x. Spatial profiles were either uniform or Gaussian bumps centered on different output neurons. Signals from sources in different dynamical states were generated by modulating instantaneous rates $\lambda(t)$ according to the activity patterns exhibited by populations in those states. Signals from source populations in an asynchronous state were modeled by Poisson spike trains with constant rate $\lambda(t) = \bar{r}_{inp}$ (Fig. 2.2A) whereas signals from sources in an oscillatory state were modeled using periodically-modulated instantaneous rates (Fig. 2.2B). Signals with sine wave modulation had $\lambda(t) = \bar{r}_{inp}(1 + \sin(2\pi f_{inp}t))/2$ parameterized by $\bar{r}_{inp}$ and rate-modulation frequency f_{inp}. Sinusoidal modulation causes spike synchrony (the interval

over which spikes are spread within each cycle) to covary with frequency as the same number of spikes become spread over a larger period as frequency decreases. Thus, we also investigated oscillatory inputs with square wave modulation in order to differentiate the effects of synchrony and frequency while maintaining the ability to compare our results with other work. Square wave rate-modulation results in periodic trains of spikes with fixed synchrony (pulse packets) parameterized by $\bar{r}_{inp}$, inter-pulse frequency f_{inp}, and pulse width δ_{inp}. δ_{inp} reflects the synchrony of spikes in the source population with smaller values implying greater synchrony.

All cells in the output layer received additional asynchronous inputs representing uncorrelated background activity from 100 cells in other brain areas spiking at 1 sp/s. Notably feedforward inhibition was excluded from the present work so that asynchronous inputs were maximally effective at driving PC cells. The effects of adding feedforward inhibition and conditions under which each case holds are considered in the Discussion. Control values for input parameters were $\bar{r}_{inp} = 1000$ sp/s (corresponding to a source population with 1000 projection neurons spiking at 1 sp/s); $\delta_{inp}=1$ms (high synchrony), 10ms (medium synchrony), or 19ms (low synchrony), and $g_{inp} = .0015$mS/cm^2.

In simulations probing resonant properties, the input modulation frequency f_{inp} was varied from 1Hz to 50Hz (in 1Hz steps) across simulations. In simulations exploring output gating among parallel and convergent pathways, input signals had the same mean strength (i.e., $\bar{r}_{inp}$) unless otherwise specified; this ensures that any difference between the ability of inputs to drive their targets resulted from differences in the dynamical states of the source populations and not differences in their activity levels.

Symbol	Description
$\lambda(t)$	Instantaneous input rate of Poisson process (kHz)
$\bar{r}_{inp}$	Time-averaged Poisson input rate, $\langle\lambda\rangle_t$ (kHz)
f_{inp}	Frequency of Poisson input rate-modulation (Hz)
δ_{inp}	Pulse width of Poisson input with square wave rate-modulation (ms)
iFR	Instantaneous output firing rate averaged over principal cells (sp/s)
$\bar{r}_{PC}$	Time-averaged population firing of principal cells (sp/s)
$\bar{r}_{IN}$	Time-averaged population firing of interneurons (sp/s)
f_{pop}	Frequency of output population activity (Hz); identical for PCs and INs
f_N	Natural frequency (Hz) (i.e., f_{pop} elicited by asynchronous input)
f_R^{PC}	$\bar{r}_{PC}$-resonant frequency (Hz) (i.e., input f_{inp} maximizing output $\bar{r}_{PC}$)
f_R^{IN}	$\bar{r}_{IN}$-resonant frequency (Hz) (i.e., input f_{inp} maximizing output $\bar{r}_{IN}$)
f_R^{pop}	f_{pop}-resonant frequency (Hz) (i.e., input f_{inp} maximizing output f_{pop})
x^T	Property x in Target pathway
x^D	Property x in Distractor pathway
r_{rhythm}	$\bar{r}_{inp}^T$ for oscillatory input to Target pathway
r_{async}	$\bar{r}_{inp}^D$ for asynchronous input to Distractor pathway
$\Delta\bar{r}$	Difference (Target-Distractor) in mean output firing rates, $\bar{r}_{PC}^T - \bar{r}_{PC}^D$.
$\bar{r}_{inp}^{D*}$	Maximum $\bar{r}_{inp}^D$ for which $\bar{r}_{PC}^T > \bar{r}_{PC}^D$, given fixed $\bar{r}_{inp}^T$.

Table 2. Meaning of symbols used in the study of resonance and gating.

2.2.4   Data analysis

For each simulation, instantaneous output firing rates, iFR, were computed with Gaussian kernel regression on population spike times using a kernel with 6ms width. Mean population firing rates, $\bar{r}_{PC}$ and $\bar{r}_{IN}$, were computed by averaging iFR over time for PC and IN populations, respectively; they index overall activity levels by the average firing rate of the average cell in the population. Multi-unit activity (MUA) was calculated by averaging voltages across PC populations. The frequency of an output population oscillation, f_{pop}, was identified as the spectral frequency with peak power in Welch's spectrum of the iFR. The natural frequency f_N of the output network was identified as the population frequency f_{pop} exhibited in response to an asynchronous input.

Across simulations varying input frequencies, statistics were plotted as the mean ± standard deviation calculated across 10 realizations. Input frequency-dependent plots of mean firing rates and population frequencies will be called response profiles. The firing rate resonant frequencies, f_R^{PC} and f_R^{IN}, are the input frequencies at which global maxima occurred in the $\bar{r}_{PC}$ and $\bar{r}_{IN}$ firing rate profiles, respectively. Similarly, the resonant input frequency f_R^{pop} maximizing output oscillation frequency was found from peaks in f_{pop} population frequency profiles. In simulations with two outputs, statistics were calculated separately for each output population. The competitive interaction between output populations was quantified by the difference in their mean firing rates.

2.2.5   Simulation tools

All models were implemented in Matlab using the DynaSim toolbox (github.com/DynaSim) (see Appendix A) and are publicly available online at:

github.com/jsherfey/PFC_models. Numerical integration was performed using a 4th order Runge-Kutta method with a fixed time step of .01ms. Most network simulations were run for 2000ms and repeated 10 times. Simulations using rate-coded signals with Gaussian spatial profiles were run for 6500ms. The network was allowed to settle to steady-state before external signals were delivered at 400ms. Plots of instantaneous responses begin at signal onset. The first 500ms of response was excluded from analysis, although including the transient did not alter our results significantly.

2.3 Results

2.3.1 *Strong feedback inhibition produces natural oscillation and inhibitory pacing in E/I networks*

A network of interacting excitatory principal cells and inhibitory interneurons responded to asynchronous input driving E (or PC) cells (Fig. 2.3A) with asynchronous spiking when feedback inhibition was sufficiently weak (Fig. 2.3Bi); however, given strong feedback inhibition, the network became an interneuron-paced oscillator (Fig. 2.3Bii-iii) with a natural frequency, f_N, that depended on the duration of inhibition. A population of asynchronous spike trains to E cells caused a subset to spike and recruit feedback inhibition, silencing the entire population until inhibition decayed sufficiently for the same or a different subset to spike on the next cycle. While the inputs in this study can be asynchronous, the outputs will always be oscillatory due to the natural oscillation produced by the synchronizing effect of strong feedback inhibition. Increasing the duration of inhibition τ_{GABA} increased the period of silence and decreased the natural

frequency f_N (Fig. 2.4A, lower plot). This E/I network mechanism generated fast interneuron-paced gamma and beta oscillations in networks with both classic Hodgkin-Huxley neurons (Hodgkin and Huxley, 1952) and more detailed PFC models (Durstewitz and Seamans, 2002).
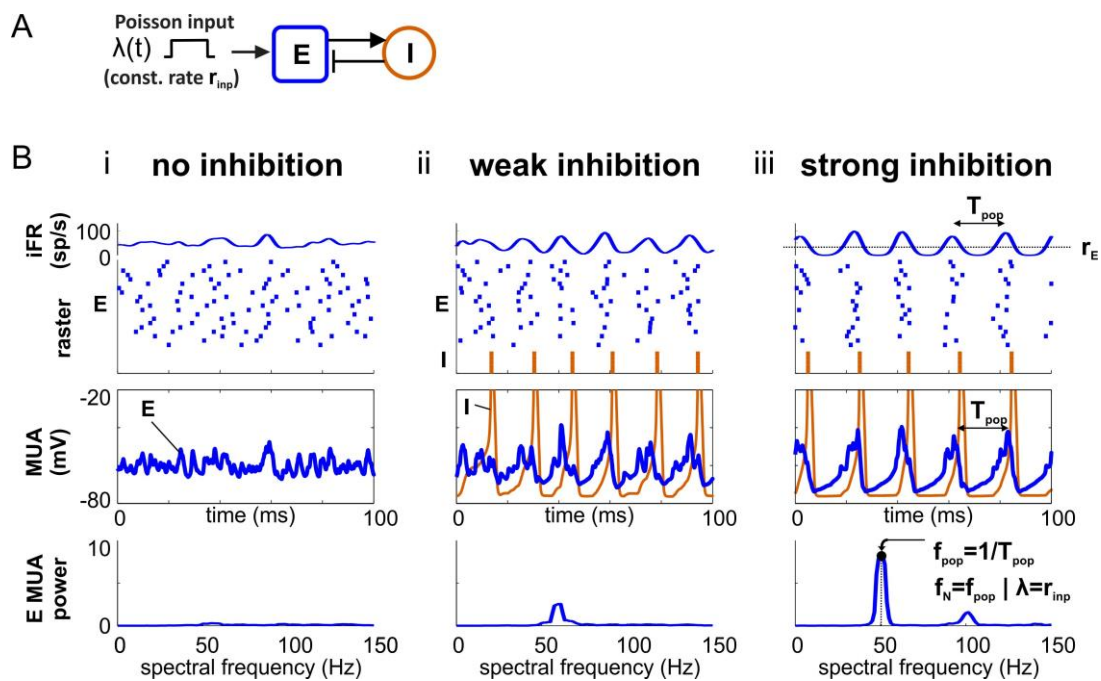
Fig. 2.3. Strong feedback inhibition produces natural oscillation in E/I network. (**A**) Diagram showing feedforward excitation from external (independent) Poisson spike inputs to 20 excitatory (E) Hodgkin-Huxley (HH) neurons receiving feedback inhibition from 5 inhibitory (I) HH neurons. See Fig. 2.1B for details. (**B**) Simulations showing the network switching from an asynchronous to oscillatory state with natural oscillation as the strength of feedback inhibition is increased.

2.3.2   Firing rate resonance in E/I networks

The response to a step input of asynchronous spiking (or noisy current) can be contrasted with the response to an oscillatory input with equal-strength (i.e., equal time-averaged rate $\bar{r}_{inp}$) and sinusoidal frequency f_{inp} (Fig. 2.4Ai, Bi). On each cycle of an oscillatory input only a fraction of PCs spiked before feedback inhibition silenced the entire population. Still, oscillatory inputs produced greater responses than asynchronous inputs because their more synchronous spike trains enabled a larger fraction of more correlated PCs to reach threshold before INs were sufficiently engaged to silence the entire population. The fraction that was able to spike before inhibition silenced the entire population increased for input frequencies around the natural frequency f_N and peaked at f_R^{PC} slightly above f_N (Fig. 2.4Aii, Bii). This increase in PC population response to oscillatory inputs with frequencies near f_N depends on matching periodic drives with the rate-limiting time constants of the driven network (Serenevy and Kopell, 2013). The number of PC cells spiking per cycle decreased beyond f_R^{PC}. This behavior was the same for PC responses to oscillatory inputs with square wave modulation (Fig. 2.5A-B). In contrast to PC rates peaking near f_N, IN firing rates continued to increase until input frequency reached $f_R^{IN} > f_R^{PC}$ (Fig. 2.5B) where the decreasing number of PCs spiking per cycle reached the minimum necessary to induce IN spiking on each cycle. Interestingly, this shows that activity of INs driven exclusively by PCs can continue increasing with the frequency of an oscillatory drive to PCs even when PC activity is decreasing, and consequently, that firing rate resonant frequencies of PC and IN populations can differ.
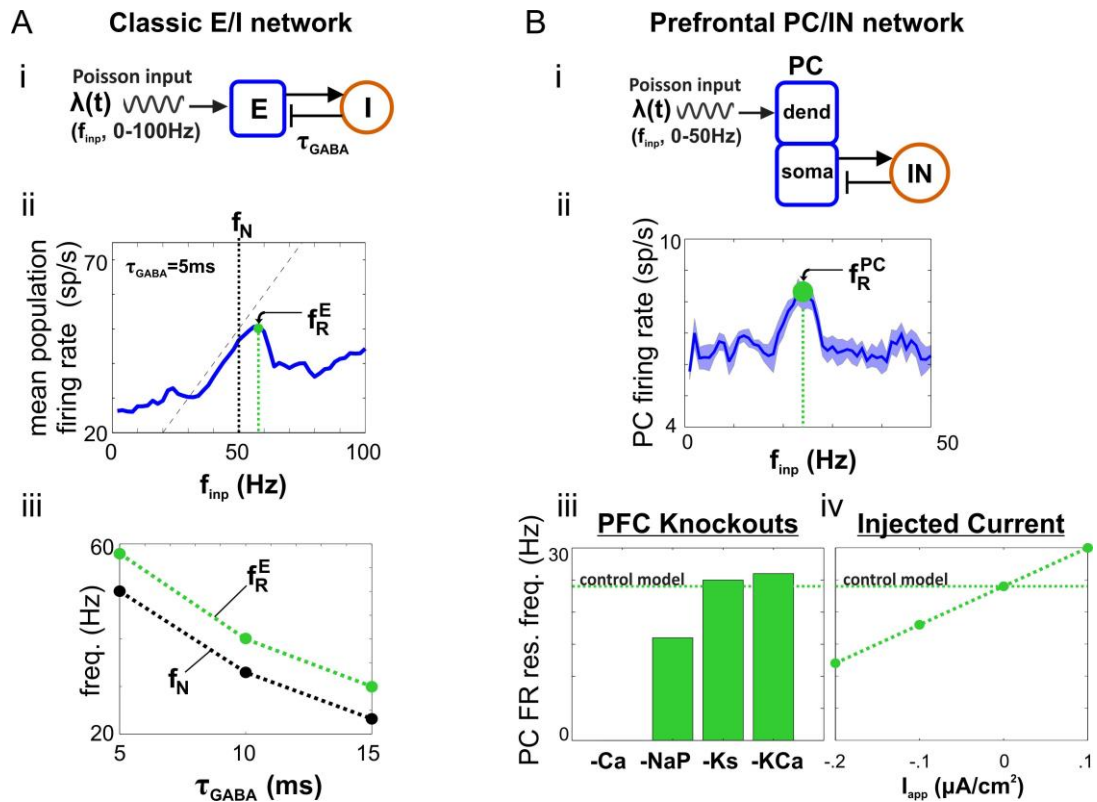
Fig. 2.4. Firing rate resonance and neuromodulation in E/I networks.
(**A**) (Ai) Diagram showing an oscillatory input to a classic Hodgkin-Huxley E/I network (see Fig. 2.1B for details). (Aii) Firing rate exhibits a resonant peak at a gamma frequency. (Aiii) Natural and resonant frequencies decrease with the duration of feedback inhibition. (**B**) (Bi) Diagram showing an external oscillatory Poisson input to the dendrites of 20 two-compartment principal cells (PCs) receiving feedback inhibition from a population of 5 fast spiking interneurons (INs). PC and IN models include additional conductances found in prefrontal neurons (see Fig. 2.1A for details). (Bii) Input frequency-dependent firing rate profile showing resonance at a beta2 frequency. (Biii) The effect of knocking out individual ion currents on the resonant input frequency maximizing firing rate outputs. Removing hyperpolarizing currents (-Ks, -KCa) increased the resonant frequency, while removing depolarizing currents (-NaP) decreased the resonant frequency or (-Ca) silenced the cell altogether (see Fig. 2.1A for ion channel key). (Biv) The effect of hyperpolarizing and depolarizing injected currents, I_{app}, on the resonant frequency mirrored the effect of knockouts on excitability.
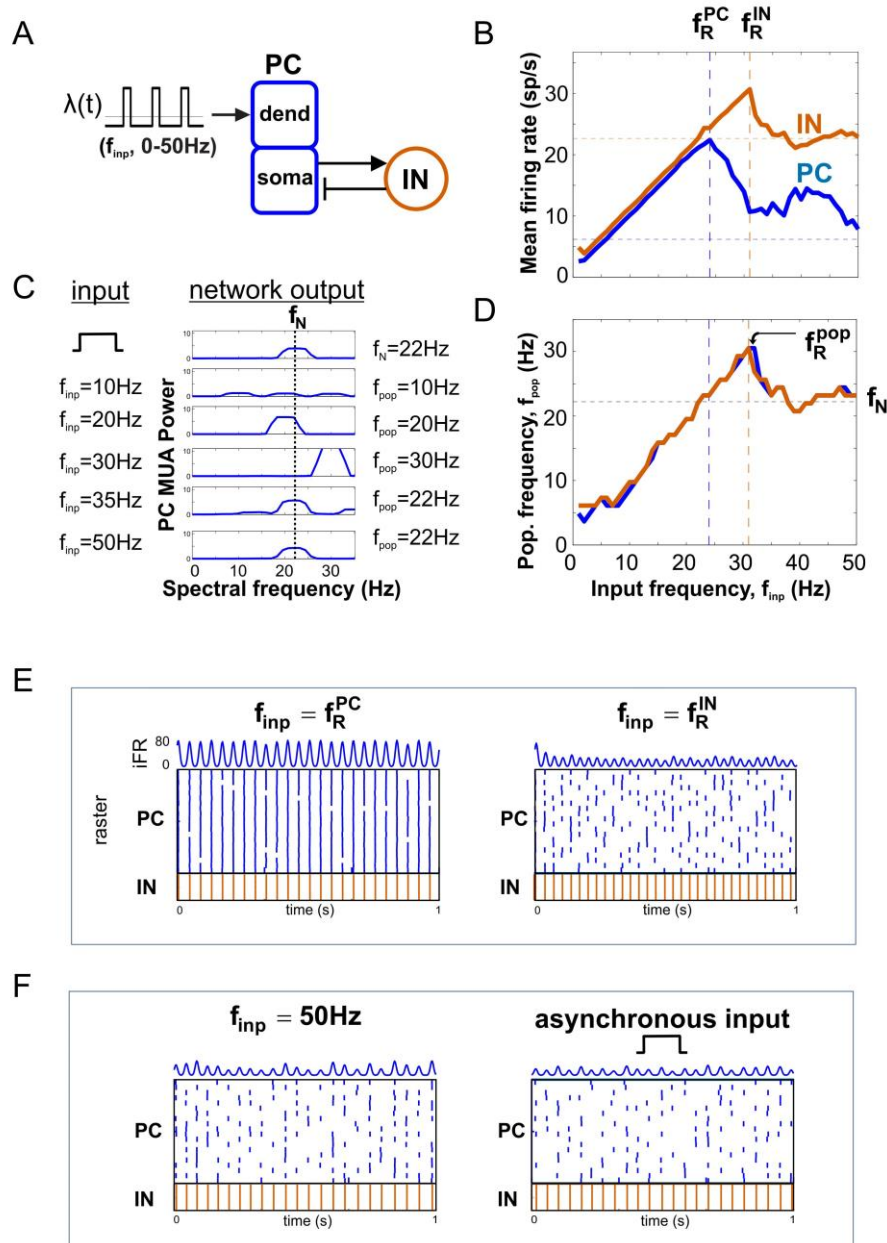
Fig. 2.5. Input frequency-dependent output response profiles.
(**A**) Diagram of PFC network receiving high-synchrony oscillatory input. (**B**) Firing rate (FR) profile for PC (blue) and IN (red) populations. (**C**) Multi-unit activity (MUA) power spectra in response to inputs with different frequencies. Population frequency is quantified by the spectral frequency with peak power. Top and bottom traces show that the network has peak power at the natural frequency for both asynchronous and high-frequency inputs. (**D**) Population frequency profile for PC and IN populations. Peak population frequency occurs at the input frequency maximizing IN activity (i.e., feedback inhibition). (**E**) Spike rasters and PC iFR responses to oscillatory inputs at the PC and IN firing rate resonant frequencies. (**F**) Spike rasters and PC iFR responses to inputs producing network responses paced by internal time constants: (left) asynchronous input, (right) high-frequency input.

2.3.3   Population frequency resonance in E/I networks

At the population level, outputs can be further described by the frequency of population oscillation, f_{pop} (Fig. 2.5C-D). f_{pop} profiles also exhibited a peak at a particular input frequency f_R^{pop}, a phenomenon we will call population frequency resonance. In both our model networks, the population frequency followed the input up to f_R^{IN} then approached the natural frequency as the response became paced by the network's internal time constants   (i.e., $f_R^{pop} = f_R^{IN}$; $f_{pop} = f_{inp}$ for $f_{inp} < f_R^{pop}$, and $f_{pop} \rightarrow f_N$ as $f_{inp} \rightarrow \infty$) (Fig. 2.5D). The population oscillation peaks at f_R^{IN} because the PC population can follow inputs only as long as INs are able to synchronously silence the PC population on each cycle of the input. This yielded the counterintuitive result that the fastest output PC oscillation (but not the highest PC firing rate) occurred at the excitatory input frequency maximizing feedback inhibition.

2.3.4   Firing rate resonance and neuromodulation in PFC networks

All of the qualitative features of the step and frequency responses discussed so far were present in both the classic Hodgkin-Huxley and the detailed PFC models of PC/IN networks with feedforward excitation, strong feedback inhibition, roughly regular spiking PC cells, and fast spiking INs. However, the two network models differed in quantitative details. Cells in different brain regions possess different intrinsic currents that may have different fast time scales for spike generation and alter the overall excitability of the cells. In networks with the Hodgkin-Huxley neurons based on the squid giant axon, the kinetics

and excitability resulted in natural and resonant frequencies well into the gamma-frequency range (Fig. 2.4Aii). Slower sodium kinetics and stronger hyperpolarizing currents (e.g., slow potassium currents) based on rat medial prefrontal cortex resulted in beta-range frequencies (f_N, f_R^{PC}, f_R^{IN}) for the same inputs (Fig. 2.4Bii). Knockout experiments (Fig. 2.4Biii) and injecting applied currents (Fig. 2.4Biv) in the PFC network showed that, in the beta/gamma range, non-spiking currents affected overall activity levels and resonant frequencies similar to tonic inputs that shift baseline excitability (see Discussion for ways modulatory currents might affect single cell responses from cycle to cycle and population responses to slower input frequencies). Thus, brain regions with different membrane conductances (e.g., produced by different ion channel expression profiles) likely differ in the precise frequency of their natural response to asynchronous inputs and the input frequencies at which they resonate, even if the pyramidal cells interact with the same population of interneurons; such profiles can be tuned by neuromodulation.

2.3.5   *Dependence of natural oscillations and resonance on mean input strength*

Stronger inputs (i.e., higher time-averaged rate $\bar{r}_{inp}$) (Fig. 2.6A), delivering larger mean drives to each PC cell, increased the mean output firing rate (Fig. 2.6Bi), natural and peak population frequencies (Fig. 2.6Bii), and input resonant frequencies (Fig. 2.6C). The dependence of f_N on $\bar{r}_{inp}$ implies the natural response is a variable-frequency network oscillation controlled by the strength of input. f_R^{PC} equaled f_N for weak inputs and increasingly exceeded it for inputs with increasing strength; in contrast, f_R^{IN} and f_R^{pop} exceeded f_N for all input strengths (Fig. 2.6C).
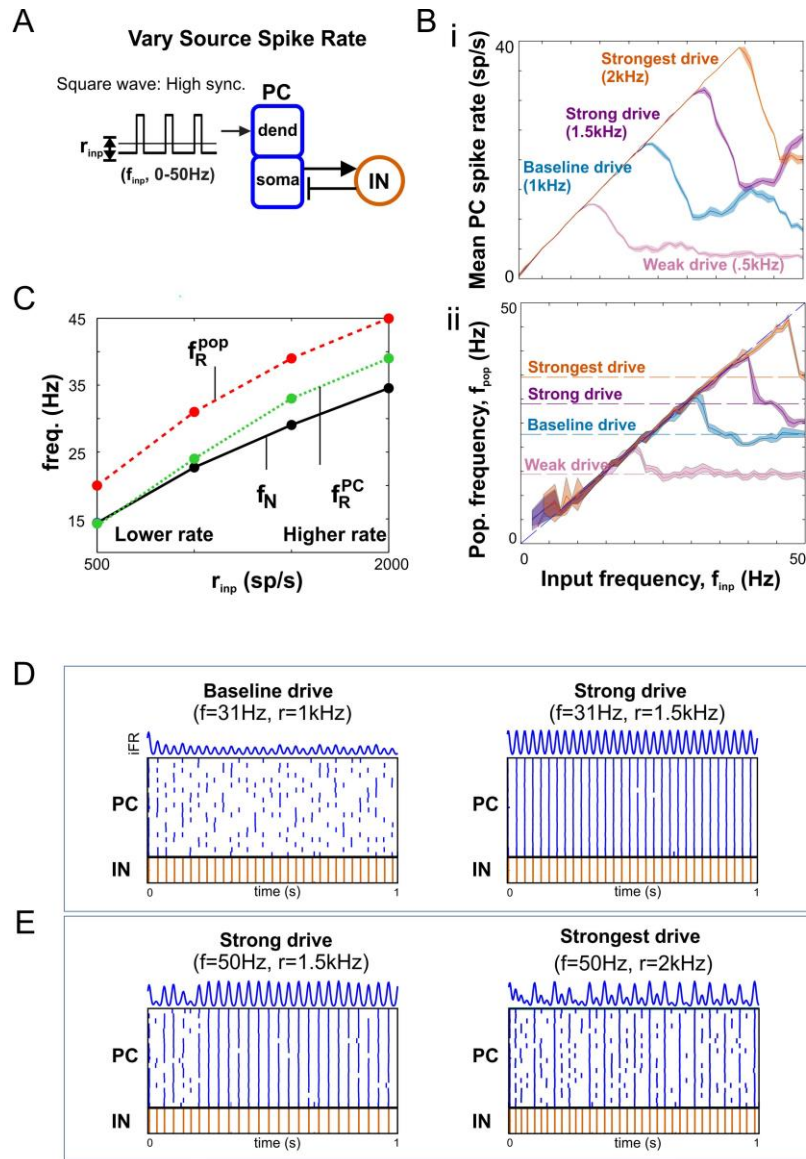
Fig. 2.6. Dependence of response profiles on input strength.
(**A**) Diagram of PFC network receiving variable-strength high-synchrony square wave input. (**Bi**) Firing rate profile for PC populations given oscillatory inputs with different strengths. (**Bii**) Population frequency profile for inputs with different strengths. Horizontal dashed lines mark the natural frequencies for each drive strength. (**C**) The effect of input strength on natural and resonant frequencies. (**D**) Spike rasters and PC iFR responses showing the typical case of stronger input driving more output: (left) weaker input, less output, (right) stronger input, more output. (**E**) Spike rasters and PC iFR responses showing special case of resonance at first harmonic enabling a weaker input to drive more output: (left) weaker input, more output, (right) stronger input, less output.

2.3.6   Dependence of resonance on spike synchrony of oscillatory inputs

More synchronous input oscillations (i.e., smaller δ_{inp}) (Fig. 2.7A) delivering more coincident spikes (i.e., larger instantaneous drives) to each PC cell drove larger fractions of the target population to spike on each cycle before feedback inhibition was recruited to silence it. This enhanced output firing rates $\bar{r}_{PC}$ for all input frequencies and the strength of resonant response (Fig. 2.7Bi) without affecting the resonant input frequency f_R^{PC} maximizing PC firing rates (Fig 2.7Bi; Fig. 2.7C) or the frequency of natural oscillation f_N (Fig. 2.7Bii; Fig 2.7C). In contrast, f_R^{IN} increased with input synchrony because $\bar{r}_{PC}$ remained sufficiently large to engage interneurons for greater f_{inp}; and, since $f_{pop} = f_R^{IN}$, population frequency also increased with input synchrony (Fig 2.7C). Thus, output networks are able to achieve faster network oscillations, produce greater projection neuron output, and recruit more local inhibition when target signal inputs are more synchronous.
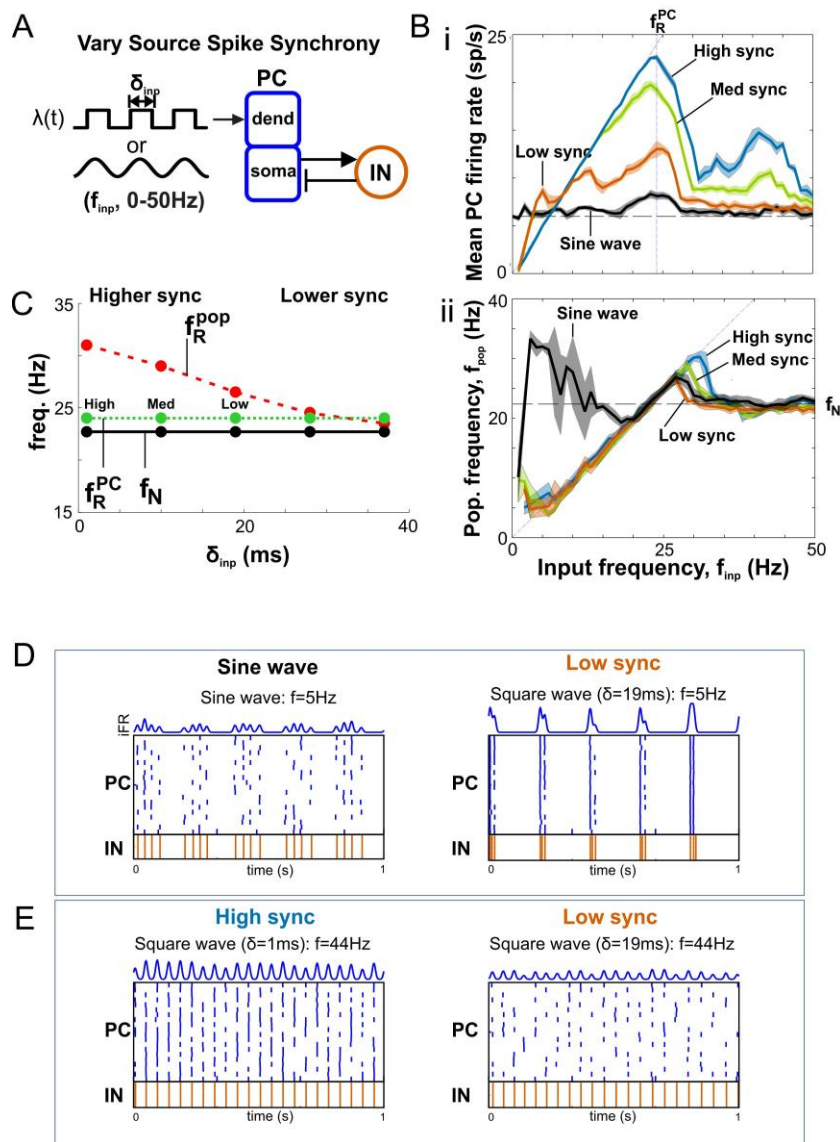
Fig. 2.7. Dependence of response profiles on input synchrony.
(**A**) Diagram of PFC network receiving variable-synchrony square wave or sinusoidal inputs. (**Bi**) Firing rate profile for PC populations given oscillatory inputs with different degrees of synchrony. (**Bii**) Population frequency profile for inputs with different degrees of synchrony. Horizontal dashed line marks the natural frequencies for each degree of synchrony. (**C**) The effect of input synchrony on resonant frequencies. Maximum population frequency (at the IN firing rate res. freq.) increases with input synchrony. (**D**) Spike rasters and PC iFR responses showing the natural nesting of natural oscillations generated by a local network on the depolarizing phase of a lower-frequency external driving oscillation with sine wave (left) or square wave (right) rate-modulation. (**E**) Spike rasters and PC iFR responses showing that weaker firing rate resonance at the first harmonic (i.e., smaller bump at f_{inp}=44Hz in Bi, blue curve) occurs for high synchrony (left) but not low synchrony (right) oscillatory inputs.

2.3.7   Rhythm-mediated competition

Now that we understand how a single output population responds to asynchronous and oscillatory inputs, we can investigate the conditions enabling input oscillatory states to govern selection among competing outputs in parallel pathways. Since outputs are always oscillatory, competition will depend on oscillatory states (i.e., the f_{pop} profile) in addition to the $\bar{r}_{PC}$ profile. For that reason we will refer to the interneuron-mediated interaction between oscillatory output populations as rhythm-mediated competition. We will begin by considering the interaction between target and distractor pathways with a target output driven by an oscillatory input and a distractor output driven by an equal-strength asynchronous input (Fig. 2.8A). Under these conditions, all differences between the output responses result from differences in the dynamical states of the source networks and depend on the frequency and synchrony of the oscillatory target input. The effect of competition on output responses will be assessed by comparing total target and distractor spike output levels with competition to their corresponding control responses without competition (i.e., comparing target output for different input frequencies to the input frequency-dependent $\bar{r}_{PC}$ profile and comparing distractor output to the natural response expected given asynchronous input).

Fig. 2.8B (i.e., Fig. 2.8Ci) shows the mean firing rate response (averaged over time, population, and 10 simulations) of each output (target and distractor; dashed lines mark control responses, i.e., without competition) as the target input frequency of a medium-synchrony ($\delta_{inp} = 10ms$) square-wave oscillation is increased from 1-50Hz. First, we can see that whether output suppression occurs, relative to the control responses,
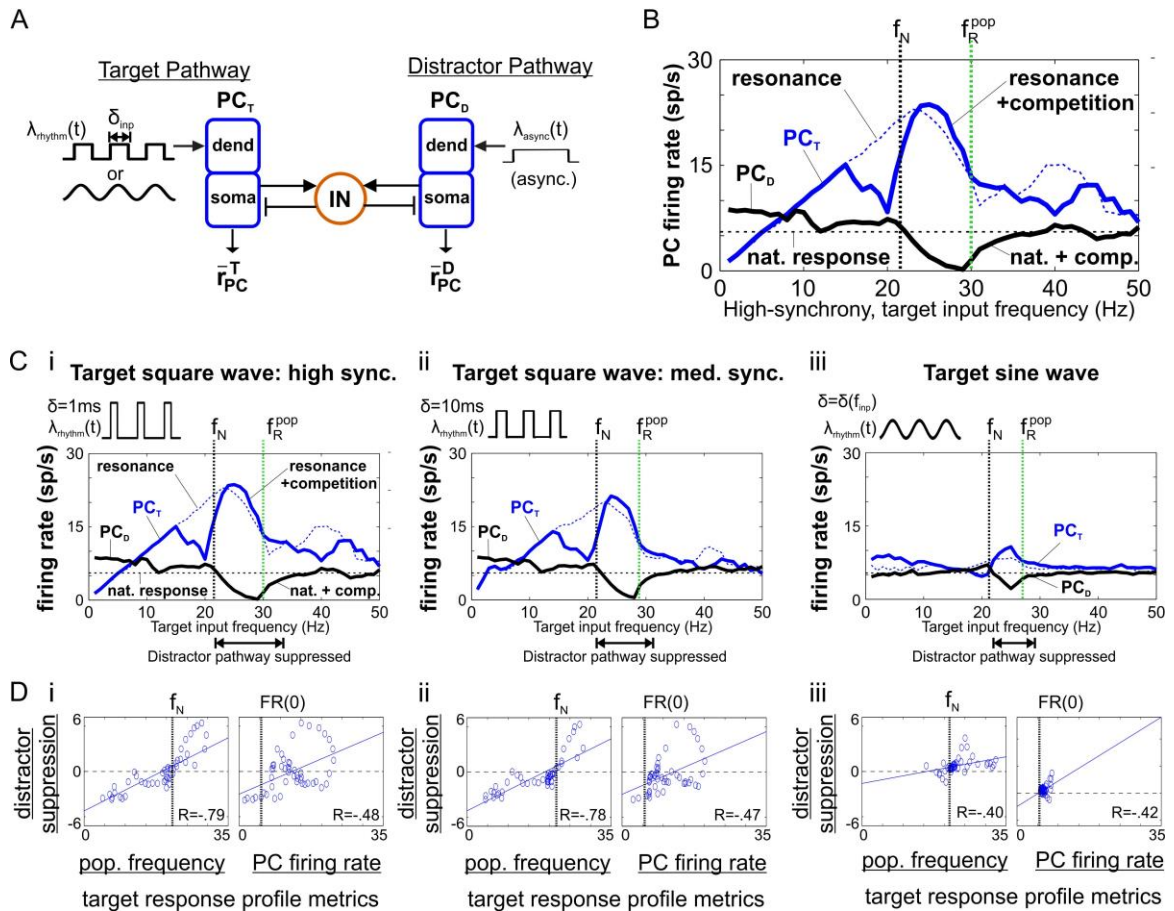
Fig. 2.8. Feedback and lateral inhibition produce rhythm-mediated competition.
(**A**) Diagram showing a rhythmically-driven target population of PC cells (PC$_T$) competing with an asynchronously-driven distractor population (PC$_D$) through a shared population of inhibitory IN cells. Shared INs cause target and distractor outputs to be rhythmic and enable competitive interaction. (**B**) Mean firing rate outputs for target and distractor as target input frequency is increased with high-synchrony, square wave rate-modulation. (**C**) Mean firing rate outputs given target inputs with (i) high-synchrony (reproduced for comparison), (ii) medium synchrony and (iii) sine wave rate-modulation. (**D**) The amount of distractor suppression relative to the natural response plotted against the target control responses (i.e., firing rates and population frequencies expected in the target based on input frequency-dependent response profiles in Figs. 6-7).

and which output is suppressed when it does occur depends on the frequency of the

oscillatory target input (compare regions where the solid lines are below the dashed

lines). The target output (solid blue line) is suppressed relative to its $\bar{r}_{PC}$ profile (dashed

blue line) when it receives beta-frequency inputs (12-22Hz) that are slower than the natural frequency of the distractor output ($f_N = 22\text{Hz}$). Despite being suppressed relative to its $\bar{r}_{PC}$ profile, in absolute terms, the total number of spikes produced in the target output exceeds the total number produced by the distractor in the opposing pathway. At the same time, the total number of spikes produced by the distractor stays near its control response (i.e., its overall activity level is not disrupted by the output with more spikes).

Instead, the distractor output is suppressed when the target output is driven by oscillatory inputs with a range of frequencies (22-35Hz) faster than the natural frequency of the distractor (22Hz). Fig. 2.8Di plots distractor suppression (i.e., deviation from the natural control response) versus target control responses (i.e., output population frequency and firing rates expected from the f_{pop}- and $\bar{r}_{PC}$-profiles, respectively). These plots show that distractor suppression occurs every time the target output is oscillating more quickly than the distractor output. These results hold for square wave target inputs with different degrees of synchrony (Fig. 2.8Ci-ii, 8Di-ii) and for sine wave inputs (Fig. 2.8Ciii, 8Diii). Thus, output suppression is determined most strongly by the relative frequencies of the oscillating outputs: the output population oscillating more quickly tends to suppress the more slowly oscillating output relative to its control response.

Since peak output frequency increased with input synchrony (Fig. 2.7C), synchrony also increased the range of input frequencies over which the target output oscillates faster than f_N and suppresses the distractor (Fig. 2.8Cii). Furthermore, since local inhibition is maximal at the peak frequency, distractor suppression increases as target inputs approach the f_{pop}-resonant frequency. Importantly, synchronous oscillatory

inputs near (and slightly below) the f_{pop}-resonant frequency were able to drive their targets to fully suppress competing distractors; this complete distractor suppression enables resonant inputs to mediate frequency-based output selection even when asynchronous inputs would otherwise produce significant responses. This confirms that input oscillatory states can control flexible gating among competing outputs driven by equal-strength inputs.

2.3.8   *Four modes of rhythm-mediated competition*

An examination of the instantaneous firing rates of the output populations (Fig. 2.9; Fig. 2.9S) with targets driven by medium-synchrony square wave inputs (Fig. 2.9A) reveals that there are four patterns of interaction that can unfold over time: continuous suppression of one output, periodic suppression of one output, alternating suppression between two outputs, and no suppression of either output. Which form of interaction occurs over time depends on differences between inputs and differences between the abilities of outputs (PC populations) to drive their shared INs. The ability to drive an IN population depends on how frequently an output delivers a collective pulse of excitation (determined by the output population frequency) and the strength of each pulse (determined by the number of spikes across the output population per cycle and the synchrony of those spikes within a given cycle).
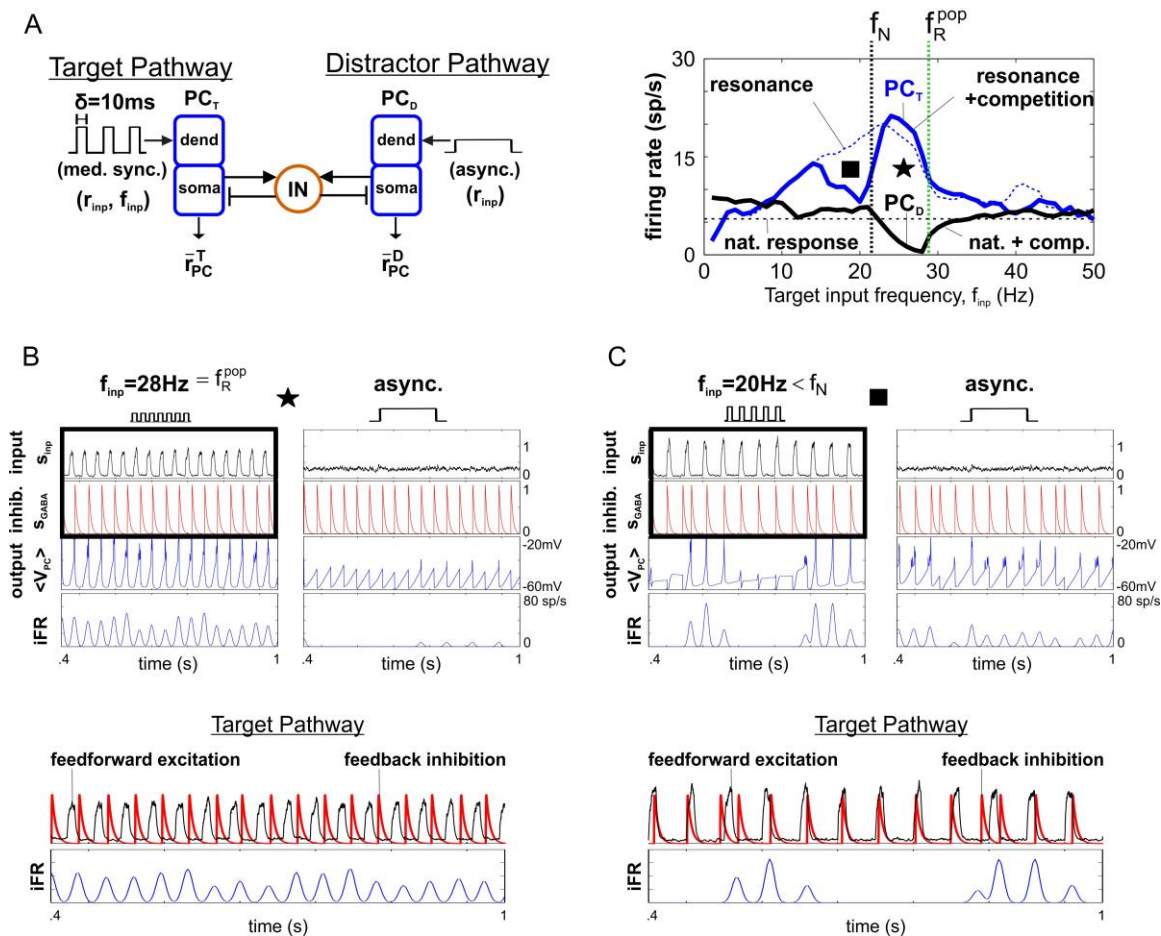
Fig. 2.9. Rhythm-mediated competition supports continuous and periodic suppression.
(**A**) (left) Diagram showing target driven by medium-synchrony oscillatory input in competition with an asynchronously-driven distractor. (right) Same as plot 7Bii with markers at input frequencies with representative responses. (**B**) Example simulation with continuous suppression of the Distractor Pathway. Bottom plots show phase locking between feedforward excitation and feedback inhibition. (**C**) Example simulation with suppression alternating between target and distractor. Bottom plots show that the lower-frequency output (Target) becomes transiently active when feedforward excitation arrives sufficiently late in the cycle after the decay of lateral/feedback inhibition.
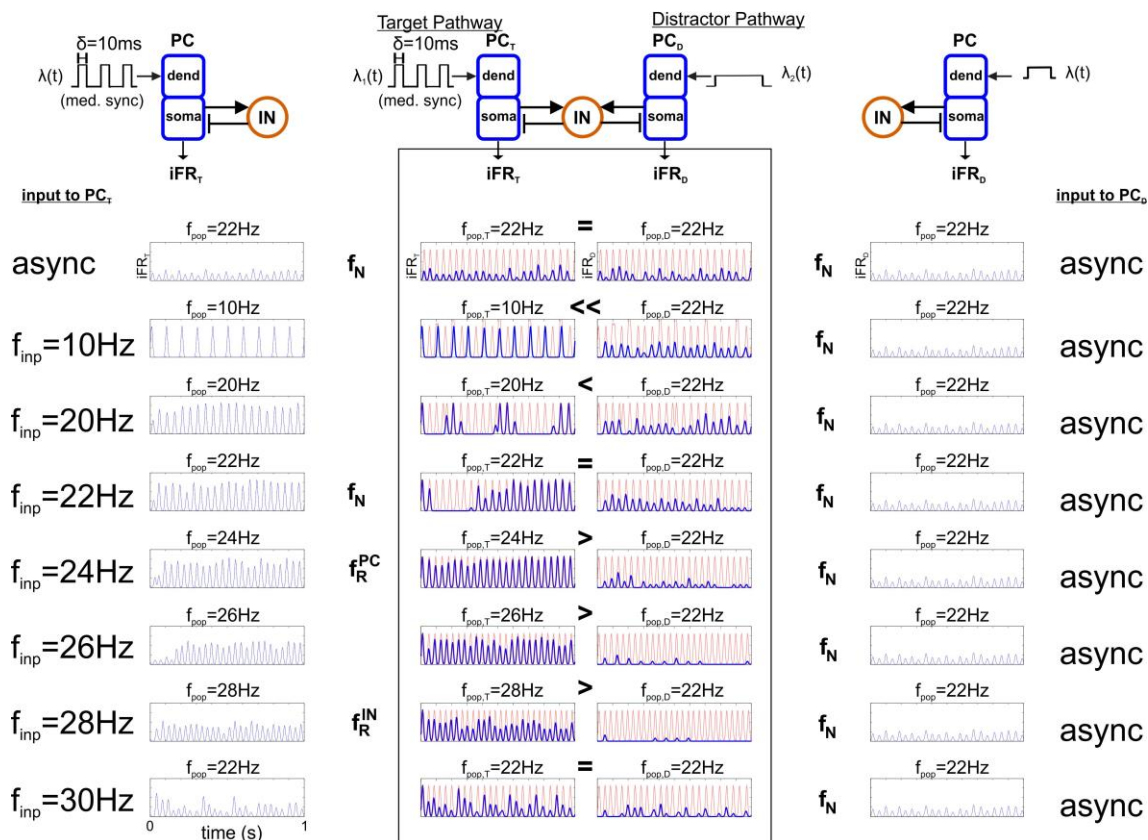
Fig. 2.9S. Instantaneous firing rates with and without lateral inhibition.
(top) Diagrams of single and competing outputs receiving medium-synchrony inputs. (bottom-left) PC iFR response to oscillatory input. (bottom-right) PC iFR response to asynchronous input. (bottom-middle) Overlay of PC (blue) and IN (red) iFR responses for Target and Distractor Pathways with different frequency target inputs. Examples demonstrate different modes of rhythm-mediated competition: (async. vs. async.) no suppression in either output, (f_{inp}=20Hz vs. async.) alternating suppression, (f_{inp}=20Hz vs. async.) continuous suppression.

The only way to fully block the output of a pathway in our model (i.e., to achieve complete distractor suppression) is for an opposing output to drive its continuous suppression through interneuron-mediated lateral inhibition. As we have seen previously, without opposition, a single output always oscillates and delivers periodic pulses of excitation to INs at the population frequency. In contrast, when multiple outputs are coupled to the same INs, the output population with the highest frequency oscillation (i.e., the output receiving the most f_{pop}-resonant input) most frequently drives IN cells, tends to phase lock with them, and suppresses spiking in output populations oscillating more slowly (i.e., outputs receiving less f_{pop}-resonant inputs). A rhythmically-driven output oscillating faster than the natural oscillation will always drive INs to continuously suppress responses to asynchronous distractors because the former recruits interneuron-mediated lateral inhibition on each cycle of its oscillatory input with a period shorter than that required for the latter to reach threshold (Fig. 2.9C, see membrane potential plot).

In contrast, when a more slowly-oscillating output is rhythmically-driven, it is capable of overcoming lateral inhibition transiently if it receives a sufficiently strong excitatory pulse after the decay of lateral inhibition and before the opposing population spikes again (Fig. 2.9D). If transient activation of a slower output is able to cause IN cells to spike and suppress the faster population, this dynamic gives rise to alternating suppression (switching between the two outputs); otherwise suppression is periodic and experienced only by the more slowly oscillating output. (Cannon and Kopell, 2015)

There is no suppression in either output when their activities are statistically indistinguishable for driving the IN population. In such cases, the outputs respond as if

they belong to the same pathway. This occurs when both populations receive equal-strength asynchronous inputs or at least one receives an oscillatory input with a frequency well above the natural frequency. When both output populations receive asynchronous inputs they respond as one population since there is nothing to distinguish their drives to INs in the output layer. Similarly, as the frequency of an oscillatory input becomes large and the output population becomes paced by its internal natural time constants, its population response becomes indistinguishable from other populations driven by high-frequency or asynchronous inputs.

Since we are interested in gating outputs from PFC in this work, we will focus on resonant beta/gamma inputs that support output selection with continuous (absolute) suppression of competing distractors.

2.3.9 *Resonant bias for frequency-based output selection*

Fig. 2.10 shows how resonant biases can perform frequency-based output selection among parallel pathways. Two pathways are shown with source networks in different dynamical states delivering an equal number of spikes to distinct output populations. The source network in the Target Pathway has a low-synchrony oscillation while the source network in the Distractor Pathway has asynchronous spiking. The oscillatory target input has an approximately f_{pop}-resonant 25Hz frequency (i.e., a frequency that maximizes the output population frequency). The target output driven by a resonant input oscillates faster than the natural frequency and results in continuous suppression of the distractor output. This demonstrates that resonant inputs can selectively activate their outputs while achieving suppression of opposing outputs

through rhythm-mediated competition, even when the competing population is also
rhythmic.

Parallel pathways

In-context
Target Pathway

Out-of-context
Distractor Pathway

Pathway 1

Pathway 2

$f_{inp} = f_R^{pop} (= \beta_2)$

Low sync

$\lambda_1(t)$

$\lambda_2(t)$

Inputs:
(e.g., from L3 PFC)
WM Reservoir:

0   .5s

0   .5s

S

S

**L5 PFC
Output Network**

PC_T **IN** PC_D

R_1

R_2

Outputs:
(e.g., to Striatum)

PC_T index

0   .5s

PC_D index

0   .5s

Rule-dependent
S→R mapping

Distractor
Suppression
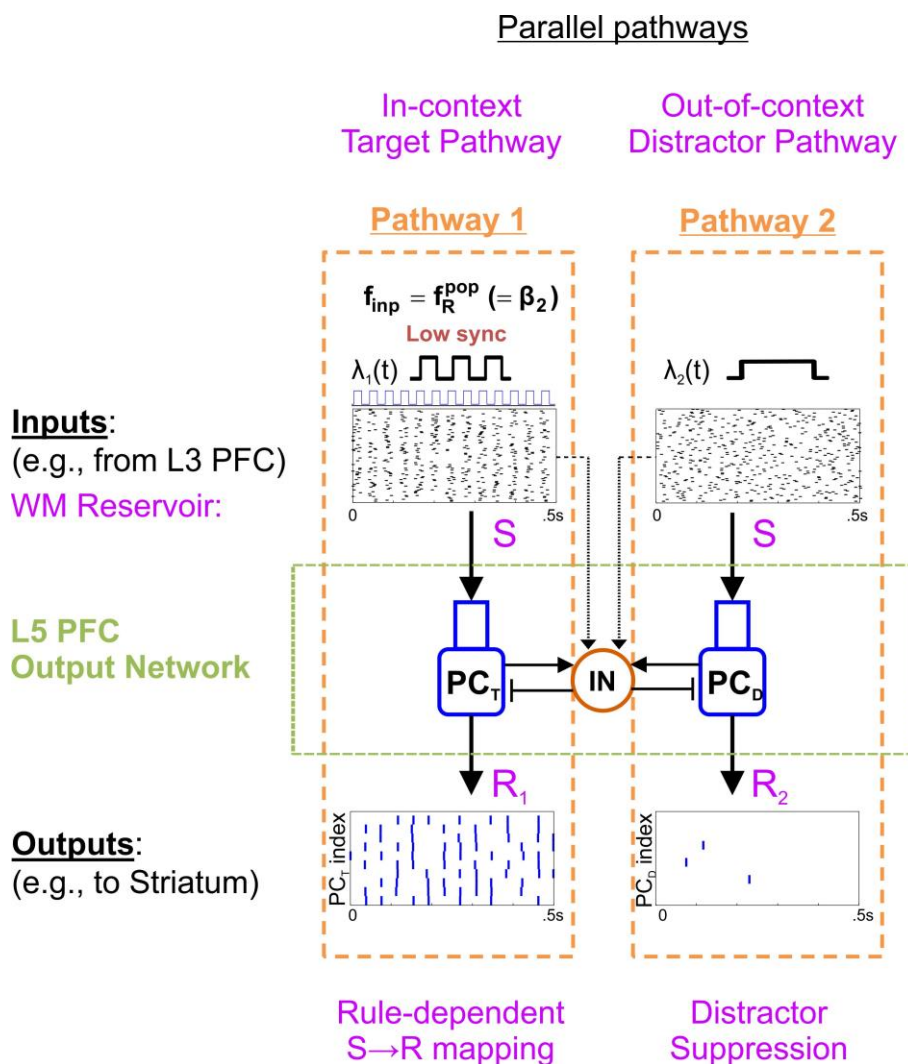
Fig. 2.10. Resonant bias supports rule-based stimulus-response mapping.
Example simulation showing two pathways (i.e., alternative stimulus-response mappings)
with superficial layer inputs and deep layer outputs. One pathway has a resonant input that
drives its output population while the other pathway has an asynchronous input and output
that is suppressed by interneuron-mediated lateral inhibition. When both inputs represent
different dimensions of the same stimulus (S) and outputs map onto alternative action plans
(R_1, R_2), context-dependent rhythmicity in a select input population can provide adequate
bias for rule-based selection of stimulus-response mapping.

2.3.10   Strength of resonant bias

A resonant bias is useful for frequency-based output selection to the extent that it can overcome input rate differences that would result in the selection of a different output. The selection mechanism can be called frequency-based as long as the output driven by a weaker input can be selected over a stronger input; otherwise selection is rate-based. To investigate the ability of resonant biases to overcome input rate differences, we compared the firing rates of two competing outputs, one driven by a weaker target oscillation and the other driven by a progressively stronger asynchronous distractor (Fig. 2.11A). We compared results for target inputs at the f_{pop}- and $\bar{r}_{PC}$-resonant frequencies, $f_R^{pop}(\delta_{inp}^T)$ and $f_R^{PC} = 24\text{Hz}$, respectively, for different degrees of input synchrony δ_{inp}^T (sine wave and square waves with high, medium, or low synchrony). In all cases, the mean target input rate $\bar{r}_{inp}^T = r_{rhythm}$ was held constant while the mean distractor input rate $\bar{r}_{inp}^D = r_{async}$ was increased across simulations up to twice the strength. The strength of resonant bias was quantified in two ways: (1) by how much more target output is produced (i.e., $\Delta\bar{r} = \bar{r}_{PC}^T - \bar{r}_{PC}^D$) when target and distractor input strengths are equal (i.e., y-axis crossing in Fig. 2.11B-C), and (2) the strongest distractor input for which there was greater target output, $\bar{r}_{inp}^{D*}$ (i.e., x-axis crossing in Fig. 2.11B-C).

In all cases, the target output had a higher mean firing rate any time it had a faster population frequency: $f_{pop}^T > f_{pop}^D = f_N(\bar{r}_{inp}^D)$. The distractor advantage that could be overcome by a weaker resonant target input increased with the oscillation frequency of

the target output (compare responses for different degrees of target input synchrony in Fig. 2.11B). In contrast, the maximal distractor strength that could be overcome by a more weakly driven target depended only slightly on the $\bar{r}_{PC}$ profile (i.e., $\bar{r}_{inp}^{D*}$ increases less with PC firing rate in Fig. 2.11D than with pop. frequency in Fig. 2.11E). As target input synchrony increased from low to high (i.e., δ_{inp}^{T} from 19ms to 1ms) (Fig. 2.11B), the maximum target output frequency increased from approximately 26Hz to 30Hz, enabling f_{pop}^{T}-resonance to confer an advantage overcoming distractor inputs that were 30% to 70% stronger. On the other hand, the extent to which the target output exceeded the equal-strength distractor output (i.e., $\Delta\bar{r}$) depended exclusively on the $\bar{r}_{PC}$ profile (i.e., not the population frequency) and increased 4x as input synchrony increased (see $\Delta\bar{r}$ in Fig. 2.11D-E, first row; $\Delta\bar{r}$ is correlated with PC firing rate but not pop. frequency).

In summary, as the strength of distractor input increased, both f_{pop}- and $\bar{r}_{PC}$-resonant inputs resulted in greater target output firing rates as long as the target output oscillated with a higher frequency than the distractor output. This enabled a highly synchronous f_{pop}^{T} -resonant input to drive greater output than a 70% stronger asynchronous input to an opposing population. Thus, resonant biases provide a competitive advantage capable of overcoming significant input rate differences in service of frequency-based output selection.
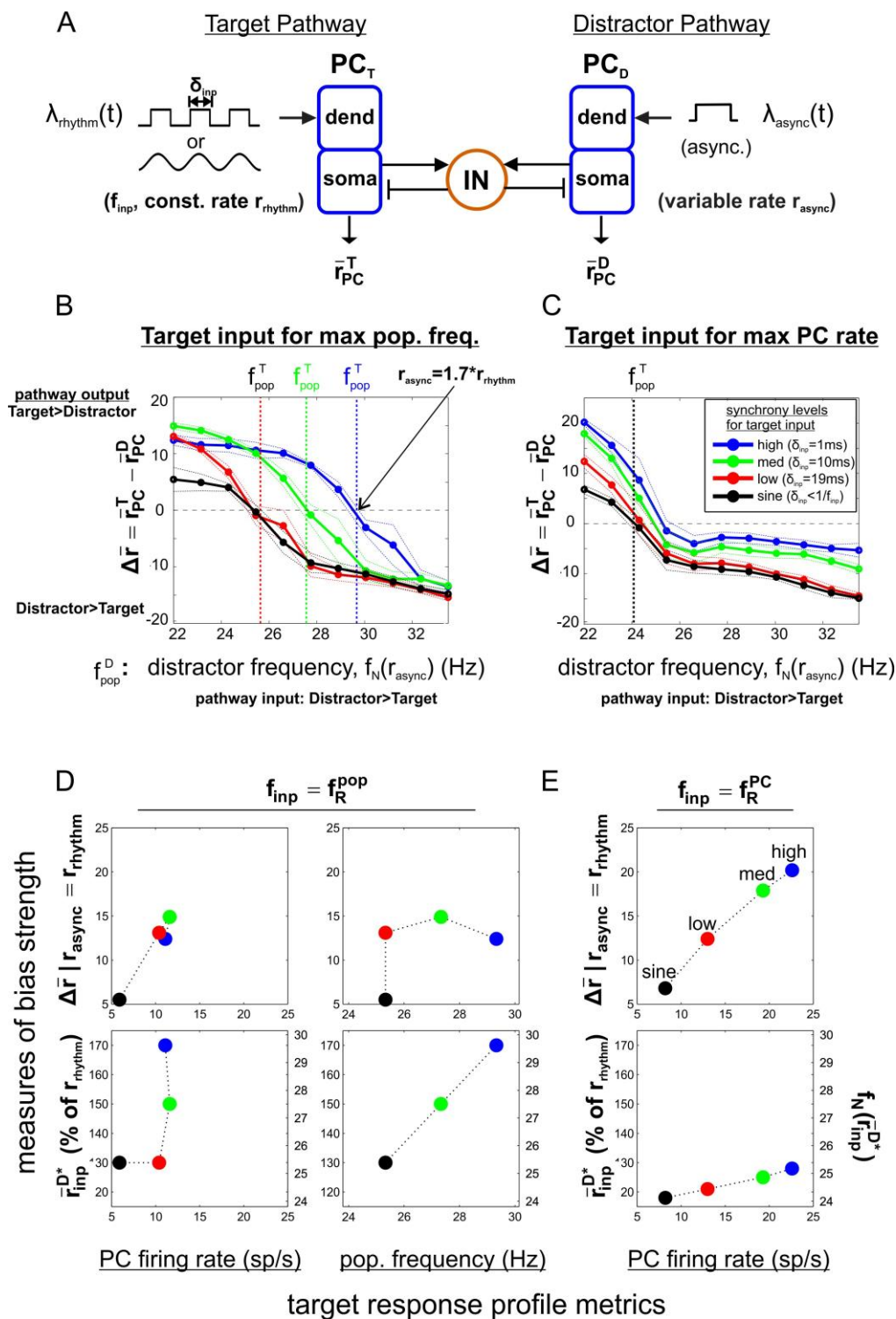
Fig. 2.11. Resonant bias enables suppression of stronger distractor pathways.
(**A**) Diagram showing target output (PC$_T$) receiving variable-synchrony input in

competition with a distractor output (PC$_D$) receiving variable-strength asynchronous input. (**B**) Differential output firing rates (target-distractor) as asynchronous input rate (i.e., output natural frequency) increases for target input frequencies maximizing output population frequency given different degrees of input synchrony. (**C**) Similar to (B) except target input frequencies are chosen to maximize output PC firing rate. (**D**) Measures of bias strength for results in (B) plotted against the firing rates expected in the target based on response profiles. (**E**) Measures of bias strength for results in (C) plotted against the firing rates and population frequencies expected in the target based on response profiles. r$_a$* is the maximum asynchronous distractor input rate where target output exceeds distractor output. r$_T$-r$_D$ is the differential output firing rate when target and distractor mean input rates are equal.

2.3.11   *Amplifying resonant bias for winner-take-all selection*

Resonant biases fully suppressed competing responses driven by equal-strength distractors, but the response to progressively stronger distractors increased steadily until the output populations oscillated at the same frequency. Winner-take-all (WTA) dynamics are known to amplify rate differences and result from a combination of strong lateral inhibition and recurrent excitation (Kaski and Kohonen, 1994). We asked whether flexible frequency-based output biases could be amplified by within-population recurrent excitation to produce stable WTA output selection. To test this, we added strong AMPA and NMDA synapses (see Methods for details) between all cells within each output population and compared input cases that previously resulted in $\Delta \bar{r} > 0$ and $\Delta \bar{r} < 0$. Specifically, we drove a target output with a f_{pop}-resonant medium-synchrony oscillation and a distractor output with either 40% stronger or 60% asynchronous input. Fig. 2.12A compares results with and without recurrent excitation when the distractor receives a 40% stronger input. As expected, the small output rate difference favoring the target output
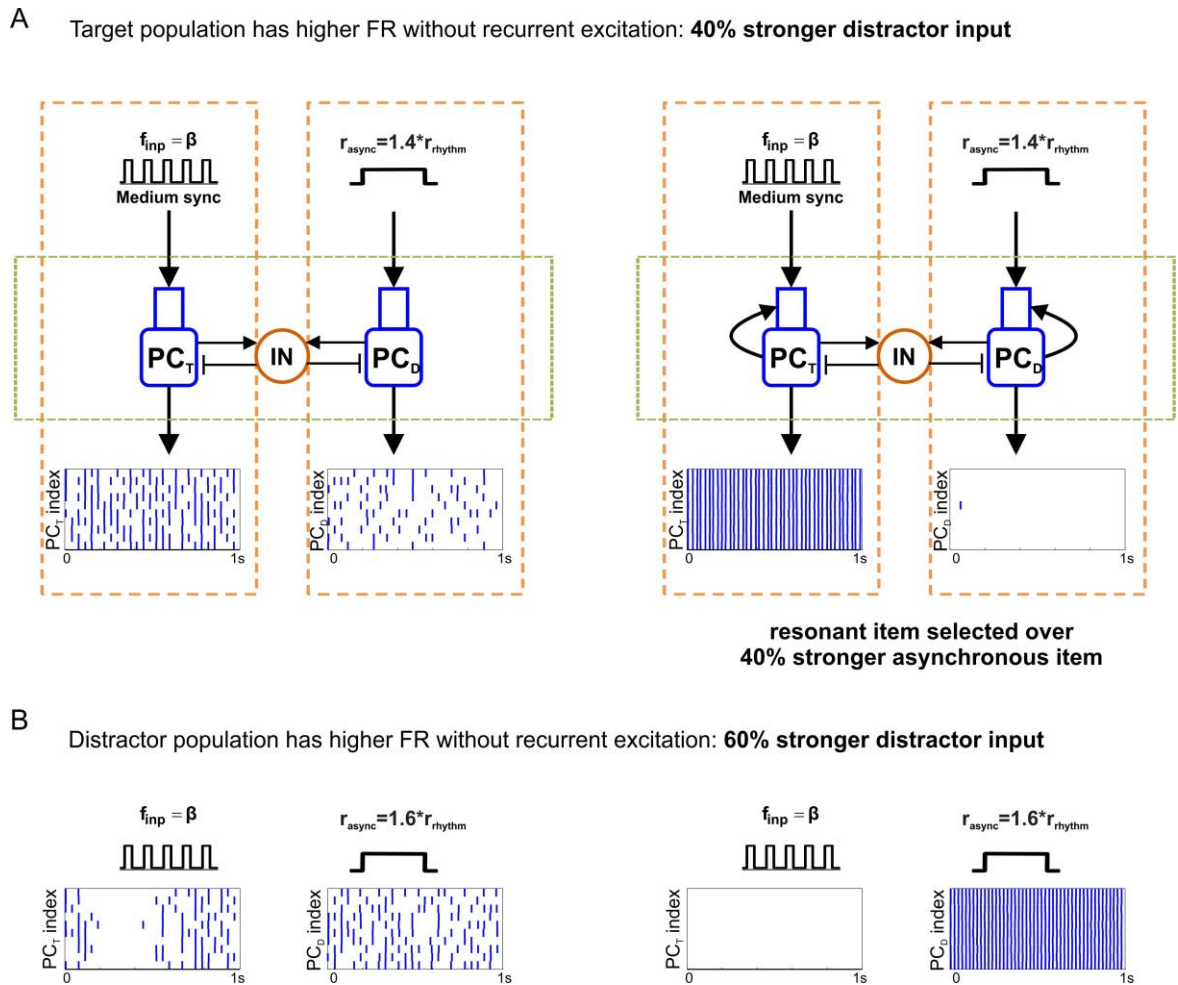
Fig. 2.12. Recurrent excitation amplifies output differences for winner-take-all selection.
(**A**) (left) Without recurrent excitation, target output is greater despite the distractor receiving a 40% stronger input. (right) Recurrent excitation amplifies resonant bias producing winner-take-all dynamics that select the output driven by a weaker resonant input. (**B**) (left) Without recurrent excitation, distractor output is greater when it receives an asynchronous input that is 60% stronger than an opposing resonant input. (right) Target is suppressed when the asynchronous input drives greater output.

was amplified so that only the target output was active. In contrast, when the asynchronous input was 60% stronger, the rate difference was amplified in favor of the distractor (Fig. 2.12B). Thus, synaptic plasticity within output populations can amplify flexible resonance-mediated biases to produce robust frequency-based output selection.

2.3.12 Pathway switching by flexibly tuning output resonance

The results so far suggest that the resonant properties of output populations determine the input frequency that is most effective at suppressing responses to opposing signals. We have shown suppression between target and distractor outputs driven by oscillatory and asynchronous inputs, respectively. We have also shown that resonant properties can be tuned by varying the overall level of excitation in an output population (Figs. 2.4B, 2.6C). Next we investigated whether suppression of the slower output oscillation occurs when both inputs are oscillatory and whether the frequency producing selective response can be modulated by tuning resonant properties.

To test this, 25Hz beta- and 40Hz gamma-frequency medium-synchrony oscillations were input to two competing output populations (Fig. 2.13A). Given baseline excitation, individual outputs can follow a 25Hz oscillation but oscillate near the natural frequency in response to a 40Hz oscillation (Fig. 2.7D). As expected, in competition the output receiving the more f_{pop}-resonant 25Hz input suppressed the competing population as if the latter was oscillating at the natural frequency in response to an asynchronous input. In a second simulation, the f_{pop}-resonant frequency was increased to more than 40Hz using an auxiliary asynchronous input (a nonspecific "switch" signal) with the appropriate strength (i.e., a mean rate of 1000 sp/s based on Fig. 2.6C) delivered to both

output populations. In this case, the population receiving the 40Hz input suppressed the competing output driven by a less resonant input (Fig. 2.13B). These simulations demonstrate that resonant biases can select outputs when both inputs are oscillatory and that nonspecific inputs can have specific effects on output selection by tuning which input frequencies are resonant and thus selectively propagated.
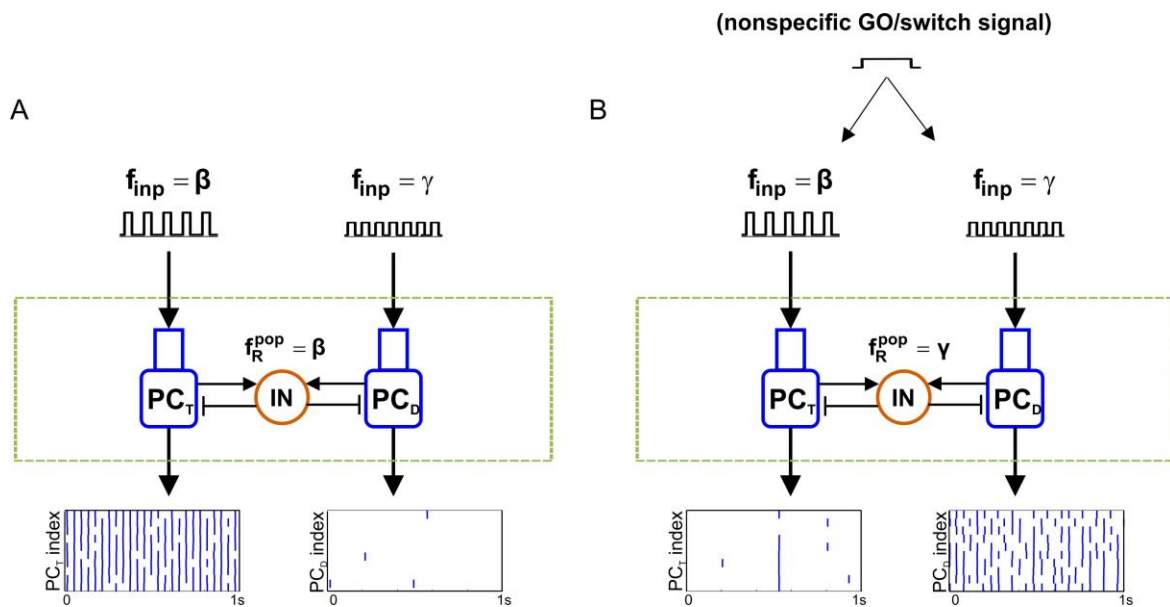
Fig. 2.13. Nonspecific inputs can tune output resonance for switching between specific beta- and gamma-rhythmic pathways.
(**A**) A resonant beta input suppresses the response to a less resonant gamma-frequency input. (**B**) A nonspecific asynchronous input to both output populations shifts their resonant frequency to the gamma-range, causing the output layer to select the gamma-rhythmic input and suppress response to the less resonant beta input.

2.3.13   Resonant bias for selecting rate-coded signals among parallel pathways

A frequency-based output selection mechanism is useful for gating rate-coded signals only if a spatial pattern of firing rates across a source population can be reflected in the output. So far we have only considered input signals with uniform spatial profiles (i.e., spike trains with spatially uniform time-averaged rates). Next we examined whether resonant biases can gate rate-coded signals among parallel competing pathways with non-uniform Gaussian spatial profiles.

To make sure output resonant properties were the same as before, the maximum input rate (i.e., peak of the Gaussian bump) was set to the level that previously produced beta-resonance given a uniform profile. Inputs with the maximum rate were delivered to a sufficient number of PC cells to recruit inhibition like before. All other PC cells of a given output received input spike trains with lower mean rates but identical oscillatory state (either 25Hz or 40Hz medium-synchrony square waves) (Fig. 2.14).

Two rate-coded signals with Gaussian profiles were approximately conserved in the spatial pattern of output firing rates in separate populations when both inputs were modulated at the resonant frequency (25Hz) (Fig. 2.14A). In contrast, when one input was modulated at a less resonant frequency (40Hz), the input with resonant modulation was conserved in its output population while the competing output was fully suppressed (Fig. 2.14B). This confirms that the prior results hold when input signals have non-uniform population rate-codes; in other words, the resonance-mediated mechanism for frequency-based output selection supports gating of rate-coded signals.
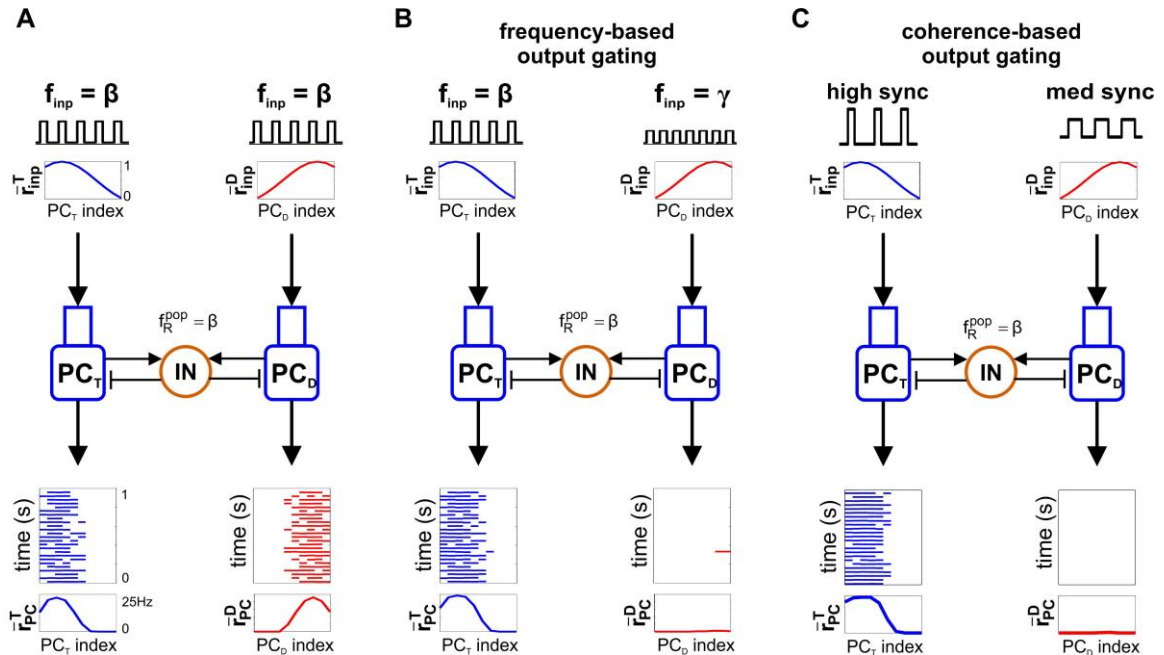
Fig. 2.14. Resonant bias supports frequency- and coherence-based gating of rate-coded signals among parallel pathways.
(**A**) Outputs of two pathways reflect the spatial pattern of firing rates across their inputs when both inputs are embedded in resonant oscillations. PC index represents linear indices of cells in a given output PC population. (**B**) Frequency-based output gating: More resonant rate-coded signals suppress less-resonant rate-coded signals. (**C**) Coherence-based output gating: Increasing input synchrony in one pathway suppresses response in a competing pathway driven by a less synchronous equal-frequency oscillation.

Experimental work has demonstrated that rule-coding populations in a task with two rules both exhibit beta-frequency oscillations with greater synchrony in the population encoding the active rule (Buschman et al., 2012). Motivated by this experimental observation, we tested interactions between outputs driven by equal-frequency oscillations differing only in synchrony. When the inputs were high- and medium-synchrony square waves with 25Hz resonant oscillations, the higher synchrony

input drove its output while suppressing the response to the lower synchrony input (Fig. 2.14C). This demonstrates that changes in input synchrony can bias output selection among parallel pathways with important implications for how task-related modulation of synchrony can direct rule-based action selection (see Discussion).

2.3.14 *Resonant bias for selecting rate-coded signals among convergent pathways*

The gating of outputs among parallel pathways can be contrasted with the gating of responses in a single output population receiving concurrent signals from convergent pathways. We have shown that lateral inhibition driven by a resonant output gives rise to periodic inhibition that blocks responses in opposing pathways. Next we tested the hypothesis that feedback inhibition can similarly block responses to less resonant rate-coded signals when pathways converge on a single output population. Similar filtering has been demonstrated in simpler models with uniform input rates (Cannon et al., 2014).

We repeated the previous simulations demonstrating frequency-based gating of rate-coded signals, except this time we delivered both inputs to the same population (Fig. 2.15). In this case, two rate-coded signals with Gaussian profiles and resonant 25Hz modulation were approximately conserved in the spatial pattern of output firing rates in a single output population (Fig. 2.15A). In contrast, when one input was modulated at a less resonant gamma frequency (40Hz), the input with resonant modulation was conserved in the output while the response to the less resonant signal was blocked by feedback inhibition as hypothesized (Fig. 2.15B). Asynchronous rate-coded signals were similarly blocked when resonant inputs from a convergent pathway resulted in the target population phase-locking with local interneurons (Fig. 2.15C). In both cases, feedback

inhibition prevented mixing of signals in a common target of convergent pathways when one pathway carried a resonant signal.
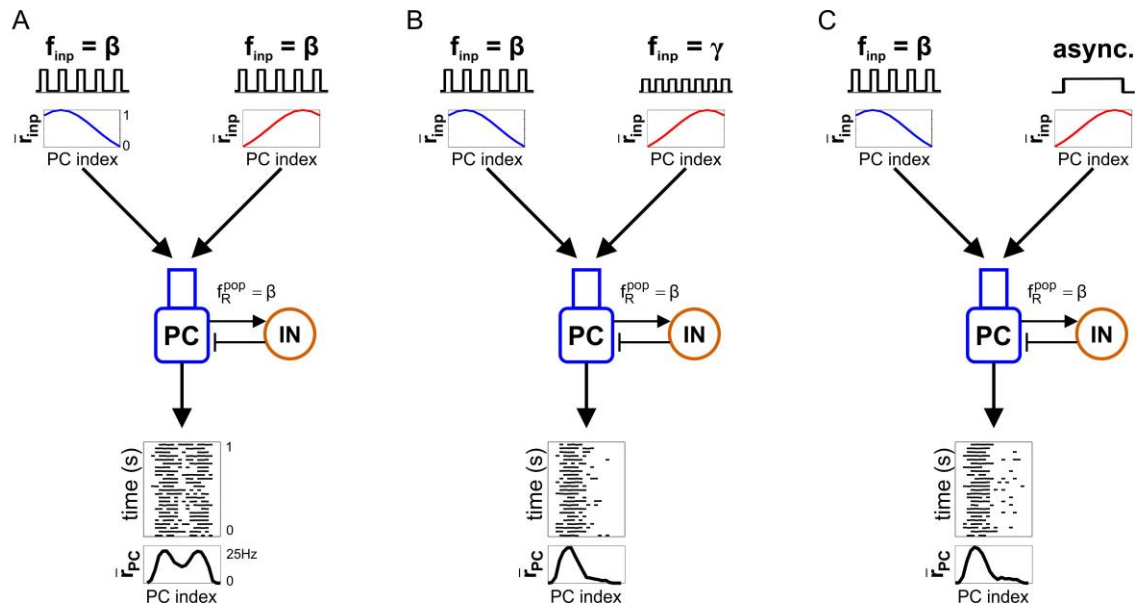
Fig. 2.15. Resonant bias supports frequency-based gating of rate-coded signals among convergent pathways.
(**A**) Similar to Fig 2.14A except both inputs converge on a single output population that reflects the approximate sum of the input signals in its spatial pattern of firing rates. (**B**) A less resonant gamma-frequency signal is blocked from the output population. (**C**) An asynchronous signal is blocked from the output population.

2.4   Discussion

We have presented a novel mechanism for flexibly gating outputs to control functional connectivity between regions connected through parallel or convergent anatomical pathways. The mechanism relies on input oscillations and shared inhibitory cells producing resonance and competitive interactions in an output layer. Output

populations driven by source networks with resonant oscillations phase lock with inhibitory cells and continuously suppress the responses of competing populations among parallel pathways as well as responses to less resonant signals among convergent pathways. The mechanism supports frequency- and synchrony-based output selection of population rate-coded signals; it enables signals to be encoded in firing rates while signal routing is independently directed by the dynamical states of source networks and output resonant properties. However, it does not require bandpass filter networks and thus supports input rate-based output selection in the absence of oscillatory input signals. Together, these properties make resonant biases useful for mediating adaptive control of dynamic signal routing, available on demand with the ability to augment or constrain underlying rate-based processes.

2.4.1   *Frequency-based output selection with rhythm-mediated competition*

In the absence of oscillatory signals, competing populations driven by asynchronous inputs tend to oscillate at natural frequencies in proportion to their input firing rates (Fig. 2.6C). The faster output population engages shared interneurons more frequently and continuously suppresses the more weakly-driven output. This results in output selection among parallel pathways mediated by input firing rates (i.e., rate-based selection) (Borgers et al., 2008). In contrast, resonant oscillatory inputs can induce oscillatory responses with frequencies higher than the natural frequency given equal-strength input. This enables outputs driven by weaker resonant target signals to suppress responses to stronger asynchronous distractors as long as the target frequency exceeds that of the distractor output. Our simulations demonstrated that high-synchrony resonant

target signals can produce greater output than distractors with 70% higher input firing rates. This resonant bias can be amplified for winner-take-all selection by plasticity of recurrent connections that strengthen output responses (e.g., across repeated trials of task). Such resonant biases result in output selection among parallel pathways mediated by input frequencies (i.e., frequency-based selection) (Fig. 2.16A). Furthermore, resonant biases support frequency-based output selection among converging pathways in a similar way.

In principal, this same mechanism could operate on flexible sub-populations within a pathway if participation in a resonant oscillation could be controlled with sub-population precision. For instance, given an input layer of pyramidal cells with different firing rates, an effective encoding population (i.e., the population of cells whose spikes activate downstream neurons) can be flexibly defined by selectively synchronizing subsets in a resonant oscillation; only the input layer cells with spikes contributing to the resonant oscillation will drive cells in the output layer, and only their firing rates will be reflected in the downstream output (Fig. 2.16B). The responses to other cells spiking in the input layer will be suppressed by rhythm-mediated competition in the output layer. In this way, synchronization of input cell ensembles can flexibly constrain encoding populations and the consequent signals read-out from an output layer. Such a mechanism requires a high degree of control over which cells are synchronous with the population oscillation.

A) flexible oscillation-based gating for parallel pathway selection using resonant biases
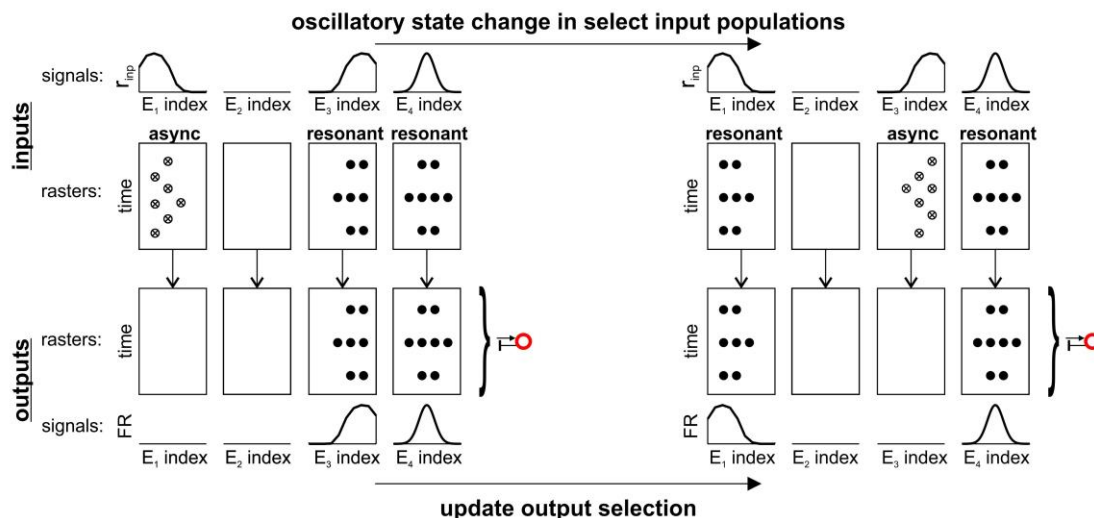
B) flexible oscillation-based gating for output signal transformation using resonant biases

Legend
○ silent cell
⊗ cell is asynchronous relative to other cells in the same layer
● cell participates in a resonant oscillation
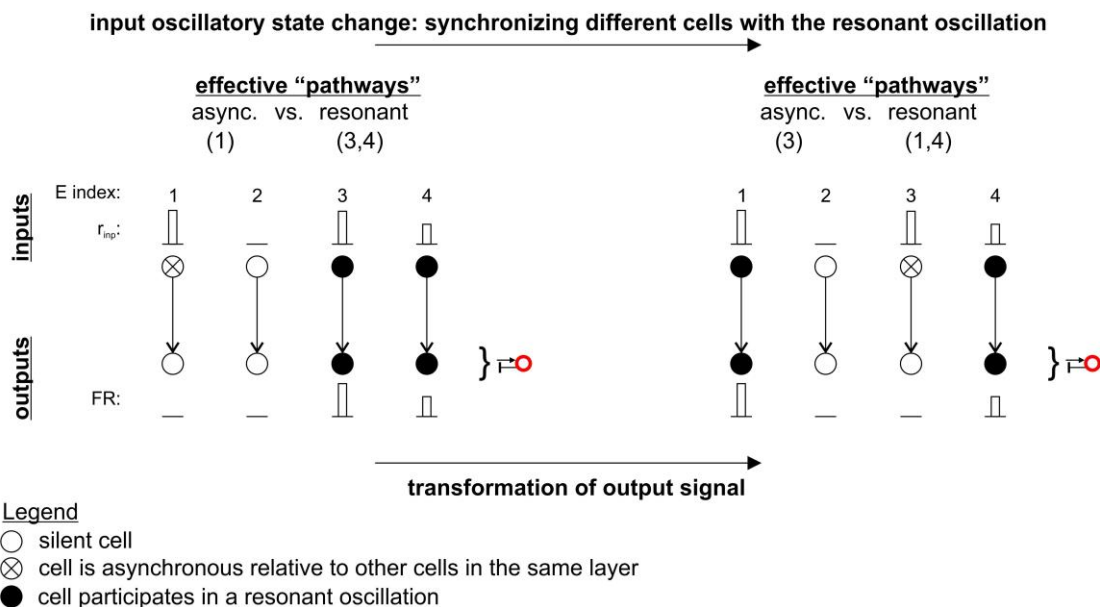
Fig. 2.16. Utility of resonant gating among parallel pathways.
(**A**) Resonant biases can flexibly gate signals among multiple parallel pathways. E_x index represents indices of excitatory cells (e.g., PCs) in pathway x. Pathways with resonant inputs transfer their rate-coded signals while suppressing responses to less resonant inputs in opposing pathways. Controlling input resonance at the population level can control which pathways have signals that are effectively transferred. (**B**) Similarly, resonant biases can determine which input cells have their activities reflected in the output layer of a single pathway. The effective representation that can be read-out from the output layer can be transformed by changing which cells in the input layer produce spikes that are coherent (i.e., synchronous) with the resonant oscillation.

2.4.2 Mechanisms for flexible routing using resonant bias

Output selection using resonant biases is based on establishing the proper correspondence between the dynamical state of source networks and the resonant properties of downstream outputs driven by them, both of which can be flexibly tuned without synaptic plasticity and without disrupting rate-coded signals. Signal routing can be flexibly controlled to the extent that input oscillatory states and output resonant properties can be flexibly tuned.

Controlling which input has a resonant oscillatory state: We have seen for interneuron-paced PC oscillations that synchrony is a function of the strength of feedback inhibition (Fig. 2.3), and population frequency is a function of inhibition duration (Fig. 2.4A). By having two competing interneuron populations that can alternately pace rhythms in the same PC population, differential drives to the interneuron populations could switch the same PC population between different frequencies and degrees of synchrony. For instance, this could be achieved in cortical layers (e.g., layers 2/3 in DLPFC) containing both parvalbumin-positive (PV+) and calbindin-positive (CB+) interneurons which are known to be driven by distinct inputs (Medalla and Barbas, 2009). While this mechanism allows rapid input oscillatory state switching, it is relatively nonspecific and would be limited to gating population signals. More precise mechanisms, presumably tuned by experience-dependent plasticity, would be required to control which cells participate in resonant oscillations.

Controlling which oscillatory state is resonant: Flexible control of output resonant properties can be achieved in numerous ways including varying the overall level

of excitation in the target population through neuromodulation (Fig. 2.2B) (e.g., modulation of potassium currents in PFC by dopamine (Dong and White, 2003) and acetylcholine (Bloem et al., 2014)), external applied currents (Fig. 2.2B), or by varying the strength of the oscillatory input (Fig. 2.6C).

Correspondence between input and output resonant frequencies might be facilitated by oscillation-pacing interneuron types (Sohal et al., 2009) that are present in both input and output layers and provide inhibition with the same time constants (e.g., PV+ fast spiking INs found in layers 3 and 5 of DLPFC (Povysheva et al., 2008; DeFelipe, 1997)).

2.4.3   *Prefrontal anatomy supports rhythm-mediated competition*

Rhythm-mediated competition in neocortex occurs when PC populations are driven by different inputs while being connected to the same local interneurons. In prefrontal cortex, parallel feedforward and/or feedback inputs from different brain regions target the apical dendrites of layer 5 pyramidal output populations with inhibitory interactions mediated by fast spiking interneurons in the output layer. Parallel pathways have been traced from visual and auditory cortices to lateral PFC (Barbas et al., 2015), and different PFC subregions form parallel loops through different subregions of basal ganglia and thalamus (O'Reilly and Frank, 2006). Gating of flows through these parallel pathways could be governed by the oscillatory state of source networks distributed throughout the brain. Selecting different outputs from PFC using resonant biases could dynamically organize functional connectivity, for instance, linking conditions encoded in source networks to appropriate responses based on downstream target populations in subcortical structures biasing attention and action control.

2.4.4   Prefrontal rhythms can select outputs from a working memory buffer

In addition to serving functional connectivity between different regions of cortex, resonant biases could select outputs among interlaminar pathways. In general, signals in superficial layers of cortex send feedforward projections to deep layers with outputs projecting to subcortical structures. Superficial PFC networks exhibit both asynchronous and oscillatory activity during delay periods of working memory (WM) tasks and are widely believed to encode WM representations (Fuster, 1988; Wang, 1999). Beta-rhythmic phase coding has been shown to segregate multiple items in a visual WM task (Siegel et al., 2009) while beta and gamma power increases have been observed in proportion to the number of items stored in WM (Roux et al., 2012) and with cognitive demand (Basar-Eroglu et al., 2007). By maintaining distinct item representations in a superficial layer (i.e., a WM buffer) that target PC populations in a deep output layer, resonant biases utilizing observed beta- and gamma-frequency oscillations could gate outputs from WM. Resonant oscillations could gate the output of select items even when other less-resonant items are stored with stronger activation (e.g., items stored in asynchronous rate-codes with 70% higher mean firing rates). The selected items would then be available in an oscillatory state for read-out in subcortical structures and participation in closed-loop processing. One way this could be controlled with appropriate temporal precision is through a basal ganglia-mediated input gate that selectively targets interneurons responsible for selective PC synchronization; a similar mechanism has been proposed for gating inputs to PCs in PFC (Frank et al., 2001).

Consistent with this hypothesized mechanism for dynamic routing of WM representations, beta-synchrony has been observed between PFC and higher-order thalamus during a WM task and was correlated with performance (Parnaudeau et al., 2013). Our results suggest that beta-rhythmic synchrony may serve thalamocortical processing by effectively selecting the relevant pathways and suppressing distractors. Suppression of responses to asynchronous inputs has the additional benefit of suppressing uncorrelated background activity, which increases the signal-to-noise ratio in the output layer. The loss of this noise suppression mechanism when beta-synchrony was disrupted could underlie the increase in errors observed by Parnaudeau et al. (2013). Without rhythmicity, outputs are rate-based with asynchronous background noise potentially contributing as much to output selection as asynchronous rate-coded signals.

A recent study by Lundquist et al. (2016) demonstrated increased gamma-rhythmic activity late in the delay when WM needed to be decoded for directing action. By activity-dependent tuning of output resonance, event-driven increases in input strength to the output layer mediated by an auxiliary nonspecific "GO" signal could facilitate the resonant propagation and decoding of such gamma-rhythmic response-related activity (Fig. 2.13). At the same time, the asynchronous and less resonant population signals in the superficial layer would be unaffected and held online for potential future read-out from WM.

2.4.5 *Prefrontal rhythms can select rule-based actions*

Beta-rhythmic synchrony has been observed in populations coding task-specific rules (Buschman et al., 2012). We have shown that synchronous beta-frequency

oscillations can selectively gate the read-out of items from a WM buffer. To understand the implications of beta-rhythmicity in rule-coding populations, consider two input items in a WM buffer representing different dimensions (e.g., color and orientation) of the same stimulus (e.g., a colored bar) while the two output populations driven by them are pointers to different action plans (saccade left and saccade right). In this scenario, context-dependent mechanisms (e.g., inputs to superficial CB+ cells) selectively synchronizing the rule-specific stimulus dimension in a resonant beta oscillation could constrain the response to the appropriate context-dependent action plan (Fig. 2.10). This would enable rule-sensitive oscillatory state control mechanisms operating on items in the input layer to select stimulus-response mappings depending on the active context or rule (see Section 2.5 for demonstration). For instance, two input items could represent the categories "blue" and "horizontal" while separate control mechanisms selectively synchronize all items in the WM buffer representing color categories in the color context or all items representing orientation categories in the orientation context. The presentation of a horizontal red bar would then select different output actions depending on the context-dependent synchronization. Rule updating via oscillatory state control mechanisms operating in PFC could potentially be directed by contextual inputs from hippocampus (Komorowski et al., 2013), error signals from ACC (Kerns et al., 2004; Amiez et al., 2005), or BG gating mechanisms (Frank et al., 2001).

2.4.6   *Frequency-based gating mechanisms for convergent pathways*

Frequency-based gating through a single output population with strong feedback inhibition (Fig. 2.17A) investigated here differs from frequency-based gating through a

spiking filter network based on feedforward inhibition (Akam and Kullmann, 2010) (Fig. 2.17B) in that the former allows responses to all inputs with preferential selectivity for those with resonant oscillatory states while the latter responds exclusively to firing rate resonant inputs. Therefore, gating with strong feedback inhibition allows for greater flexibility in the kind of signals that can be transmitted while still supporting the selective response to oscillatory inputs. Furthermore, gating with feedback inhibition supports rate-based output selection of asynchronous rate-coded input signals that can be overridden by frequency-based selection with resonant biases when particular input populations are selectively synchronized at the appropriate resonant frequency.
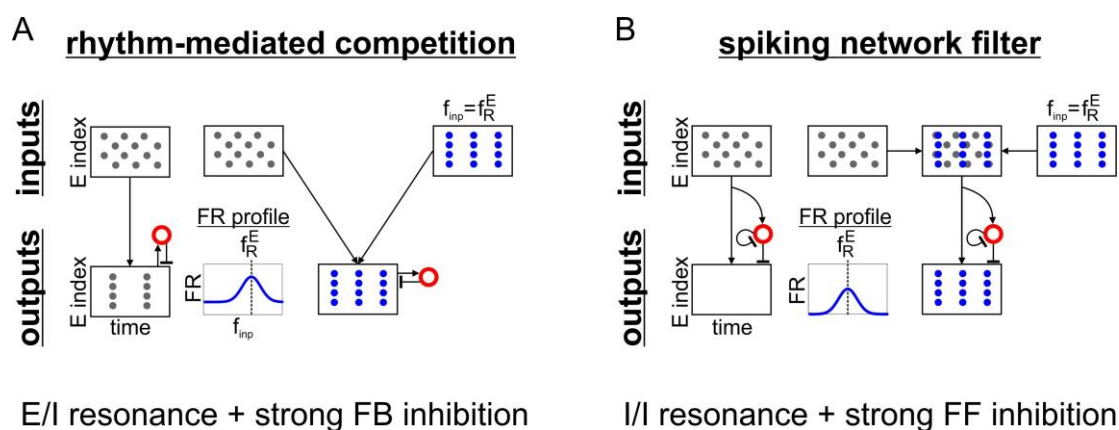
Fig. 2.17. Comparison of frequency-based gating mechanisms for convergent pathways.
(**A**) Outputs with feedback inhibition enable resonant biases to gate which signals among convergent pathways are reflected in an output population. In the absence of input oscillations, convergent signals can be mixed in the output or selected based on differences in firing rates. (**B**) Outputs with strong feedforward inhibition from a resonant inhibitory population respond selectively to oscillatory inputs with frequencies in a particular range. Collectively, such a configuration functions as a spiking network filter that suppresses asynchronous activity and performs frequency-based output selection.

2.4.7 Limitations and future directions

The most significant limitation of the current work is the exclusion of feedforward inhibition. PCs receiving feedforward (especially perisomatic) excitation may be coupled to local interneurons receiving collateral excitatory inputs from the same sources. When the collateral drives to INs balance the drives to PCs the PC/IN network functions as a bandpass filter with PCs remaining silent in response to asynchronous input (Akam and Kullmann, 2010). We have focused on a regime with strong feedback and lateral inhibition to investigate competition between local populations and excluded feedforward inhibition so that asynchronous inputs would have a maximal impact on PC spiking. As feedforward inhibition is increased, local populations become less influential over local interneurons and PC responses to asynchronous inputs are suppressed. In intermediate regimes, the firing rate response profile shifts downward with decreasing resonant frequencies as feedforward inhibition increases. More work is needed to explore the effects of intermediate levels of feedforward inhibition on output competition mediated by feedback and lateral inhibition. However, the mechanism reported here should hold to a degree as long as interneurons can be driven by local populations over external inputs and oscillatory output responses remain paced by local inhibition.

Another important limitation of the present work pertains to the role of modulatory intrinsic currents. We have focused on regimes where PCs are roughly regular spiking and INs are fast spiking. It is unclear how the mechanism reported here would be affected by PCs that are intrinsically bursting (as observed in deep layers of cortex and thalamus) and INs exhibiting low-threshold spiking. Furthermore, our account

of the effects of knocking out modulatory currents is limited to effects on overall activity levels across the PC population and responses to inputs in the beta and gamma frequency ranges. Preliminary simulations suggest that local maxima in the response profiles, especially in lower frequency ranges, may depend on these modulatory currents. Furthermore, work by Olufsen et al (2013) shows that modulatory currents can impact the cycle-to-cycle probability of individual cells participating in the population rhythm.

2.4.8   Conclusions

Resonance and interneuron-mediated competition enable network oscillations to select and route information through parallel and convergent pathways. This mechanism enables the dynamical state of network activity to mediate functional connectivity throughout the brain. Its dynamic nature makes it an ideal way for prefrontal systems to achieve flexible control of cognitively-relevant neural dynamics.

2.5   Superficial LPFC dynamics for interneuron-mediated rule switching

Next, we sought to demonstrate the utility of this oscillation-based routing mechanism in a simulated rule-based task using a model motivated by the laminar structure of prefrontal cortex. We built on two ideas discussed above: (1) selection of input-output mappings using resonant biases, and (2) controlling context-dependent synchronization using distinct populations of interneurons with different strengths of feedback inhibition.

Anatomically, LPFC is eulaminate cortex with well-differentiated superficial and deep layers separated by a granular layer (Barbas, 2015) with deep layer 5 pyramidal cells sending apical dendrites into the superficial layers and projecting axons to subcortical structures governing action. LPFC contains multiple interneuron types with more CB+ INs in superficial layers (e.g., layer 2) and PV+ INs in middle/deep layers (including layer 3) (DeFelipe, 1997). It receives feedforward inputs from sensory cortices projecting to middle layers and feedback inputs from ACC projecting to superficial layers, targeting more CB+ INs than PV+ INs (Medalla and Barbas, 2009). Physiologically, PV+ and CB+ INs in PFC can exhibit fast spiking (FS) and low threshold spiking (LTS) behavior (Kawaguchi, 1993; Kawaguchi et al., 1998). Pyramidal cells can show selectivity for stimuli, responses, and rules (Buschman et al., 2012). Motivated by these anatomical and physiological considerations, and the rule-based task of Buschman et al. (2012), we constructed a laminar model of LPFC capable of selecting rule-dependent input-output mappings using resonant biases.

The task involved visual presentation of a rule cue followed by a stimulus and a learned response. Depending on the rule (color (c) or orientation (o)), a given stimulus "S" (e.g., horizontal blue bar) can indicate to saccade left (L) or right (R). We simulated two trials with an incongruent stimulus that maps onto different responses depending on which stimulus dimension (color or orientation) is relevant according to the active rule. The model includes stimulus-selective populations ($_oS_L$ and $_cS_R$) of PCs in superficial layers and response-selective populations (L and R) of PCs in deep layers (Fig. 2.18). Interlaminar feedforward projections define parallel channels representing stimulus-

response mappings. $_oS_L$ and $_cS_R$ represent populations selective for different dimensions of the same stimulus and which map onto opposing responses, L and R, respectively. Independent of the rule, both populations will become active and tend to drive opposing responses. Given rule "o", $_oS_L$ should activate L more than $_cS_R$ activates R (i.e., select input-output mapping S→L). Given rule "c", the opposite should occur (i.e., S→R should be selected).

The oscillatory state of the superficial PC encoding populations ($_oS_L$ and $_cS_R$) is controlled by PV+ FS and CB+ LTS interneurons providing weak and strong feedback inhibition, respectively. When LTS cells pace the PC population, activity is more synchronous (due to stronger inhibition) and rhythmic at a beta frequency (due to the time constant of LTS inhibition). In contrast, when FS cells pace the PC population, spiking is less synchronous, and the population oscillates at a faster frequency (due to the shorter time constant of FS inhibition). Given beta resonance in the output layer, PC populations paced by LTS cells drive their targets more effectively. Critically, we assumed that context signals bias rule-specific mappings by increasing the excitability of rule-selective LTS cells. PC populations are paced by LTS cells only when the LTS cells are more excitable, otherwise PCs are paced by FS cells. The active rule in this model is then determined by which LTS cells receive the context signal. The input-output mappings enhanced via resonant bias are those with inputs paced by the in-context LTS cells.
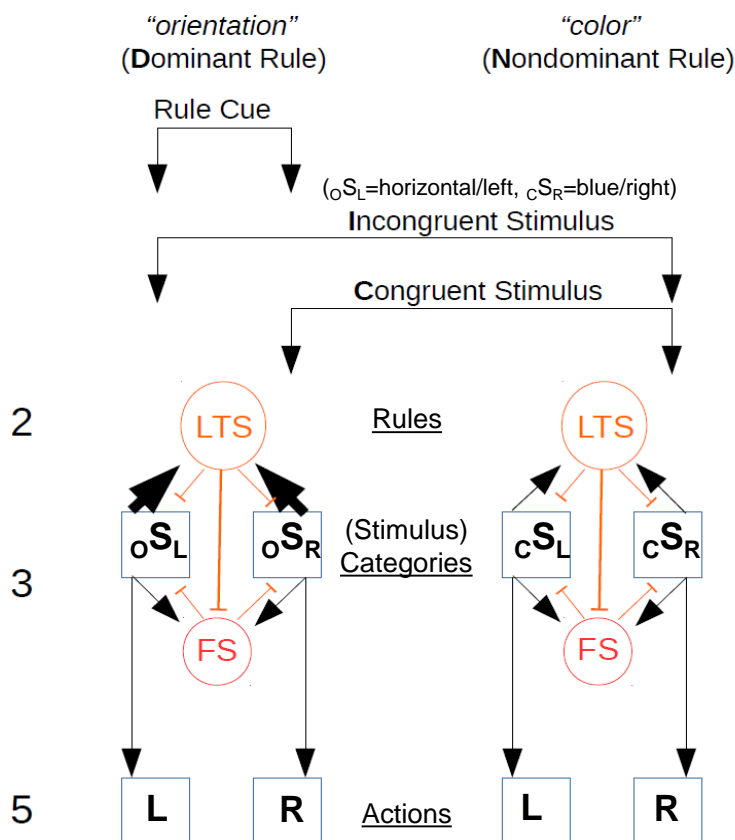
Fig. 2.18. Diagram of laminar LPFC model that performs a rule-based task.
In the rule-based task, an oriented, colored bar (stimulus S) triggers a learned response (saccade left L or right R) based on which stimulus dimension is relevant for the active rule. In the color rule (c), a red bar ($_cS_L$) triggers L, and a blue bar ($_cS_R$) triggers R. In the orientation rule (o), a horizontal bar ($_oS_L$) triggers L. An incongruent stimulus (e.g., horizontal, blue bar) has dimensions that map to opposing responses, and the correct response depends on the rule. The laminar model of LPFC contains stimulus-selective superficial PC populations and response-selective deep layer PC populations. The interlaminar structure has four parallel pathways that represent learned input-output mappings (e.g., $_cS_L{\rightarrow}L$, $_cS_R{\rightarrow}R$, $_oS_L{\rightarrow}L$). The incongruent stimulus activates $_oS_L$ and $_cS_R$, which drive opposing responses L and R, respectively. Layer 2 LTS and layer 3 FS interneuron populations provide strong and weak feedback inhibition, respectively. LTS cells are rule-selective and induce synchronous beta oscillations in specific PC inputs, enabling resonance to amplify their target responses through all pathways paced by LTS inhibition. When o-selective LTS cells pace $_oS_L$ activity, the resulting resonant bias amplifies L activity over R. In this way, rule-dependent LTS inhibition can mediate the selection of rule-based input-output mappings using resonant biases. See Appendix B for model details.
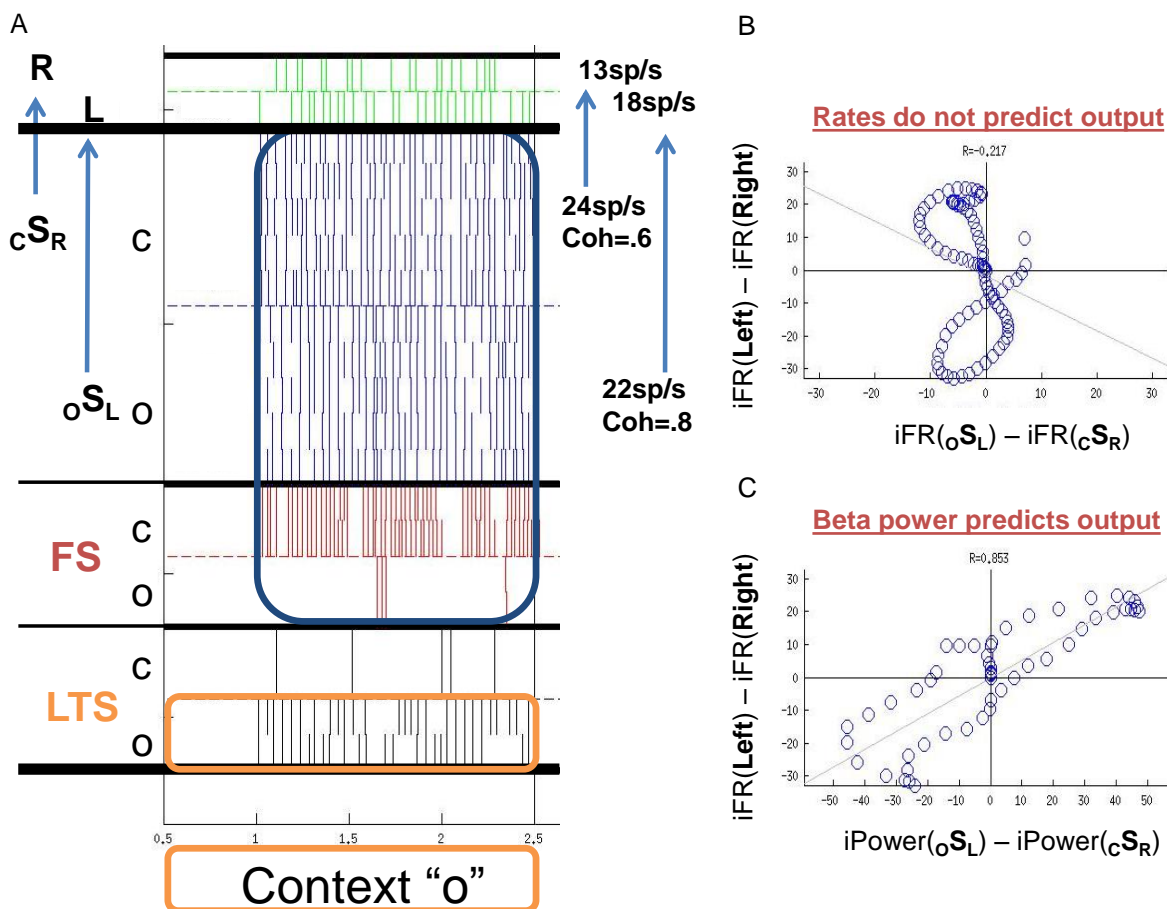
Fig. 2.19. Two trials with incongruent stimuli and different contexts.
(**A**) The first of two trials of a rule-based task with a subthreshold context cue driving o-selective LTS cells (orange box) and, .5s later, a suprathreshold stimulus driving superficial PC populations ($_oS_L$ and $_cS_R$) and FS cells (blue box). LTS cells require both cue and PC→LTS excitation to become active; their activity then suppresses FS cells. This results in $_oS_L$ paced by LTS and $_cS_R$ paced by FS. Stronger LTS→PC inhibition produces lower rates and higher coherence in $_oS_L$ compared to $_cS_R$ paced by weaker FS→PC inhibition. The time constant of LTS inhibition yields a beta-frequency rhythm in $_oS_L$ that is resonant for the deep output layer. The resonant bias, then, enables the more coherent (.8>.6) encoding population $_oS_L$ to drive greater L output despite having a lower mean firing rate (22sp/s<24sp/s) than the opposing pathway. When the rule switches, and c-selective LTS cells receive cue-related subthreshold drive, the dominant input-output mapping switches from $_oS_L$→L to $_cS_R$→R (not shown). (**B-C**) Differential output across two trials is predicted by input beta power, not input activity levels. (B) Differences in the instantaneous firing rate (iFR) outputs between the pathways (Left-Right) is not correlated with differences in the iFRs of the input encoding populations ($_oS_L$-$_cS_R$). (C) Differences in iFR between outputs is correlated with differences in the instantaneous levels of beta power (iPower) between the inputs. Beta power is more predictive because beta-frequency resonance overcomes the effects of small input rate differences.

In the first simulated trial (Fig. 2.19A), the "o" cue at .5s provided a subthreshold drive to "o" selective LTS cells. The stimulus arrived at 1s and provided suprathreshold drives to both stimulus-coding PC populations. The in-context PC population, $_oS_L$, was paced by the more excited LTS cells and, due to their strong feedback inhibition, were made more coherent (coh=.8) and exhibited a lower mean firing rates (22 sp/s). In contrast, the out-of-context PC population, $_cS_R$, was paced by FS cells providing weak feedback inhibition and, consequently, had higher mean firing rates (24 sp/s) but lower spike coherence (coh=.6). The resonant bias provided by the more synchronous $_oS_L$ population enabled it to activate its target (L) more than the higher rate $_cS_R$ population activated R. On the second trial (not shown), the rule cue provided a subthreshold drive to "c"-selective LTS cells, resulting in a resonant advantage for $_cS_R$ and more R output.

We analyzed the result in terms of instantaneous firing rates and the instantaneous beta power (calculated from the short-time Fourier transform averaged over 20-30Hz) of each stimulus-coding and response population. Plotting the difference in outputs (Fig. 2.19B-C, Left-Right) versus the difference in input rates (Fig. 2.19B) and the difference in input beta power (Fig. 2.19C) showed that which input-output mapping was selected was predicted by differences in input beta power, not differences in input rate. This demonstrates that context-specific rhythmicity, mediated by distinct populations of interneurons, can enable resonant biases to overcome differences in activity. It also provides an anatomical and physiological hypothesis for how the rule-related beta rhythmicity observed in primate DLPFC could confer a rule-related advantage biasing action selection.

The output bias demonstrated here is produced exclusively by resonance without competition. The earlier work in this chapter showed that the advantage provided by input rhythms can be increased beyond the effects of resonance alone when there is also lateral inhibition between outputs (Figs. 2.8-9) and output-specific recurrent excitation (Fig. 2.12). Thus, the anatomical details of LPFC layer 5 and effects of learning not captured by the model of Fig. 2.18 only increase the ability of input rhythms to mediate rule switching.

Our models do not utilize attractor states and, consequently, are not directly applicable to activation-based mechanisms for working memory (Durstewitz et al., 2000). However, work on achieving stable persistent activity in oscillatory populations of biophysically-detailed spiking neurons (Tegner et al., 2002) suggests the principles demonstrated here could operate equally well in the context of working memory attractor networks. Thus, resonant biases and synchronization mediated by distinct interneuron populations may support rule-based selection of read-out from working memory attractor networks..

CHAPTER 3

ANTERIOR CINGULATE HETEROGENEITY FOR COMBINATORIAL PROCESSING[3]

The anterior cingulate cortex (ACC) is vital for a range of brain functions requiring cognitive control and has highly divergent inputs and outputs, thus manifesting as a hub in connectomic analyses. Studies show diverse functional interactions within ACC are associated with network oscillations in the beta (20-30 Hz) and gamma (30-80 Hz) frequency range. Chapter 2 showed that oscillations permit dynamic routing of information within cortex, a function that depends on resonance and band-pass filter-like behavior to selectively respond to specific inputs. However, a putative hub region like ACC needs to be able to combine inputs from multiple sources rather than select a single input at the expense of others. Such a mechanism could serve process monitoring and the regulation of cognitive control, perhaps by driving thresholded outputs triggering switch mechanisms, mediated by superficial CB+ interneurons, that update the dynamical state of encoding populations in LPFC.

To address this potential functional dichotomy we modeled local ACC network dynamics in the rat *in vitro*. Modal peak oscillation frequencies in the beta- and gamma-frequency band corresponded to $GABA_A$ergic synaptic kinetics as seen in other regions;

---

[3] This chapter is an extension of the following reference: Natalie Adams*, Jason Sherfey*, Nancy Kopell, Miles Whittington, and Fiona LeBeau. *Heterogeneity in Neuronal Intrinsic Properties: A Possible Mechanism for Hub-Like Properties of the Rat Anterior Cingulate Cortex During Network Activity*. eNeuro 2017. * N.A. and J.S. contributed equally to the referenced manuscript. J.S. was trained in the experimental techniques, but N.A. obtained the data that was used in this work. J.S. analyzed the experimental data and performed all modeling and simulation.

however, the intrinsic properties of ACC principal neurons were highly diverse. Computational modeling predicted that this neuronal response diversity broadened the bandwidth for filtering rhythmic inputs and supported combination – rather than selection - of different frequencies within the canonical gamma and beta EEG bands. These findings suggest that oscillating neuronal populations can support either response selection (routing), or combination, depending on the interplay between the kinetics of synaptic inhibition and the degree of heterogeneity of principal cell intrinsic conductances.

3.1 Introduction

Anterior cingulate cortex (ACC) is a functionally distinct area of the prefrontal cortex (PFC) that in rats, primates and humans is associated with a broad range of functions including remote spatial memory (Teixeira et al., 2006; Wartman et al., 2014), attention and executive function (Kesner and Churchwell, 2011; Newman et al., 2014) adaptive control (Narayanan et al., 2013), error detection (Ito et al., 2003; Hyman et al., 2013), and reward-based decision making (Walton et al., 2003; Hillman and Bilkey, 2010). Such diversity of function, collectively referred to as 'cognitive control' (Shenhav et al., 2013) supports the idea that ACC may act as a general action-outcome-predictor (Hyman et al., 2013) and cognitive resource allocator performing a cost/benefit analysis on diverse signals (Botvinick 2016).

A wide range of inputs to ACC suggests that, from a connectomic point of view, this region can potentially monitor all modalities of primary sensory input, affective state,

motor state and associational processing (Hoover and Vertes, 2007; Park and Friston, 2013; Vogt and Paxinos, 2014). Equally diverse outputs from ACC (Gabbott et al., 2005) would allow this area to function as a higher-order hub region, vital for multimodal integration (Bassett et al., 2008).

A dynamic view of brain connectivity reveals a rich variation in the interplay between one brain region and others that change over timescales of less than tens of milliseconds (Kopell et al., 2014). Functional connectivity, with quantifiable behavioral consequences, involves specific phase relationships between activity in different areas organized over a spectral range including beta- (20-30 Hz) and gamma- (30-80 Hz) frequency EEG bands (Bastos et al., 2015). Within this frequency range, local neuronal networks can effectively 'select' which inputs to respond to on the basis of the relative peak frequency of concurrent inputs – with more resonant frequencies taking precedence (Chapter 2; see also Cannon et al., 2013). This selection of inputs can lead to 'routing' of information based on the relative strength of the oscillations present in the inputs (Chapter 2; see also Kopell et al., 2010; Akam and Kullmann, 2010, 2014).

Network oscillations in the beta- and gamma frequency range in PFC subregions, including ACC, are associated with many cognitive functions (Buschman et al., 2012; Brincat and Miller, 2015). This activity depends upon local network interactions between excitatory principal cells and fast-spiking, parvalbumin-containing (PV) interneurons (e.g. Fisahn et al., 1998; Whittington et al., 2011). Computational studies have predicted that the input selection and routing behaviors of gamma and beta rhythms are, at least in part, manifest through the establishment of 'band-pass filter' and rhythm-mediated

competitive behavior of local networks afforded by the kinetics of the synaptic inhibition provided by these PV neurons (Chapter 2; see also Akam and Kullmann, 2010; Cannon et al., 2013). In contrast, it can be argued that the function of hub-like regions like ACC should depend more on a combinatorial processing of inputs, with selection and routing processes more appropriate for regions critical for contextual disambiguation (Phillips et al., 2010).

Using *in vitro* recordings in rat ACC, we investigated the network properties of beta- and gamma frequency oscillations generated locally and the diversity of intrinsic cellular properties of ACC principal cells. The experimental data in this chapter was collected by Natalie Adams in the LeBeau laboratory at Newcastle University. The data demonstrated that the generation of both beta- and gamma frequency oscillations was critically dependent on the kinetics of fast synaptic inhibition, as widely reported in other brain regions (Whittington et al., 2011). Here we show that both passive and active intrinsic principal cell properties exhibited a great deal of heterogeneity. Computational studies, constrained by this biological data, showed that in response to rhythmic (sinusoidal) input the kinetics of slow (13 ms) and fast (5 ms) synaptic inhibition decay times determined the 'center frequency' of the band-pass filtering properties of the ACC network to within either the beta- or gamma-frequency range, respectively. However, modeling the observed heterogeneity in the intrinsic properties of ACC neurons broadened the filter bandwidth at both beta- and gamma frequencies. The main consequence of the broader filter bandwidths was to bias the local network behavior

away from input-selection, and towards a more combinatorial behavior, consistent with the proposed hub-like function of ACC.

3.2 Methods

3.2.1 *Slice Preparation and solutions*

Coronal slices 450 µm thick containing the caudal regions of ACC (Cg1 and Cg2) were prepared from 2-3 month old male Lister Hooded rats. Rats were anesthetized with inhaled isoflurane, followed by an intramuscular injection of ketamine (100 mg/kg; Fort Dodge Animal Health Ltd., Southampton, UK) and xylazine (10 mg/kg; Animalcare Ltd., York, UK). When all response to noxious stimuli, such as pedal withdrawal reflex, had terminated, the animals were intracardially perfused with ~50 ml of modified artificial cerebrospinal fluid (ACSF) that was composed of, in mM, 252 sucrose, 3.0 KCl, 1.25 NaH_2PO_4, 24 $NaHCO_3$, 2.0 $MgSO_4$, 2.0 $CaCl_2$ and 10 glucose. All procedures were in accordance with the UK Animals (Scientific Procedures) Act 1986 and the European Union Directive 2010/63/EU.

Following brain removal, 450 µm thick coronal PFC slices were cut using a Leica VT1000S vibratome. Slices were then trimmed and transferred to a holding chamber at room temperature for ~1 hour, which allowed washout of all anaesthetic agents, before being transferred to a recording chamber where they were maintained at ~29-31°C at the interface between normal ACSF (where sucrose was replaced with 126 mM NaCl and $MgSO_4$ and $CaCl_2$ were reduced to 1.2 and 1.76 mM respectively) and humidified 95%

O_2/5% CO_2. Drugs used were as follows: kainic acid (800 nM) (Sigma-Aldrich); the AMPA/kainate receptor antagonist 2,3-Dioxo-6-nitro-1,2,3,4-tetrahydrobenzo[f]quinoxaline-7-sulfonamide, (NBQX; 10 µM); the NMDA receptor antagonist D-(-)-2-Amino-5-phosphonopentanoic acid (D-AP5; 50 µM); the $GABA_B$ receptor antagonist 3-aminopropyl-diethoxy-methyl-phosphinic acid CGP 35348 (5 µM).

3.2.2   Recording Techniques

Extracellular recordings were performed with ACSF-filled glass microelectrodes (resistance <5 MΩ). Only one extracellular electrode was positioned in each slice, which was moved across the laminae until a clearly detectable oscillation was recorded. Intracellular recordings used potassium acetate (2 M) filled glass microelectrodes (resistance 80 MΩ - 150 MΩ). To assess the intrinsic membrane properties ACC cells were recorded with antagonists of glutamatergic transmission including NBQX (10 µM), D-AP5 (50 µM) and CGP 35348 (5 µM) in the ACSF. Slices were maintained in an interface recording chamber at 29-30°C. Data were recorded via an Axoclamp amplifier (Molecular Devices), using an InstruTECH ITC-16 (HEKA Electronic, Digitimer, Welwyn Garden City, Herts, UK) after live mains noise was removed using a Humbug (Quest Scientific, Digitimer, Welwyn Garden City, Herts, UK) and pre-amplification and bandpass filtering between 1.5 – 300 Hz (Neurolog, Digitimer, Welwyn Garden City, Herts, UK). Data were sampled at 5 kHz and band-pass filtered (1.5 Hz – 100 Hz).

3.2.3   Data Analysis

All time-series analyses were performed in Matlab (MathWorks Inc., Natick, MA, USA). Power spectra for all LFP and intracellular recordings were created using Welch's estimate on traces between 20 seconds and 1 minute in length, using a window length of 5 seconds and a 50% window overlap. During post-processing the LFP data were only processed up to a frequency of 80 Hz.

3.2.4   Post-synaptic potentials

Inhibitory post-synaptic potentials (IPSPs) were recorded with cells held at a membrane potential of -30 mV (Fig. 3.1). IPSPs were analyzed using a custom made Matlab script and were only included if the amplitude exceeded 0.5 mV. IPSP amplitude was calculated as the voltage difference between the trough of the IPSP and the preceding peak (start of the IPSP). Decay times of IPSPs were taken at 63% of the peak voltage deflection. Spike triggered averaging was performed by taking the mean of all spiking events above a threshold of -40 mV with the spike peak forming the center of the average and including 50 ms before and 200 ms following the peak.

3.2.5   ACC cell intrinsic properties

Numerical values for intrinsic parameters (IPs) were collated for each cell (Fig. 3.2). The chosen IPs were as follows: IP1 Action potential (AP) amplitude (mV); IP2 I_h (cAMP-dependent hyperpolarization-activated current) estimate (the amplitude of the sag potential from the steady state of -200 nA step injection and the subsequent return to rest) (mV); IP3 after-hyperpolarization (AHP) amplitude (mV); IP4 AHP magnitude (voltage

integrated over 200 ms post AP; mV); IP5 AHP time to maximal deflection (ms); IP6 Spike width at half-height (ms); IP7 Spontaneous spike rate at threshold (Hz); IP8 Resting membrane potential (rmp; mV); IP9 Initial spike frequency (time between first and second spikes) on step depolarization (Hz); IP10 Ratio of 3rd to 2nd inter-stimulus interval on step depolarization-induced spike train (used as a measure of spike frequency adaptation; unitless). After within-parameter normalization, the normalized cross-correlation coefficients between pairs of parameters were found. IPs that were correlated (or anti-correlated) above an absolute value of +/- 0.33 were considered significantly correlated and were discarded. The variance explained in the remaining IP dataset (IP3, IP5, IP6, IP7, IP8, IP9, IP10) was calculated for each property.

3.2.6   Cell Clustering

Clustering was performed using k-means and hierarchical methods (Fig. 3.3). One-way ANOVA analysis was used to compare parameter distributions across the clusters. After within-parameter normalization, the normalized cross-correlation coefficients between pairs of parameters were found, producing a correlation matrix of all pairs. Variables that were correlated (or anti-correlated) above an absolute value of +/- 0.33 were classed as significantly correlated variables and were discarded. MANOVA analyses of the remaining parameters were performed on all pairs of clusters to determine if cells could be clustered according to individual or combined parameters. Hierarchical clustering utilized Ward's minimum variance criterion. The effectiveness of clustering was tested for 2 – 10 clusters using the Davies-Bouldin Index, which measures the ratio of intra-cluster scatter to inter-cluster separation, and the Dunn's Index, which similarly

assesses intra-cluster distance versus inter-cluster distance. Maximization of the Davies-Bouldin index and minimization of the Dunn's Index provide internal measures of the effectiveness of the clustering (Davies and Bouldin, 1975; Maulik and Bandyopadhyay, 2002). Data were shuffled by re-ordering the values for each intrinsic property via a random permutation in Matlab.

3.2.7   Statistical Analysis

Statistical analyses were performed in Sigmaplot 11.0 (Systat Software Inc., San Jose, California, USA) and data were presented as median 25-75% interquartile ranges (IQR) and significance chosen was P <0.05.

Computational Modeling

3.2.8   Pyramidal cell model

We developed a single-compartment pyramidal cell model capable of producing the range of intrinsic membrane properties observed in ACC (Fig. 3.4). The conductance-based model had a membrane potential V (mV) governed by:

$$C_m \frac{dV}{dt} = I_{inj}(t) - \sum I_{int} + \eta$$

where t is time (ms), $C_m = 1\mu F/cm^2$ is the membrane capacitance, $\eta = .01\varepsilon$ is Gaussian noise with $\varepsilon \sim N(0,1)$ and amplitude tuned to match baseline fluctuations in membrane potential, $I_{inj}(t)$ is an injected current ($\mu A/cm^2$) simulating an *in vitro* experimental
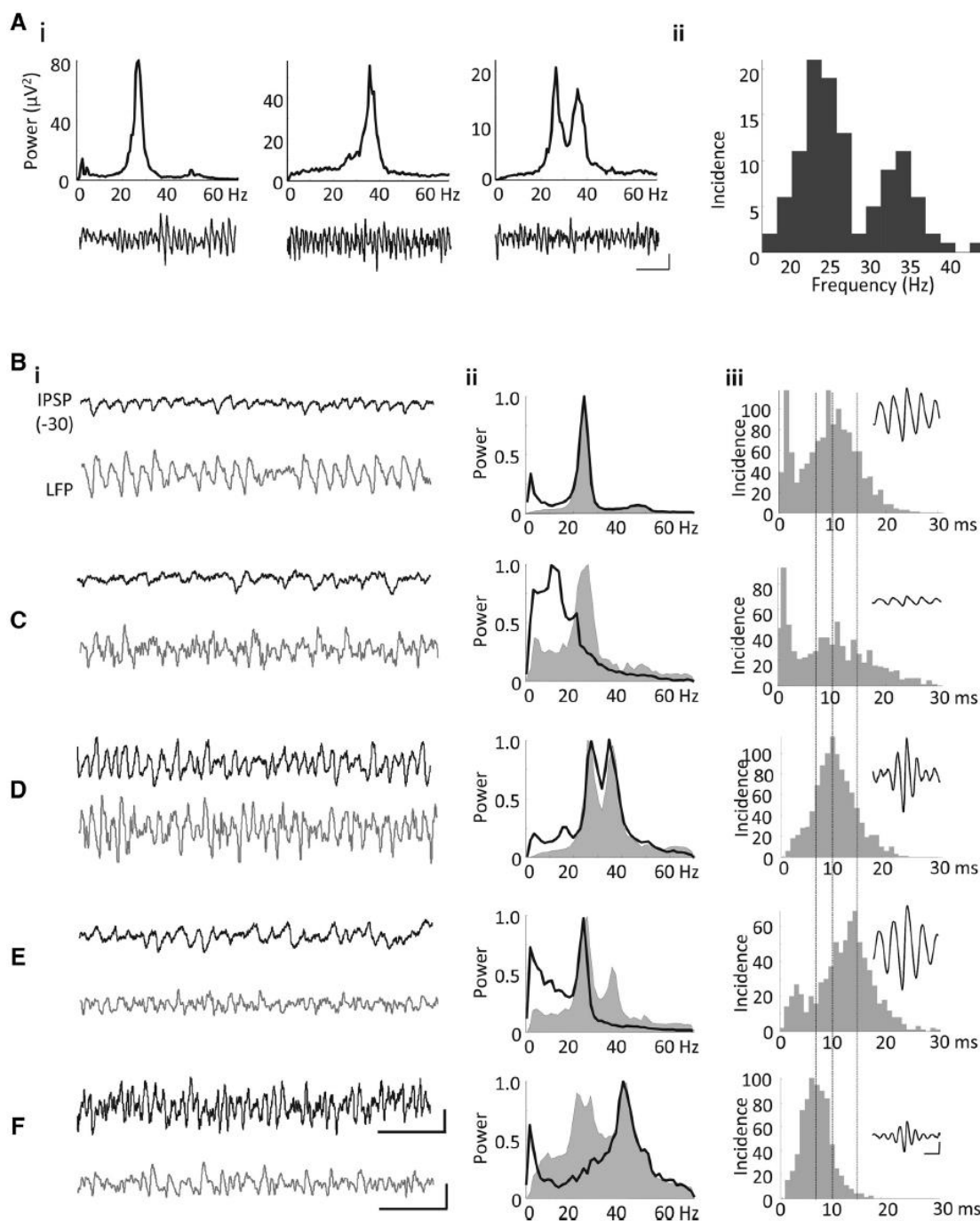
Fig. 3.1. IPSPs suggest dual inhibitory inputs in ACC cells during gamma/beta network oscillations.
Ai) Example power spectra and traces of KA-evoked oscillations showing representative local field potential oscillations from three different slices consisting of purely beta rhythms (left), purely gamma rhythms (middle) and a dual frequency oscillation (right); scale bar 50 µV, 200 ms. Aii) Incidence plot for the modal peak

frequencies in spectra from 109 ACC slices showing a clear bimodal average spectrum. Bi) Example IPSP traces (scale bar 5 mV, 200 ms) and simultaneously recorded LFP (scale bar 50 µV, 200 ms) with corresponding normalised power spectra (ii) showing the LFP power spectrum (shaded) and overlaid IPSP power spectrum (black line). Biii) Distribution of IPSP decay times. The inset shows IPSP-triggered averages of the LFP. B) Field oscillation and IPSP at beta frequency. C) Field oscillations at beta frequency but IPSPs at ~12 Hz. D) Mixed gamma/beta frequency field oscillation and IPSPs. E) Mixed gamma/beta field oscillations but IPSPs only at beta frequency. F) Mixed gamma/beta field oscillations but IPSPs only at gamma frequency.

protocol, and I_{int} denotes intrinsic membrane currents ($\mu A/cm^2$) produced by ionic conductances with Hodgkin-Huxley-like channel kinetics from published cell models: I_{KDR}, I_{NaF}, I_{KS}, and I_{NaP} from (Durstewitz and Seamans, 2002) for spike generation and adaptation; I_{CaN}, I_{CaT}, I_{KCa}, and I_H from (Papoutsi et al., 2013) for calcium-dependent adaptation, slow afterhyperpolarization, and hyperpolarization-induced voltage sag; and I_{AHP} from (Yamada et al., 1998) (see legend of Fig. 3.4 for more details). Ionic currents from (Durstewitz and Seamans, 2002) and (Papoutsi et al., 2013) were chosen because their kinetics were constrained by experimental data from rat mPFC. Each active current was modeled as $I_{int} = g_{int}m^p h^q (V\text{-}E_{int})$ where maximal conductance g_{int} (mS/cm^2), reversal potential E_{int} (mV), p, q, and the kinetics of activation gate m and inactivation gate h were as published unless otherwise specified. All cells had a passive leak current $I_L = g_L(V\text{-}E_L)$ with conductance $g_{L}=.04$ mS/cm^2 and reversal potential E_L (mV).
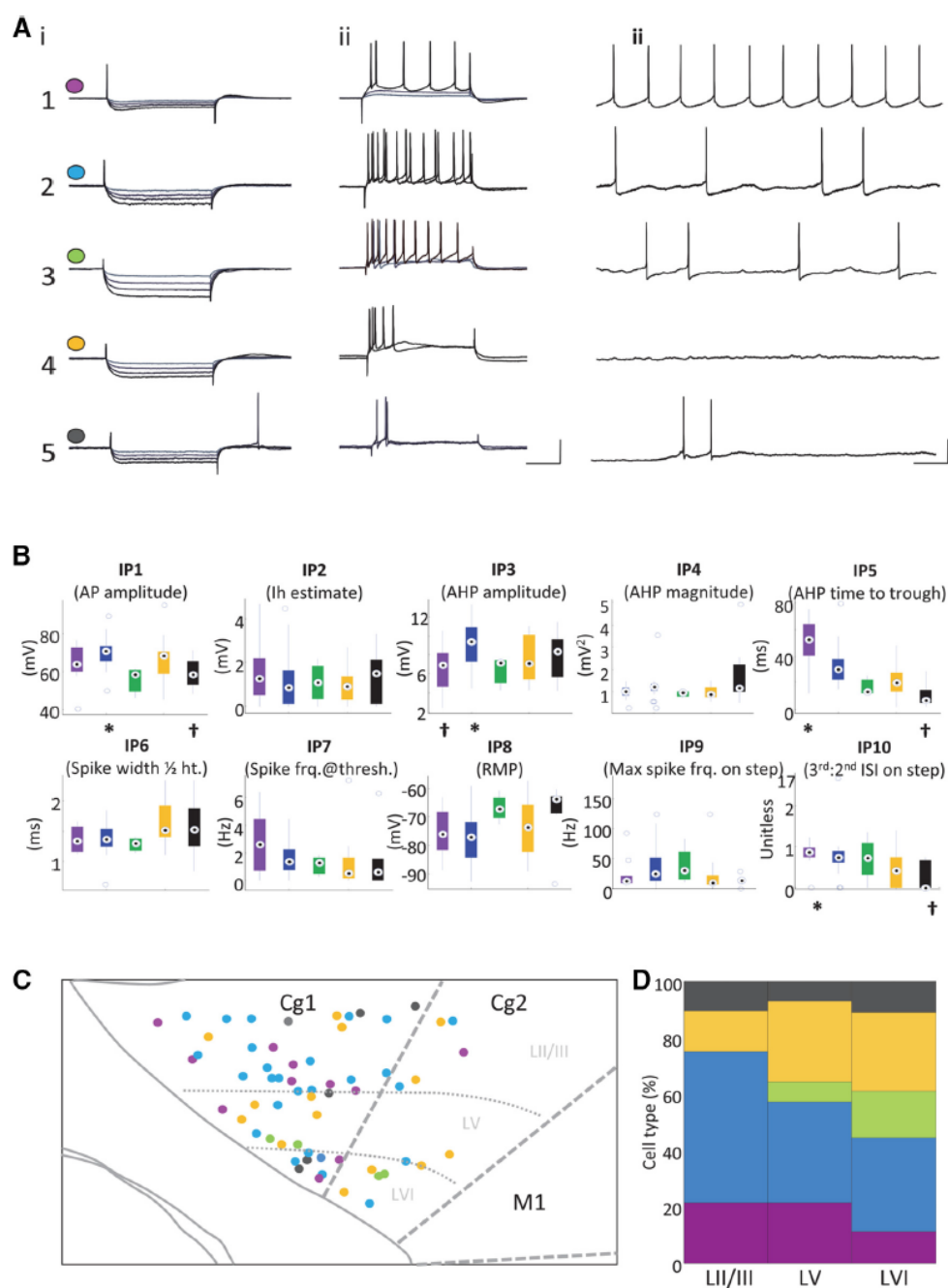
Fig. 3.2. Manual classification and laminar distribution of cells in ACC.
A) Each row shows the electrophysiological response properties of one example cell from each Group 1 - 5 to i) 400 ms hyperpolarizing steps at 0.1 – 0.4 nA; ii) 400 ms depolarizing steps at 0.3 – 0.4 nA; (grey to black = smaller to larger current step; scale bar 20 mV, 100 ms). iii) tonic activity at spike threshold (scale bar 20 mV, 200 ms).

B) Values (medians and interquartile ranges) for 10 IPs plotted for each manually selected Group 1 - 5 (colours as in A). † significantly different from * (One-way ANOVA P <0.05). Central circle = median values; blue circles = outliers. C) A schematic diagram of ACC (Cg1 and Cg2) with dots showing the location of cells found with different response properties. The colour of each dot corresponds to cells from Groups 1-5 recorded at each location. D) Plot shows the laminar distribution profile as a percentage of total cells in Groups 1-5.

The *in vitro* cell characterization experiment was simulated by a current injection, $I_{inj}(t)$, delivering a series of hyperpolarizing and depolarizing pulses followed by a ramp to spike threshold then constant depolarization (compare Fig. 3.4A). Model IPs were calculated from the simulated data using the same analysis applied to the experimental recordings. A set of cell models capturing the diversity observed in ACC was obtained by manually varying biophysical parameters and comparing model IPs to the aggregate (all cells, all layers) experimental distributions (Fig. 3.4C). Specifically, E_L and maximal values for 8 active conductances (g_{KDR}, g_{NaF}, g_{KS}, g_{CaN}, g_{CaT}, g_{KCa}, g_H, g_{AHP}) were varied across simulations to find a set of models with IPs spanning the ACC distributions for the 5 most discriminative IPs from the experimental IP data analysis (IP5, IP6, IP7, IP8, IP9; accounting for 85% of the total variance in ACC IPs; see Fig. 3.4C). Parameter space was explored in two steps. First, each maximal conductance was logarithmically varied 1E-6 to 1E2 to determine the scales over which realistic IPs could be observed. Next, hypercube subspaces were explored around the identified scales for maximal conductance and a E_L range spanning the recorded RMP values. Only parameter sets producing IPs within the experimental ranges were considered viable models of the

pyramidal cells recorded *in vitro* in the presence of synaptic blockers. This procedure resulted in 2,810 viable cell models out of >100,000 simulated models.
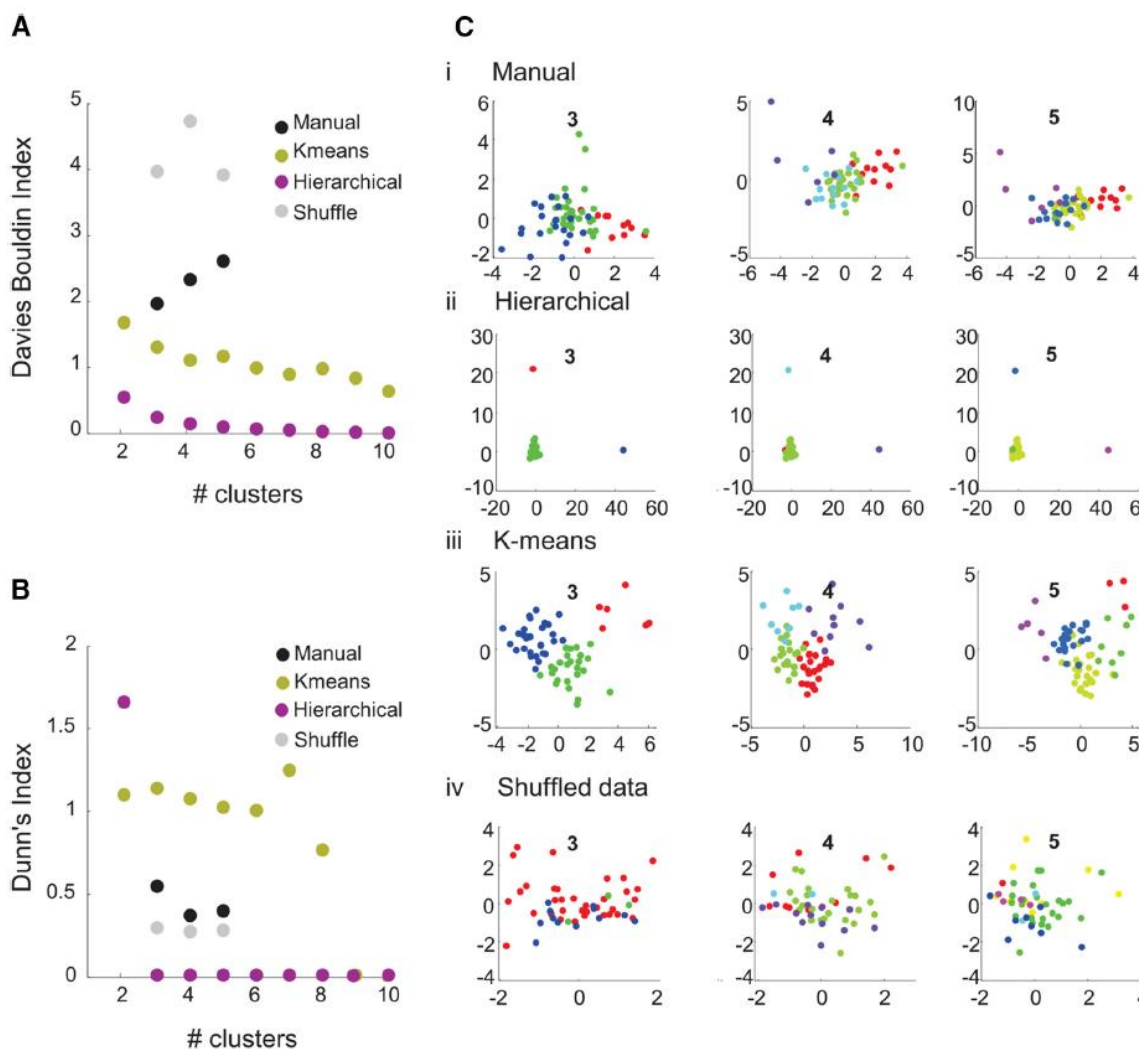
Fig. 3.3. Objective clustering analysis does not identify distinct clusters.
Validity indices (A) Davies-Bouldin (B) Dunn's index for the 3 clustering methods attempted; manual (black circles), k-means (olive circles), hierarchical (purple circles) and shuffled data (grey circles) for a range of cluster numbers (2-10 clusters). C) 2D canonical variable plots (unitless) from the multivariate analysis for the (i) manual, (ii) hierarchical, (iii) k-means and (iv) shuffled clusters when assuming 3, 4 and 5 clusters. Each plot shows the cells of each cluster as an arbitrary colour.

All viable cell models had biophysical parameters yielding intrinsic electrophysiological properties within the ranges observed experimentally. Across the set of viable models, each biophysical parameter had a distribution of values (Fig. 3.4C) and tended to co-vary with other biophysical parameters to some degree. We defined a homogeneous assembly of cells as a population of equivalent cell models with biophysical parameters set to medians computed across the full set of viable models; all cells belonging to a given assembly received similar inputs (see details below). Independent realizations of heterogeneous assemblies were generated by drawing biophysical parameters from a multivariate normal distribution using the co-variance matrix, including all pairs of biophysical parameters, computed across the full set of 2,810 viable models.

3.2.9 *Biophysical network model*

We developed a computational representation of a generic ACC network including single-compartment excitatory (E) pyramidal cells and inhibitory (I) interneurons. E-cells were modeled as previously described with the addition of synaptic inputs and exclusion of the injected current:

$$C_m \frac{dV}{dt} = -I_{ex}(t,V) - \sum I_{int} - \sum I_{syn}$$

where $I_{ex}(t,V)$ is an excitatory current (μA/cm^2) reflecting inputs from external sources and I_{syn} denotes synaptic currents (μA/cm^2) driven by other E- and I-cells in the network. I-cells were modeled using the fast-spiking (FS) Wang-Buzsaki interneuron model

(Wang and Buzsaki, 1996). A more computationally demanding FS I-cell model based on PFC data (Durstewitz and Seamans, 2002) produced qualitatively similar results.

All networks consisted of 80 E-cells split into one or two assemblies coupled reciprocally to a shared pool of 20 I-cells (see model architecture in Figs. 3.5A,B and 3.6A). E-cells provided excitation to all I-cells, mediated by α-amino-3-hydroxy-5-methyl-4-isoxazolepropionic acid (AMPA) currents. I-cells in turn provided inhibitory inputs γ-aminobutyric acid (GABA$_A$) currents to all E-cells and I-cells. AMPA currents were modeled as:

$$I_{AMPA} = g_{AMPA}s(V\text{-}E_{AMPA})$$

where V is the postsynaptic membrane voltage, g_{AMPA} is the maximal synaptic conductance, s is a synaptic gating variable, and $E_{AMPA} = 0$ mV is the synaptic reversal potential. Synaptic gating was modeled by:

$$\frac{ds}{dt} = H(V_{pre})\frac{(1-s)}{\tau_r} - \frac{s}{\tau_d}$$

where V_{pre} is the presynaptic membrane voltage, $\tau_r = .4$ ms and $\tau_d = 2$ ms are time constants for neurotransmitter release and decay, respectively, and $H(V) = 1 + \tanh(V/10)$ is a sigmoidal approximation to the Heaviside step function. GABA$_A$ currents are modeled in the same way with $E_{GABA} = $ -75mV and variable $\tau_d = \tau_I$ (5 ms or 13 ms, reflecting inhibition from different interneuron classes). Maximum synaptic conductances for E-cells were (in mS/cm^2): GABA$_A$ (.1); for I-cells: AMPA (1), GABA$_A$ (1).
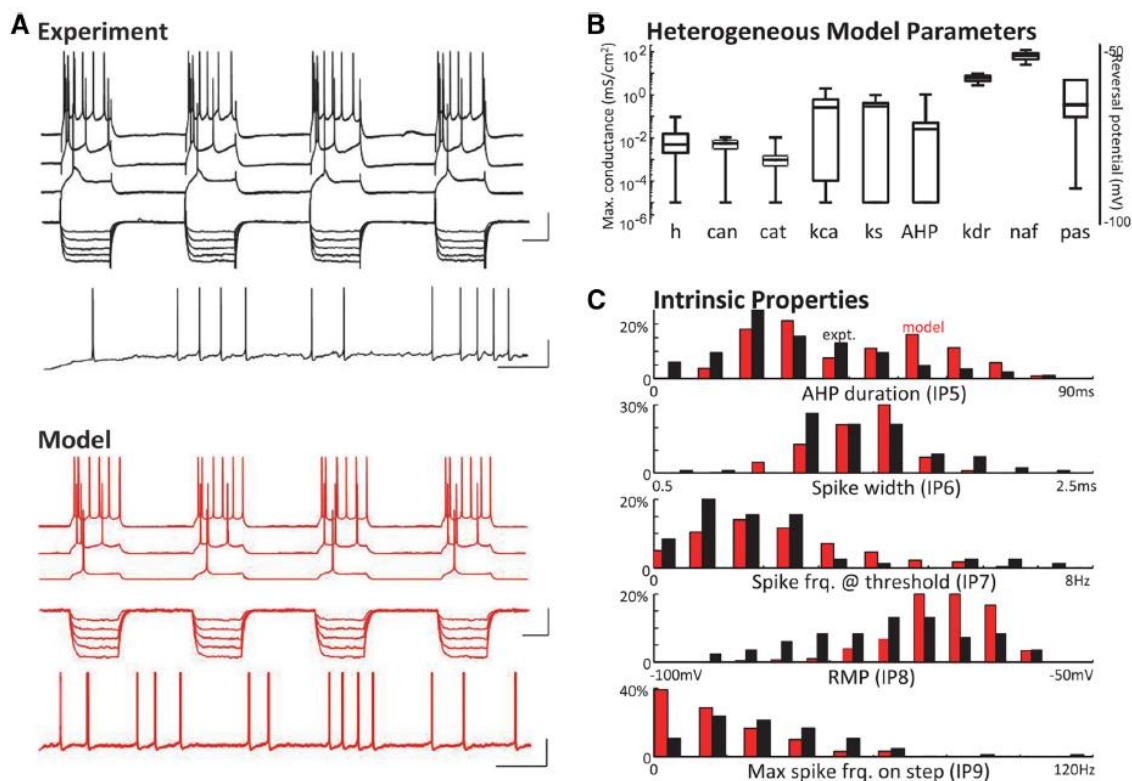
Fig. 3.4. Heterogeneous biophysical models reproduce the range of experimental intrinsic properties.
A) Example of experiment and model cell responses to depolarising current steps (top traces) and hyperpolarising current steps (middle traces) and firing rate at r.m.p. (bottom trace). Scale bars 20 mV/100 ms and 20mV/2sec. B) Shows ion channel conductance ranges (10^{-6} to 10^2) used in ACC cell model. Values are based on model fits to experimental IP ranges. (Ion channel key: h = HCN channel; can = high-threshold (N-type) calcium channel; cat = low-threshold (T-type) calcium channel; kca = calcium-dependent potassium channel; ks = slow (M-type) potassium channel; AHP = slow afterhyperpolarizing potassium channel; kdr = fast delayed rectifier potassium channel; naf = fast sodium channel; pas = passive leak channel). C) Model and experimental IP distributions for the 5 IPs (IP5-9) that explained most of the variance.

E/I networks with one E-cell assembly were simulated to probe the natural and

resonant frequencies of ACC networks with and without E-cell heterogeneity (Fig. 3.5).

In these simulations, the input was a gated channel with excitatory AMPA current

$I_{ex} = g_{ex}S_{ex}(V\text{-}E_{ex})$ where E_{ex} is the synaptic reversal potential and S_{ex} is a postsynaptic gating variable that integrates independent Poisson spike trains with time-varying rate function $\lambda(t)$. In different simulations, $\lambda(t) = r$ (background activity) was used to probe natural frequencies and $\lambda(t) = r(1 + \sin(2\pi f t))/2$ (rhythmic input) was used to probe resonant frequencies. Input spike trains represent background noise or rhythmic population activity originating from an arbitrary source network and are integrated in the synaptic gate S_{ex} with exponential AMPAergic decay. r was tuned during the former simulations to produce firing rates observed in the *in vitro* experiments with kainate-induced network oscillations. In the latter simulations, f was varied from 4 Hz to 60 Hz (2 Hz steps) across simulations. All single-assembly simulations were repeated for $\tau_I = 5$ ms and $\tau_I = 13$ ms based on experimentally observed IPSPs in the gamma- and beta-coherent cells, respectively. Parameters were set to $E_{ex} = 0$, $g_{ex} = .001$, $r = 4500$ Hz.

E/I networks with two identical E-cell assemblies, E1 and E2, were simulated to probe the effects of heterogeneity on synchrony (integration) and competition between assemblies receiving noise or rhythmic inputs at different frequencies, f_1 and f_2, respectively (Fig. 3.6). In these simulations, the excitatory input was a gated AMPAergic response to a Poisson spike train as before. However, assemblies E1 and E2 received inputs from distinct source networks. Source network frequencies (f_1, f_2) were varied over a grid ranging 7.5 Hz to 60 Hz (7.5 Hz steps) across simulations while the number

of spikes delivered to each assembly was fixed. $\tau_I = 5$ ms and $\tau_I = 13$ ms were both used for the results reported below.

The diversity of cell intrinsic properties observed in ACC pyramidal cells was incorporated into heterogeneous E-cell assemblies as previously detailed. For a given simulation with two assemblies, the same cell models were used for both assemblies to ensure that differences in their activities resulted from differences in their inputs and not differences in their cell properties.

All models were implemented in Matlab using the DynaSim toolbox (github.com/DynaSim) and are publicly available online at: github.com/jsherfey/ACd_model. Numerical integration was performed using a 4th order Runge-Kutta method with a fixed time step of .01ms. One- and two-assembly network simulations were run for 2000 ms and 5000 ms, respectively, and the first 500 ms was excluded from subsequent analysis. All network simulations were repeated 10 times.

3.2.10   Model analysis

Analysis of model networks with one assembly. The natural frequency of a network is the frequency of rhythmic population activity that emerges naturally given background activity. The natural frequency was identified as the frequency with peak power in Welch's spectrum of the mean E-cell voltage (simulated LFP) given an external input with constant g_{ex}. The resonant frequency of a network is the frequency of a rhythmic input for which the network exhibits maximal spiking. The resonant frequency

was identified as the input frequency producing the maximum number of spikes in the E-cell assembly given an external input with sinusoidal g_{ex}.

Analysis of model networks with two assemblies. Two E-cell assemblies coupled to a shared pool of I-cells may differ in their amount of spiking (i.e., they may compete) and/or exhibit synchronous spiking to varying degrees (i.e., they may or may not support integration). The degree of competition between two assemblies, E1 and E2, was quantified by:

$$\Delta = \frac{|N_1 - N_2|}{N_{max}}$$

where N_1 is the number of spikes in assembly E1, N_2 is the number of spikes in assembly E2, and N_{max} is the number of spikes in the more active assembly. Δ indicates how much more active a dominant assembly is compared to a less active assembly; it varies between 0 (equal activity levels) and 1 (total suppression of the nondominant assembly). The degree of spike synchrony between two assemblies was quantified using the percentage of 10 ms time bins for which spiking occurred in both assemblies. Competition and synchrony were compared between homogeneous and heterogeneous networks using a two-sample *t*-test and were considered significant if P <0.05.
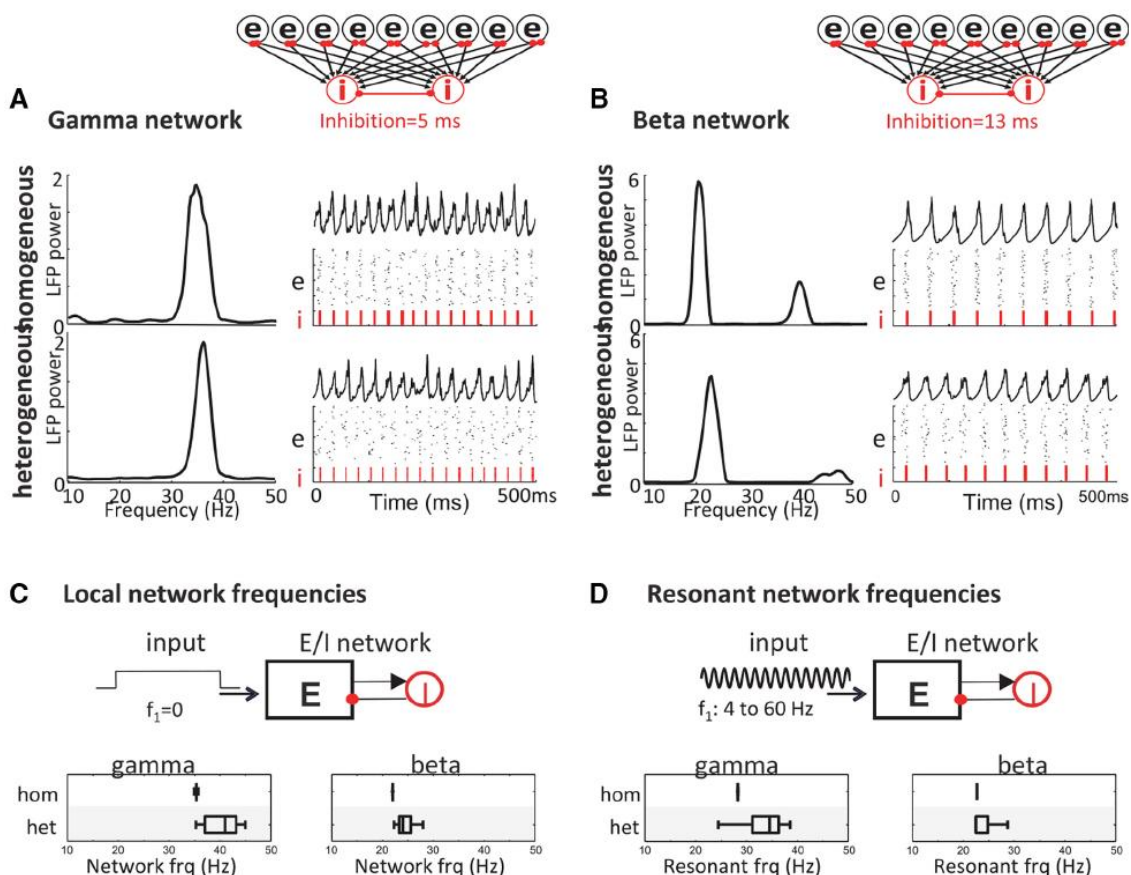
Fig. 3.5. Cell diversity broadens intrinsic (local) oscillations and network tuning in ACC model.
A-B) Network models were constructed by coupling the heterogeneous E-cell population to I-cells with time constants of inhibition based on the IPSP durations observed in cells rhythmic with the network beta or gamma rhythm in the LFP. The resulting E/I networks with fast (5 ms) and slow (13 ms) inhibition produced (A) gamma frequency and (B) beta frequency network oscillations whether the E-cell population had homogeneous or heterogeneous IPs. C) Effect of cell diversity on the intrinsic (local) frequency of network oscillations: Poisson noise input was applied to different 80-cell subsets of network E-cells on different realizations. Box plots show range of network frequencies for homogeneous and heterogeneous networks with different inhibition time constants at beta and gamma frequencies. (D) Effect of cell diversity on network tuning (resonant frequency): a sinusoidal input was applied to different subsets of E-cells on different realizations, independently for each input frequency 4 Hz to 60 Hz (in 2 Hz steps). Box plots show range of resonant frequencies of the homogeneous and heterogeneous networks.
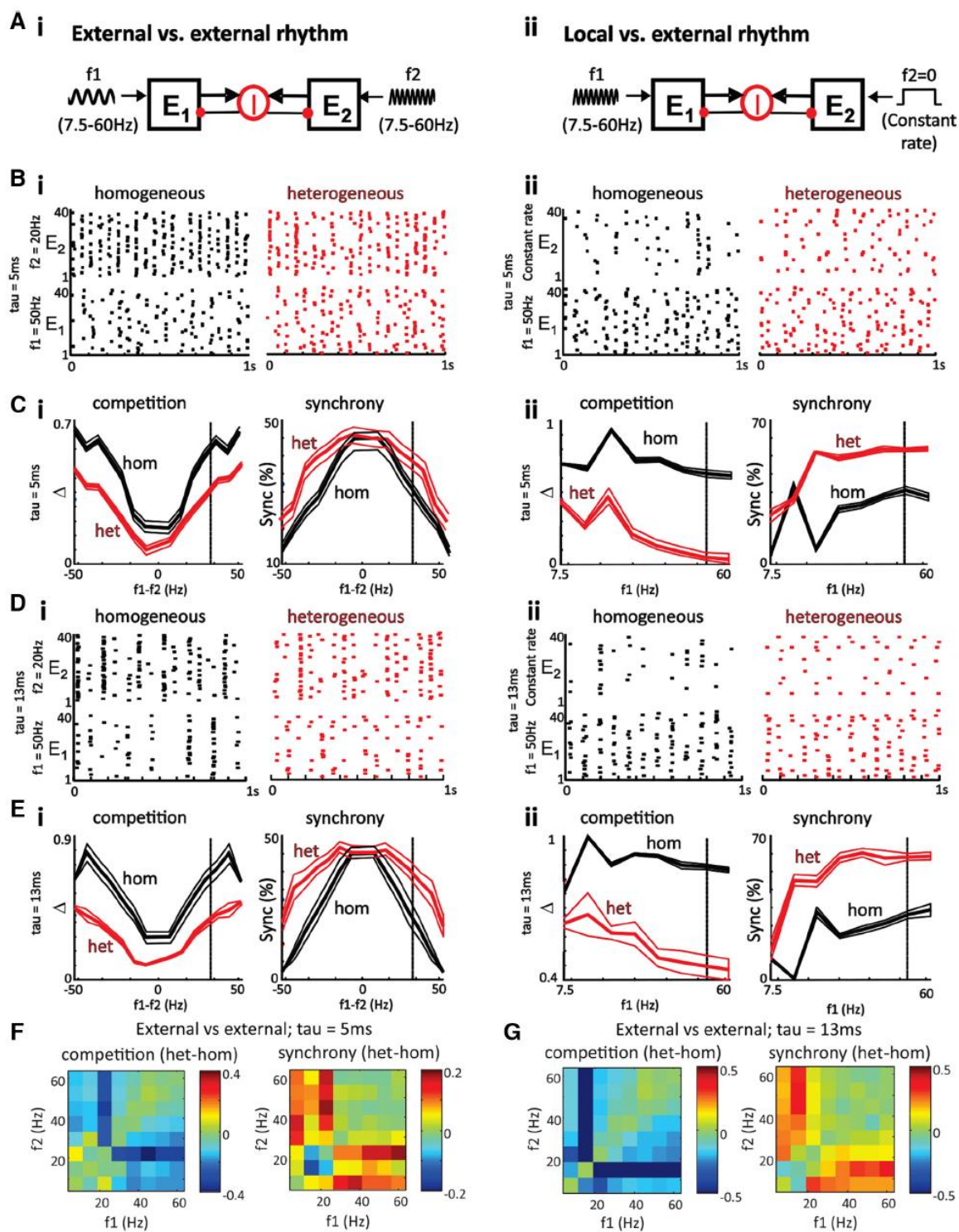
Fig. 3.6. Heterogeneity increases synchrony and decreases competition between cell assemblies.

Ai) Model schematic showing two excitatory assemblies, E1 and E2, receiving rhythmic AMPAergic inputs with equal spike counts and time-varying Poisson rates modulated at frequencies f_1 and f_2, respectively. The assemblies compete through a shared pool of inhibitory interneurons (I-cells) and $\tau_I = 5$ ms and $\tau_I = 13$ ms was used for these results. Bi) For homogeneous assemblies (left raster plots) driven by external rhythms, the assembly with a more resonant input (e.g., 20 Hz) suppresses spiking in the assembly driven by a less resonant input (e.g., 50 Hz). Heterogeneity of cell intrinsic properties decreases this competition (right raster plots) and increases synchrony between the two assemblies (i.e., the fraction of 10 ms bins with spiking in both E1 and E2). Ci) Heterogeneity decreases competition (Δ) across all pairs of input frequencies and increases synchrony for inputs separated by more than 30 Hz. Solid lines represent the f_1 - f_2 shown in the above raster plots. Di) and Ei) show similar raster plots, and plots of competition and synchrony for $\tau_I = 13$ ms. Again heterogeneity decreases competition across all pairs of input frequencies and increases synchrony for inputs separated by more than 30 Hz. Aii) Model schematic showing two assemblies, E1 and E2, receiving external rhythmic and background noise inputs, respectively, with the latter driving a local rhythm at the natural frequency of E2 (as in Fig. 5A). Bii) The less resonant input from (Bi) strongly suppresses an assembly driven by a non-rhythmic Poisson input with equal spike count and constant rate. Heterogeneity decreases competition and increases synchrony. Cii) Heterogeneity again decreases competition for all input frequencies and increases synchrony for frequencies greater than 20 Hz. Dii) and Eii) show similar raster plots and plots of competition and synchrony for $\tau_I = 13$ ms, again heterogeneity decreases competition and increases synchrony in a very similar manner to $\tau_I = 5$ ms. Solid lines represent the f_1 shown in the above raster plots. F) Plots show differences (heterogeneous – homogeneous) in mean competition and synchrony for tau = 5 ms plotted as f1 against f2 on separate axes. G) Same as (F) except tau = 13ms.

3.3 Results

3.3.1 *Kainate-evoked network oscillations in ACC.*

Glutamatergic excitation via bath application of the kainate receptor agonist kainic acid (KA; 800 nM) was the sole pharmacological manipulation necessary to produce a range of network oscillatory activity. Example power spectra with the

associated local field potential (LFP) traces from three different experiments showed that the ACC oscillations could consist of either a single peak at beta frequencies (n = 81/109; 74%), a single peak at gamma frequencies (n = 16/109; 15%) or dual peaks at both beta and gamma frequencies (n = 12/109; 11%), (Fig. 3.1aAi). Oscillations at gamma and beta frequency could be observed in both deep and superficial layers. LFP recordings from all layers of ACC were combined and the frequency of the oscillation evoked varied from 18 Hz to 44 Hz (n = 109 slices) but resulted in a bimodal distribution with peaks at beta frequencies (~24 Hz) and gamma frequencies (~34 Hz) (Fig. 3.1Aii). The slightly higher body temperatures present *in vivo* likely shift the distribution to slightly higher natural frequencies.

3.3.2 *Local network inhibition*

IPSPs were recorded during KA-evoked field oscillations from morphologically unidentified cells in ACC (n = 10) and a variety of different IPSP properties were observed. When a beta frequency oscillation was recorded in the LFP the IPSPs recorded intracellularly were either rhythmic with the recorded LFP (Fig. 3.1Bi) or non-rhythmic with the concurrently recorded LFP (Fig. 3.1Ci). If the IPSPs were non-rhythmic at the LFP frequency (Fig. 3.1Ci), they still exhibited rhythmicity, but with a peak power below ~12 Hz. When dual beta-gamma oscillations were recorded in the LFP, the IPSPs were either rhythmic at both frequencies (Fig. 3.1Di) or at only beta (Fig. 3.1Ei), or gamma (Fig. 3.1Fi), frequency.

The decay times for the IPSPs that were rhythmic with the beta frequency field oscillation were slower (modal peak 15 ± 3.5 ms; Fig. 3.1Bi) than IPSPs found to be

rhythmic with the gamma frequency field oscillation (modal peak was 6 ± 1.8 ms; Fig. 3.1Fi). In total 8/10 cells were rhythmic with the field at either beta or gamma frequencies. Overall the results demonstrated that network inhibitory inputs mostly correlated with the bimodal nature of peak spectral frequencies seen in local field potentials such that IPSPs were largely either at beta or gamma frequency only. A correlation between field and IPSP frequency has been reported many times for network oscillations in primary sensory and polymodal association areas, reflecting the critical role of synaptic inhibition in shaping fast network dynamics (Whittington et al., 2011).

The above results revealed nothing unique in the profile of synaptic inhibition in ACC that could reflect the proposed hub-specific dynamic behavior that we predicted should be present in this region. We therefore switched our attention to examining the intrinsic principal neuronal properties that are known to be diverse in both rat (Yang et al., 1996; van Aerde and Feldmeyer, 2015) and primate PFC (Ardid et al., 2015).

3.3.3   ACC intrinsic cell properties

We recorded from a total of 61 cells in the ACC in the presence of excitatory transmitter blockers (see Methods) and found a wide variety of intrinsic properties (IPs) as has been previously reported in the prelimbic and infralimbic regions of the PFC (Yang et al., 1996; Dembrow et al., 2010; Gee et al., 2012; van Aerde and Feldmeyer, 2015; Glykos et al., 2015).

Initially, cells were characterized manually, segregating cells according to their AHP shape and firing characteristics from step and tonic depolarizations. Figure 2A illustrates the variety of electrophysiological characteristics, we organized into manually

created categories (Groups 1-5). The presence of a distinct fast AHP was evident in some cells, either with or without, an after-depolarization (ADP) potential. Tonic injected current at the threshold for spiking showed some cells fired continually, while others fired less frequently, with a low frequency intrinsic sub-threshold oscillation (ISO) evident between spikes. Other cells did not fire at all upon depolarization, or required rapid acceleration of depolarizing current to produce any spikes. Some cells had very little spike accommodation while others had very fast adapting properties. The five manually classified Groups were defined as follows (Fig. 3.2A): Group 1 (11/61 18% of cells) had an AHP duration (~ 200 ms), usually with a small ADP, little spike adaptation and a spiking frequency of ~5 Hz at threshold. Group 2 (27/61 44% of cells) had similar properties to Group 1 with respect to spike adaptation, but the AHP had a more variable duration (~100-500 ms), and firing rates at threshold were less regular. Group 3 (3/61 5% of cells) had a sharp AHP, clear spike adaptation and irregular firing rates at threshold. Group 4 (14/61 23% of cells) had very strong spike adaptation, rounded, short AHPs and little or no firing after the initial spikes at threshold. Group 5 (6/61 10% of cells) always had a characteristic fast AHP, interrupted by an ADP, then a long AHP and exhibited strong spike adaptation. Without morphologically identifying cells we could not determine if any of these groups corresponded to classes of interneurons, rather than putative pyramidal cells, but no distinct fast-spiking (FS) interneurons were recorded in this study.

In all cells we measured 10 intrinsic properties (IP1 - IP10) (Fig. 3.2B) which were as follows: IP1, action potential amplitude; IP2, I_h estimate; IP3, AHP amplitude;

IP4, total AHP magnitude; IP5, AHP time to maximal deflection; IP6, spike width at half-height; IP7, spontaneous spike rate at threshold; IP8, resting membrane potential; IP9, initial spike frequency on step depolarization; IP10, ratio of 3rd to 2nd inter-stimulus interval on step depolarization-induced spike train (see Methods). Each of these IPs reflects the presence and magnitude of intrinsic conductances that are known to influence neuronal resonance (input-filtering) properties (see Discussion). The IPs of all cells were compared across each of the manually selected groups (Groups 1 - 5), but very few significant differences were found, and those that were identified did not show any obvious pattern (Fig. 3.2B). In addition, the distribution of cells in Group 1 - 5 across the laminar structure of ACC was diffuse as most cell types could be found in all layers (Fig. 3.2C,D). These data demonstrate that in the ACC different cell classes could not be defined either by a unique expression of ion channel properties or by laminar position.

In order to assess whether ACC cells could be separated into discrete clusters both hierarchical and k-means clustering were used in an attempt to segregate the cells, assuming between 2 and 10 clusters. The Davies-Bouldin Index and the Dunn's Index for a range of clusters from 2 to 10 for all clustering methods used in this study are plotted (Fig. 3.3A,B). In the Davies-Bouldin plot (Fig. 3.3A), the lower the index value, the better the cluster separation. Using the Dunn's Index (Fig. 3.3B), the higher the index value, the better the cluster separation. K-means performed the best overall at various cluster sizes, followed by manual clustering and finally the shuffled data gave the worst performance. The hierarchical cluster analysis performed best at the 2 cluster level but other values on, or close, to the zero line suggest this analysis failed at higher cluster

numbers. However, although these data show our manually selected clusters performed better than the shuffled data, the clusters were still not clearly separated by any method used here. All clustering of cells found using the different methods are shown for 3, 4 and 5 assumed clusters on 2D plots (Fig. 3.3C) of the first two canonical variables from the MANOVA analysis. For k-means clustering, at the 3-cluster level (Fig. 3.3Ciii, left graph), all three clusters were significantly different from each other in the first canonical variable dimension (x-axis; P <0.05). However, although the k-means method performed optimally out of the chosen methods in terms of the validity tests (Dunn's and Davies-Bouldin indicies) as described above, two of the clusters (green and blue) can be seen to lie along a continuum, with no clear space separating them. In addition, relating these clusters individually back to the original electrophysiological characteristics yielded few significant differences, similarly to the manually selected clusters. At the 3-cluster level using k-means, one cluster was separable (P <0.05) in terms of spike rate at threshold, and one other cluster was separable (P <0.05) in terms of resting membrane potential.

3.3.4   *Biophysical diversity reproduces IP diversity in computational cell models*

The above analyses strongly suggested a broad continuum of intrinsic ACC principal cell properties. To understand how such a situation may influence local network behavior, we first modeled this diversity computationally. A set of biophysical computational ACC cell models was generated to capture the above spread of IP values. Cells in this model could reproduce the firing properties of cells observed experimentally (Fig. 3.4A). A range of ion channel conductances was identified for each of 8 different ion channels that reproduced the distribution of IP values recorded experimentally (Fig.

3.4B). Notably, this method did not explicitly constrain IP distribution shapes, yet the simulated IPs distributed similarly to the experimental IPs in most cases (Fig. 3.4C). Five IPs explained >85% of the total variance in the experimental data (IP5 AHP duration; IP6 spike width; IP7 spike rate at threshold; IP8 resting membrane potential; IP9 instantaneous spike frequency), and were included in the model. In addition, we also compared the correlations between z-scored IP values recorded in each cell, with those from all model cells. This analysis showed that each experimental cell had at least one model cell with a value of $R^2 > 0.85$, and 90% of experimental cells had at least one model cell with $R^2 > 0.9$, indicating a very high correlation between the experimental and modeled IP values.

3.3.5   Beta and gamma frequency rhythms were generated by different inhibitory decay constants in an ACC network model

In order to predict a possible role for the observed heterogeneity of IPs the range of E-cells modeled above were combined with local circuit interneurons and inserted into an ACC network model (Fig. 3.5). Results from this model were compared with a model containing homogeneous E-cell populations in which the intrinsic properties were the same for all cells in the population (see Methods). Heterogeneity was based on model parameters drawn from a multivariate distribution that preserves the correlation between the biophysical parameters producing cell responses constrained by experimental IPs (see Methods).

The different beta- and gamma frequencies observed experimentally could be replicated in both the heterogeneous and homogeneous E-cell-containing models by

switching the interneuron population inhibitory decay time constant (τ) from 5 ms to 13 ms (Fig. 3.5) consistent with experimentally observed values in cells with activity locked to gamma- and beta-rhythms, respectively (see above). Simulation of all the heterogeneous E-cell models resulted in a broad distribution of oscillation frequencies, predominantly within either the beta or gamma frequency band, depending on the set inhibitory decay time constant (Fig. 3.5). This effect was similar regardless of whether the E-I assembly was driven by background activity (Poisson noise) or a rhythmic input. In both cases cell diversity broadened the range of frequencies generated by the networks, but with different inhibition time constants resulting in largely separable frequency ranges at beta and gamma frequency (Fig. 3.5C,D).

3.3.6   Network heterogeneity decreases competition and increases synchrony among multiple assemblies.

The above simulations led us to hypothesize that the experimentally observed heterogeneity in ACC might confer a computational advantage to a region that may have to combine multiple inputs at different peak frequencies within a given EEG band. To compare the effects of two different inputs on both the homogeneous and heterogeneous E-cell networks, we ran simulations with two E-cell assemblies connected to the same I-cells both receiving external rhythmic inputs (Figure 6A). With this model configuration we then assessed whether heterogeneity of cell properties in the model altered the network's response to multiple different inputs. Competition and synchrony were compared between the networks with homogeneous and heterogeneous E-cell assemblies with a shared pool of inhibitory interneurons (I-cells) and $\tau_I = 5$ ms and $\tau_I = 13$ ms

(Fig. 3.6A-Ei). Figure 6B shows example raster plots for two assemblies driven by rhythmic inputs at 20 Hz and 50 Hz. In the homogeneous network, assembly E2, driven by an input at 20 Hz dominated overall activity, even though assembly E1 was being driven by an input with faster 50 Hz modulation across the population. When spiking occurred in the less active assembly (E1), it had a moderate degree of synchrony with the dominant assembly (E2). In contrast, in the heterogeneous network, receiving the same 20 Hz and 50 Hz inputs, both assemblies were now able to sustain more equal activity levels throughout the simulation, and with a greater degree of overlap in spike timing. Very similar results were obtained with interneuron population inhibitory decay time constants at both $\tau_I = 5$ ms and $\tau_I = 13$ ms. These examples emphasize how, a wider diversity of cell properties within assemblies, can increase the spike synchrony and decrease competition among multiple assemblies. Over a range of input frequencies f_1 and f_2, the degrees of competition and synchrony between target assemblies E1 and E2 were related to the proximity of their input frequencies. Competition in the heterogeneous network was reduced across all values of f_1 and f_2. Furthermore, for assemblies driven by inputs separated by more than 30 Hz (i.e., across EEG beta and gamma frequency bands), heterogeneity significantly increased spike synchrony.

Similarly, in separate simulations where only one cell assembly (E1) received an external rhythmic input and the other assembly (E2) received an equal rate Poisson noise, the degree of competition and synchrony between target assemblies E1 and E2 were related to the frequency f_1 of the external rhythm (Fig. 3.6A-Eii). However, in this condition the interaction involved E1 following an external rhythm and E2 exhibiting a

noise-driven local rhythm at its natural frequency (as in Fig. 3.5A). Given this interaction between external and local rhythms, heterogeneity reduced competition across all values of f_1 to a greater extent than occurred for two assemblies driven by external rhythms. Furthermore, a wider diversity of cell properties increased spike synchrony between externally-driven and locally-generated rhythmic assemblies to a greater extent for beta- and gamma-rhythmic inputs. Again, very similar results were obtained with interneuron population inhibitory decay time constants at both $\tau_I = 5$ ms and $\tau_I = 13$ ms (Fig. 3.6A-Eii). Reploting the data as f1 versus f2 along separate axes for both $\tau_I = 5$ ms and $\tau_I = 13$ ms shows the largest reduction in competition and increase in synchrony within the beta and gamma frequency bands (Fig. 3.6F,G).

3.4 Discussion

The present findings support the evidence that ACC generates gamma and beta frequency oscillations as a consequence of local circuit interactions between principal cells and interneurons. This type of local circuit behavior is near-ubiquitous in cortex (see Whittington et al., 2011 for review). The generation of beta- and gamma frequency activity does not, alone, therefore present any clues as to the proposed hub-like role of ACC in combining multiple inputs required for its general role in cognitive control (Lapish et al., 2008; Durstewitz et al., 2010; Shenhav et al., 2013; Ma et al., 2014). However, in ACC we found that this fundamental, inhibition-based mechanism of rhythm generation was present, along with considerable heterogeneity of principal cell intrinsic

properties. Computational modeling predicted that an inhibition-based oscillation, combined with such heterogeneity, would have a limited effect on the locally-generated rhythm, but a potent effect on the network's response to diverse oscillatory inputs. Neuronal response heterogeneity caused a transition from a network behavior in which frequency-selected single inputs generated a single local ACC network output, to a combinatorial behavior in which the network could combine oscillating inputs of different frequency.

3.4.1   *Local generation of gamma and beta oscillations*

We have demonstrated that gamma- and beta frequency oscillations can be evoked in the ACC *in vitro* with application of KA alone. This is consistent with data *in vitro* from the hippocampus (Hajos et al., 2000; Hormuzdi et al., 2001; Fisahn, 2004) and neocortex (Roopun et al., 2008a; Anver et al., 2010; Ainsworth et al., 2012) where KA application has also been shown to evoke fast network oscillations in the 20-80 Hz frequency range. Network oscillations in the beta- and gamma frequency range in ACC are dependent upon $GABA_A$ and AMPA receptors (Steullet et al., 2014). With the exception of beta rhythms in parietal association areas (Roopun et al., 2006), this pharmacological profile is consistent with other local cortical gamma and beta oscillations that are an emergent property of the network, and reflect the activation by KA of a reciprocally connected pyramidal-fast spiking interneuron network (Whittington et al., 2011).

The distinction between gamma- and beta frequency oscillations corresponded to the presence of IPSPs with different decay kinetics recorded from morphologically

unidentified cells in ACC. The IPSP values obtained were consistent with the kinetics of GABA$_A$ receptor-mediated events associated with gamma oscillations in hippocampus and neocortex and beta oscillations in auditory cortex (Whittington et al., 1995; Ainsworth et al., 2011). The most parsimonious explanation for these two different frequencies of network activity, and two different inhibitory decay times, would be that distinct interneuron subtypes differentially contributed to the beta- and gamma frequency oscillations (Roopun et al., 2008a). The kinetics of GABA$_A$ receptor-mediated inhibition is known to be slower at receptors containing the ϵ "modulatory" subunit (Wagner et al., 2005) and at synapses on distal dendrites (Harney and Jones, 2002). Thus, the different IPSP kinetics observed could result from interneuron subtypes providing inhibition through synapses at different postsynaptic sites or involving GABA$_A$ receptors with different molecular composition. PV- and somatostatin (SOM)-expressing interneurons in the PFC have been shown to provide somatic versus dendritic inhibition (DeFelipe, 1997) and to contribute to distinct behavioral functions (Kvitsiani et al., 2013; Pinto and Dan, 2015). Such interneuron subtype-specific functions might therefore correlate with the distinct network activities at beta frequencies, paced by the PV+ subtype, and gamma frequencies, paced by the SOM+ subtype. Beta frequency oscillations have been proposed to play a role in establishing functional long-range connections, while gamma frequency oscillations are thought to be more important for local interactions (Donner and Siegel, 2011; Kopell et al., 2010). In addition, gamma frequency activity may mediate feed-forward interactions while beta frequency activity has been proposed to mediate feedback interactions (Bastos et al., 2012; Bastos et al., 2015), but see below.

3.4.2   Variability of oscillatory inputs to ACC

A principal underlying the role of oscillations in determining functional connectivity between brain areas is that, within a classical EEG frequency band, they provide a mechanism by which neurons generate outputs at times appropriate for optimizing their mutual influence (Ainsworth et al., 2012). In order for this so-called "communication through coherence" to occur, matching the phase and frequency of oscillations in the connected areas is important (Fries, 2005). However, even within a classical EEG band the network oscillation frequencies can vary enormously. In the case of gamma oscillations, frequency can vary as much as 20 Hz depending on the region of origin (Herrmann et al., 2010; Middleton et al., 2008) and the properties of the sensory input that generates them (Perry et al., 2015; Orekhova et al., 2015). Similarly, beta oscillations in different brain regions may vary in peak frequency by up to 10 Hz (e.g., Roopun et al., 2008b; van Burik et al., 1998).

Within brain regions, receiving concurrent oscillating inputs in the gamma or beta EEG bands, even subtle frequency differences have been predicted to have dramatic effects. In networks where the dominant time-constant governing rhythmicity is that of synaptic inhibition, one input driving a slightly faster frequency than another can effectively abolish any influence the slower frequency has on local spike generation (Chapter 2; Cannon et al., 2013). Similarly, synchronous inputs can be readily separated from asynchronous inputs (Chapter 2; Akam and Kullmann, 2010), but if multiple inputs arrive at similar frequencies they can become mutually distracting (Akam and Kullmann, 2014). Therefore, if a local network such as the ACC is to combine multiple oscillating

inputs, a network property additional to the rhythmicity afforded by local inhibition must be present. Data and computational modeling presented here strongly suggest that heterogeneity in intrinsic neuronal electrophysiological properties may provide such a combinatorial advantage to the network.

3.4.3   Intrinsic electrophysiological properties of neurons in ACC.

Neurons recorded in this study could be subjectively divided into five broad groups similar to those described in other PFC regions (Yang et al., 1996; Dembrow et al., 2010; Gee et al., 2012; Lee et al., 2014; van Aerde and Feldmeyer, 2015; Glykos et al., 2015). However, using a range of established clustering algorithms, that have been used successfully in other cortical areas to identify distinct neuronal clusters based on electrophysiological properties (Sosulina et al., 2006; Keshavarzi et al., 2014; Ferrante et al., 2016), we did not identify distinct clusters. Three significantly different clusters could be distinguished using k-means clustering, but the clusters were not well separated and they could not be replicated using hierarchical clustering. Our data, therefore, suggest there is in fact a broad continuum of electrophysiological properties present in ACC neurons with this heterogeneity mediated by the relative density of intrinsic conductances, including passive and voltage-gated potassium channels, persistent sodium channels and HCN channels. These channels have overt effects on intrinsic neuronal properties (He et al., 2014), and are vital for controlling the resonance and thus dynamic input-filtering properties of neurons (Chapter 2; Hutcheon and Yarom, 2000). In turn, band-pass and competitive input filtering are vital for input selection and routing of oscillatory inputs (Kopell et al., 2010; Akam and Kullmann, 2010, 2014).

Neocortical areas can also exhibit considerable heterogeneity in electrophysiological properties as evidenced by the recent extensive documentation of neuronal circuits within the somatosensory cortex (Markram et al., 2015). As discussed by Markram and colleagues, in addition to intrinsic properties, there can also be heterogeneity of synaptic properties such as decay times, synaptic depression and facilitation, which can vary between cell types (Thomson et al., 1996). However, Markram et al., (2015) describes electrically stimulated and spontaneous activity in the neocortex, and not the properties of neurons during an emergent network rhythm, such as beta and gamma frequency activity. Our data demonstrate there is little variability in, for example, decay times of the IPSPs which correlated with either the beta- or gamma frequency field oscillation.

One interesting feature we observed was the lack of any clear laminar segregation in the generation of either beta or gamma frequency activity within the ACC. This is in marked contrast to other neocortical areas where several studies *in vitro* have shown that gamma frequency activity is generated in the superficial layers (II/III), while beta frequency activity arises from deep (V/VI) layers (Roopun et al., 2008a; Ainsworth et al., 2012). No such obvious laminar distinction was seen in this study, and both beta- and gamma frequency activity could be recorded from all layers. This difference in organization may reflect the absence of a functional layer IV in ACC, or may in fact reflect the integrative function of ACC, such that oscillations of different frequencies occur across all the laminae.

3.4.4   Consequences for ACC functionality in a dynamic network

The data and model presented here suggested that the modal peak frequency of an oscillation in ACC was predominantly governed by the time course of synaptic inhibition. This was the case, both when the observed diversity of intrinsic properties was used, and when principal neuron properties were homogeneous. The biggest difference made by the observed intrinsic heterogeneity was a broadening of the input filtering characteristics of the model ACC network, and a resulting ability of the network to respond to multiple inputs of differing frequencies concurrently within either the gamma or beta EEG bands. This is consistent with the ideas of Seamans' and colleagues who consider ACC as consisting of "overlapping cell assemblies encoding various cognitive events involved in a decision making process" (Lapish et al., 2008; Durstewitz et al., 2010; Ma et al., 2014). The emergence of a broader range of local and resonant frequencies, afforded by cellular diversity, would promote diverse inputs to equally influence the same target (ACC).

Interestingly, with the degree of model heterogeneity constrained by the biological data gathered, the broadening of input filter characteristics predicted a decrease in competition and increased synchrony between ACC regions receiving or generating both gamma and beta frequencies. This seems antagonistic to proposed functions of discrete frequency bands such as hierarchical organization of signals (Lakatos et al., 2005), concatenation (Roopun et al., 2008b) and segregation of top-down and bottom-up signals (Bastos et al., 2015). However, with ACC sitting at the top of the functional connectivity hierarchy in the cortex these 'rules' need not apply, e.g. there is no overt

'top-down' input to ACC. In addition, broader filter characteristics were predicted to powerfully reduce competition and increase synchrony when comparing a discrete input frequency with noise alone. This may be seen as a negative property – allowing ACC to generate associations where there are none (e.g. when they are "cognitively false' (Straube et al., 2011)). However, it may also underlie the observed role of ACC in the formation of novel 'intuitive' associations (Jung-Beeman et al., 2004; Mai et al., 2004).

3.4.5   Conclusions

A dynamic approach to understanding functional brain connectivity has previously shown that information held in neuronal oscillations can be selected and routed through the cortex on the basis of frequency- and coherence-related competition. Here we present an additional dynamic process whereby different frequencies of oscillation can be combined together. The phenomenon is facilitated by the interplay between the kinetics of fast synaptic inhibition (which sets the 'center frequency' for a given oscillation band) and the degree of heterogeneity in intrinsic electrophysiological properties of principal cells (which sets the bandwidth). Although this study has focused on ACC, it is possible similar mechanisms could be used in other hub regions, where diverse inputs are integrated. A synergistic interplay between synaptic inhibition and intrinsic electrophysiology would provide a rich functional network structure that would be highly labile to neuromodulatory substances such as acetylcholine, dopamine and noradrenaline (Carr et al., 2007; Hasselmo and Sarter, 2011; Gee et al., 2012; Dembrow and Johnson, 2014). We suggest that neuromodulators may modulate the degree of hub-

like or input-selective functionality of higher brain structures to influence cognitive functions (Deco and Rolls, 2003).

CHAPTER 4

CONCLUSION

Decades of research have highlighted the importance of prefrontal cortex for cognitive control as well as the ubiquity of neural oscillations throughout the brain. Recent work has begun to elucidate the ways in which network oscillations can contribute to cognitive processing; for instance, cortical networks can perform frequency- and coherence-based filtering of signals among convergent pathways based on resonance with feedforward inhibition (Akam and Kullman, 2010) and feedback inhibition (Cannon et al., 2014). The work presented in this dissertation builds on these previous findings in two important ways. First, in Chapter 2, I explored how interneuron-mediated lateral inhibition supports frequency- and coherence-based selection among parallel pathways (i.e., rhythm-mediated competitive gating). Second, in Chapter 3, we found that principal cell heterogeneity can switch a network from a selective mode where only one input is processed to a combinatorial mode where multiple inputs can be processed simultaneously.

These microcircuit properties have important consequences for cognitive control operations mediated by LPFC and ACC. Rhythm-mediated competitive gating supports selective gating of outputs from a LPFC working memory (WM) buffer. Given a WM attractor network with persistent activity in some set of spiking cells, synchronization of a subset in a resonant oscillation can determine which of the persistently active cells will have their activities reflected in a feedforward output layer, and thus constrain the subset of WM-coding cells available for downstream read-out. If the feedforward projections

from the WM buffer to the output layer have parallel channels representing alternative input-output mappings, then synchronization of select inputs in a resonant oscillation can constrain the input-output mapping that is selected given a particular stimulus. Furthermore, given context-dependent synchronization, this mechanism supports rule-based selection of input-output mappings. Outputs, in turn, could provide biases directing action selection (through projections to premotor cortex, ventral thalamus, or striatum) or attentional control mechanisms (through projections to thalamic reticular nucleus or posterior association cortex). Changes in the active rule could be caused by ACC-induced changes in synchronization, possibly mediated by CB+ interneurons in the superficial layers of LPFC.

In contrast, the extensive heterogeneity of principal cell intrinsic properties characterized in Chapter 3 endows ACC with the ability to respond non-selectively to multiple inputs from source networks in different dynamical states. Source networks in regions with different natural frequencies, for instance, OFC, amygdala, and hippocampus, could deliver signals related to the outcomes of present actions and be integrated in ACC for monitoring performance based on multiple lines of evidence. This combinatorial processing could support rate-based evidence accumulation, for instance, in superficial ACC, driving rate-thresholded response gates, for instance, in deep ACC, that output control signals governing resource allocation. Deep layer control signals from ACC could potentially trigger rule updating through their projections to superficial CB+ cells in LPFC as described above. The ACC control signal could either directly select the rule through specific projections or trigger a nonspecific update mechanism with rule-

specificity provided by contextual inputs from other regions (e.g., ventral hippocampus). These mechanisms could be coordinated with other mechanisms for routing signals through LPFC (e.g., BG-mediated inhibitory gating for updating WM buffers).

This perspective on ACC/LPFC dynamics for process monitoring, rule updating, and rule application represents a hypothesis based on the mechanisms we have identified and what is known about neural anatomy and the localization of cognitive operations. However, the rhythm-mediated competitive gating and processing mode control mechanisms we have reported are general features of neural networks with interacting principal cells and interneurons providing strong feedback inhibition. Thus, they may find application in various cognitive processes involving regions throughout the brain.

While much has been learned about the link between mind and brain over the last century, new technologies and a growing community of increasingly connected researchers are sure to make the next century even more enlightening. Close collaboration between experimentalists and modelers will remain essential for distilling the mechanistic principles that underlie information processing and neural function. Whatever concepts and metaphors prove to be useful, a deeper understanding of neural mechanism (i.e., how the brain works) will open the future to boundless opportunities for enhancing, healing when dysfunctional, and more greatly appreciating the mental experience with which we so deeply identify.

APPENDIX A: The DynaSim Toolbox

Introduction

DynaSim is a Matlab/Octave toolbox I developed for rapid prototyping of large neural models, batch simulation management, and efficient model sharing. It is designed to speed up and simplify the process of generating, sharing, and exploring network models of neurons with a few compartments. Its aim is to enable researchers to focus on model details instead of implementation. It facilitates rapid prototyping by enabling models to be specified using equations with conventional mathematical notation (Fig. A.1-2), similar to XPP (Ermentrout, 2002) and Brian (Goodman and Brette, 2008), built-in Matlab functions, and predefined, mechanistically-meaningful model objects (Fig. A.3-4), similar to objects in Brian and mechanisms in NEURON (Hines and Carnevale, 1997). DynaSim's high-level specification, described below, easily scales to arbitrarily complicated population models and networks of interconnected populations (Fig. A.4). It is most similar to the Brian simulator in spirit, scope, and its ability to simulate models based on equations as well as libraries of preexisting model objects (Goodman and Brette, 2009). The software has been implemented in Matlab because Matlab lacks advanced tools for neural modeling, despite its popularity and a growing interest in modeling neural systems. DynaSim incorporates the best features of existing simulators to fill the niche for neural modeling in Matlab.

DynaSim also includes a unique set of features to simplify the processes of exploring model dynamics over parameter spaces (Fig. A.5), running separate

simulations in parallel on a compute cluster, as well as parallel analysis and plotting of large numbers of simulated data sets. It increases simulation speed, compared to common Matlab implementations, using a combination of optimized vector computation, C compilation, and parallel simulation. It includes a graphical user interface (DynaSim GUI) that supports full functionality without requiring user programming (Fig. A.6). The GUI can be used as a powerful aid for teaching about the dynamics of neural systems. The design of DynaSim incorporates a simulator-independent model specification to facilitate interoperability with other tools outside Matlab including other simulator-independent specifications (e.g., NeuroML, SBML), simulators (e.g., NEURON, Brian), model repositories (e.g., Open Source Brain), and web-based applications (e.g., Geppetto). The hope is that DynaSim will reduce barriers to exploring dynamics in complicated neural models, facilitate collaborative modeling, and complement other tools being developed in the neuroinformatics community.

This Appendix will begin with examples demonstrating the simplicity and power of DynaSim for rapid prototyping and model exploration. That will be followed by technical details on the mechanics of how DynaSim works. Then an associated model repository, InfiniteBrain, will be introduced. The Appendix will end with an overview of progress at community development and available resources, including a tutorial on using the DynaSim toolbox.

Worked examples

Example 1: Lorenz equations

Any system of ordinary differential equations (ODEs) can be modeled in DynaSim by listing equations using conventional mathematical notation. Equations can be listed in a single string or a cell array of strings and may contain parameters, functions, conditional statements, ODEs and their initial conditions (ICs). To demonstrate the generality of this approach, the Lorenz equations (Lorenz, 1963) are defined in the cell array `eqns` in Fig. A.1A, and the system is numerically integrated by passing the user specification (i.e., `eqns`) to the DynaSim function `SimulateModel`. Integration in DynaSim is described in the Technical details. The results are plotted in Fig. A.1B. The same approach could be applied to simulate ODE-based rate models of neural systems.

A

```
eqns={
  's=10; r=27; b=2.666';
  'dx/dt=s*(y-x);   x(0)=1';
  'dy/dt=r*x-y-x*z; y(0)=2';
  'dz/dt=-b*z+x*y;  z(0)=.5';
};
data=SimulateModel(eqns);
plot(data.pop1_x,data.pop1_z)
```

B
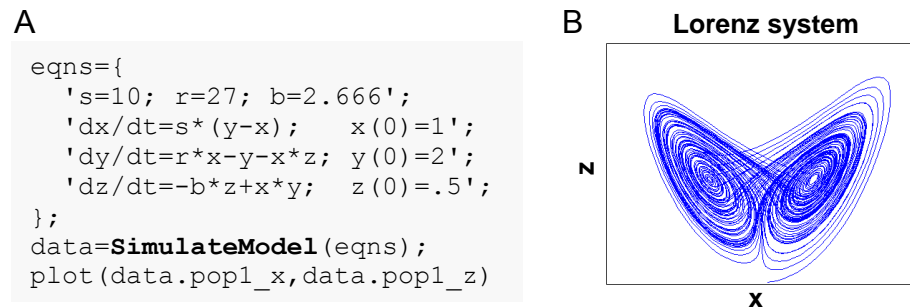
Fig. A.1. Simulating a simple system of ordinary differential equations in DynaSim. (**A**) Matlab code using the DynaSim toolbox. Simulation is achieved by passing a model specification to the DynaSim `SimulateModel` function. Simulated data are returned in a DynaSim `data` structure. (**B**) (x,z) phase plane of Lorenz system.

Example 2: Izhikevich spiking neuron model

The Izhikevich neuron (Izhikevich, 2003) is a system of differential equations with a conditional reset. Fig. A.2A demonstrates the specification of an Izhikevich model

using a cell array of strings and a noisy time-varying input function that leverages the built-in Matlab function `rand`. See the tutorial for details on incorporating conditionals: `if(condition)(actions)`. Input and simulated output are plotted in Fig. A.2B.

A

```
eqns={
  'a=.03; b=-2; c=-50; d=100; vpeak=35; vr=-60';
  'I(t)=70*(t>200&t<800)*(1+.5*rand)';
  'dv/dt=.01*(.7*(v-vr)*(v+40)-u+I(t)); v(0)=vr';
  'du/dt=a*(b*(v-vr)-u); u(0)=0';
  'if(v>vpeak)(v=c; u=u+d)';
};

data=SimulateModel(eqns,'time_limits',[0 1000]);
figure
subplot(2,1,1); plot(data.time,data.pop1_v);
subplot(2,1,2); plot(data.time,data.pop1_I);
```

B
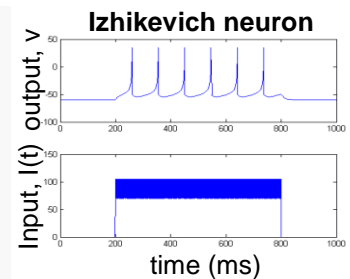
Fig. A.2. Simulating an ODE system with conditional reset and stochastic drive.
(**A**) Matlab code using the DynaSim toolbox. The model is specified using a cell array of strings, `eqns`, listing equations defining parameters, an input function `I(t)`, ODEs with ICs, and a conditional reset. The stochastic input uses the built-in Matlab function `rand`. (**B**) Plot of the time-varying input and simulated output.

Example 3: Hodgkin-Huxley-type spiking neuron models

The construction of large models with many equations can be greatly simplified by utilizing components from a library of preexisting model objects. For instance, conductance-based neuron models often include component ion currents (i.e., ionic mechanisms) that may be used in models of different neuron types. A regular spiking (RS) neuron may include fast spike-generating sodium (e.g., iNaF) and potassium (e.g., iKDR) currents, while an intrinsically bursting (IB) neuron includes the same spike-generating currents plus a slower potassium current (e.g., iM) providing a second time

scale separating bursts of spikes. Both models rely on the same iNaF and iKDR currents while the IB model incorporates an additional iM current.

DynaSim expedites the construction of such models by leveraging preexisting mechanism sub-models (e.g., iNaF, iKDR, iM). In the case of one or a population of cells with dynamics shaped by the same mechanisms, models can be specified using strings listing equations with two additional features: (1) an ODE (e.g., voltage dynamics) containing a placeholder for terms defined in external model objects and (2) a list of objects (e.g., ionic mechanisms) contributing to the dynamics. Fig. A.2A demonstrates the specification of a biophysically-detailed IB neuron using a placeholder, `@current`, in the voltage dynamics, `dV/dt`, and a list of ionic mechanisms, `{iNaF,iKDR,iM}`, affecting the dynamics. Fig. A.2B plots the simulated response to a tonic injected current. The IB neuron could be rapidly converted into a RS neuron simply by reducing the list of mechanisms to `{iNaF,iKDR}`. Alternatively, the neuron model could be made arbitrarily more complicated by adding to the mechanism list as many ion currents as desired. This method is described further in the Technical details section below.
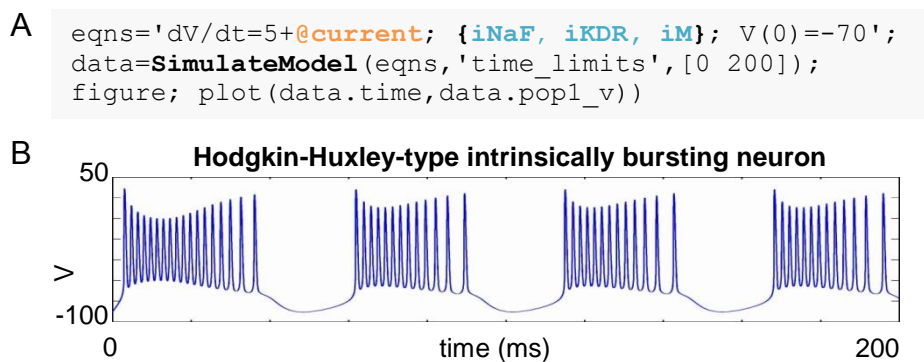
Fig. A.3. Simulating a biophysically-detailed neuron model using mechanisms.
(**A**) DynaSim model leveraging existing model objects for iNaF, iKDR, and iM currents to simplify the specification of a detailed neuron model. (**B**) IB response to tonic current.

Example 4: Weak PING spiking network model

The construction of complicated network models can be greatly simplified by introducing an additional higher-level model object, the population, with connections between populations and dynamics dependent on lower-level mechanisms. Fig. A.4A demonstrates an object-based network architecture with two populations (E and I), each with dynamics shaped by ionic mechanisms. Voltage dynamics of the E population is shaped by intrinsic ion currents (ina, ik) and an inhibitory synaptic current (iGABAa) that depends on the state of the presynaptic I population. Similarly, the I population has voltage dynamics shaped by the same intrinsic currents (ina, ik) and an excitatory synaptic current (iAMPA) that depends on the E population. Given the kinetics of the predefined ionic mechanisms and the parameters used in this example, this network generates a weak pyramidal-interneuron network gamma (PING) rhythm (see Chapter 1 for more details on neural systems exhibiting weak PING dynamics).

DynaSim expedites the process of specifying object-based network models using a high-level DynaSim `specification` structure that organizes information about the population-level equations and the mechanisms on which they depend. To facilitate the computational implementation of an object-based conceptual network model (like the example in Fig. A.4A), information is organized into two fields of the `specification` structure: `populations` and `connections`. Patterns of connectivity between source and target populations are specified using connectivity matrices that appear in the equations of their connection mechanisms (e..g, synaptic currents). Fig. A.4B demonstrates the DynaSim specification of the weak PING model shown in Fig. A.4A as

well as raster plots and an overlay of voltage traces showing a 40Hz network oscillation in response to a tonic drive. Similar to the mechanism-based specification of the IB neuron in Example 3, the network model can be rapidly adjusted and made as complicated as desired by simply updating mechanism lists for each population and for the connections between populations. This method is also described further in the Technical details section below. It is worth noting that any network model specified using a `specification` structure could be equivalently specified using the more tedious method of explicitly listing all equations as described in Examples 1-2.

A

Object-based network model architecture

B

High-level specification structure

```
master_equations='dV/dt=Iapp+@current+randn(1,N_pop); {ina,ik}';
```

```
s.populations(1).name='E';
s.populations(1).size=80;
s.populations(1).equations=master_equations;
s.populations(2).name='I';
s.populations(2).size=20;
s.populations(2).equations=master_equations;
s.connections(1).direction='I->E';
s.connections(1).mechanism_list={'iGABAa'};
s.connections(2).direction='E->I';
s.connections(2).mechanism_list={'iAMPA'};
data=SimulateModel(s);
```
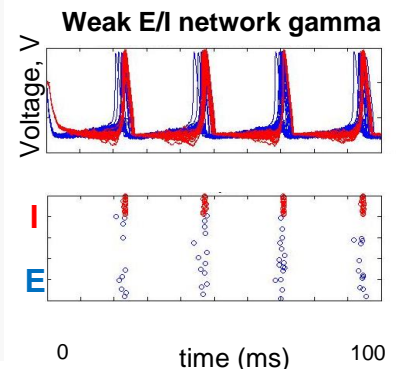

Fig. A.4. Simulating weak PING rhythms using a model specification structure.
(**A**) The conceptual object-based architecture of a biophysically-detailed E/I network. (**B**) Mapping the object-based architecture onto a DynaSim `specification` structure that contains all the high-level information necessary to construct the complete system of equations for the full model using objects from a library of preexisting ionic mechanisms.

Example 5: Exploring parameter space of the weak PING model

One of the strengths of DynaSim is its support for exploring how system behavior changes as a model is systematically varied. In the simplest case, exploration involves running sets of simulations varying model parameters and performing analysis and visualization of the results over parameter space. This can be achieved easily in DynaSim by setting the `vary` option of `SimulateModel` using a compact specification of the parameter space to explore. For instance, the space can be specified using a set of triplets (as in Fig. A.5A) with each element indicating the values to use for parameters of populations and/or connections; the space to explore is then constructed from the Cartesian product of the parameter values from the set of triplets. DynaSim offers multiple forms of specification to accommodate different patterns in parameter space.

Exploring the weak PING model is demonstrated in Fig. A.5A where 9 simulations are specified with three values for each of two parameters: the amplitude of the current injected into cells of the E population (`Iapp`) and the inhibition time constant of the inhibitory synapse onto E cells (`tauD`). DynaSim provides multiple functions for visualizing results over parameter space. For instance, Fig. A.5B shows raster plots produced by the DynaSim `PlotData` function called in Fig. A.5A, while Fig. A.5C, produced by the DynaSim `PlotFR` function, shows the dependence of average firing rates on varied parameters. See the tutorial below and online documentation for additional details.

A

```
vary={
  'E'   ,'Iapp',[0 10 20];
  'I->E','tauD',[5 10 15]
  };
data=SimulateModel(s,'vary',vary)
PlotData(data,'plot_type','raster');
PlotFR(data);
```

B

Raster plots

C

Mean firing rates (sp/s)
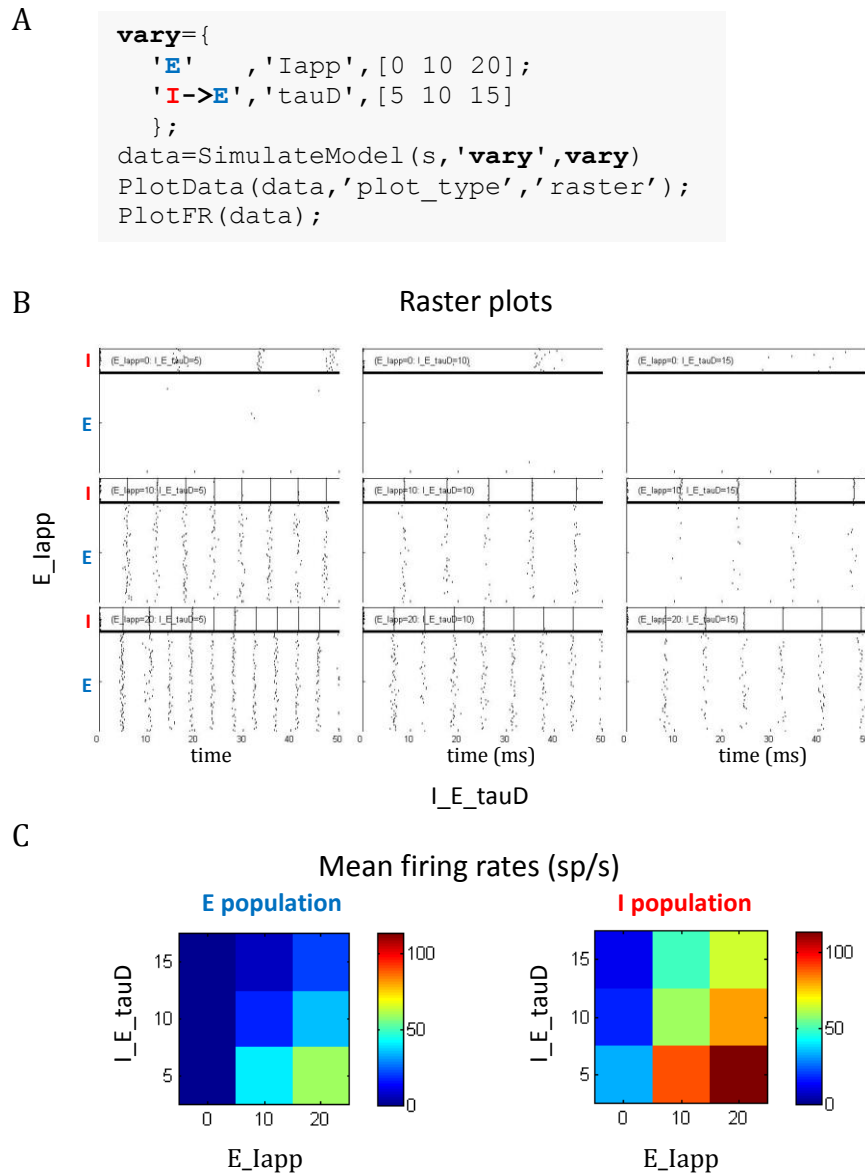
Fig. A.5. Searching parameter space using the DynaSim toolbox.
(**A**) Matlab code using the DynaSim `SimulateModel` function with the `vary` option to specify a set of 9 simulations varying two parameters (`Iapp` in population E and `tauD` of the connection from I to E). (**B**) Raster plots produced by `PlotData` with the `plot_type` option given an array of DynaSim `data` structures containing results for all 9 simulations. (C) Plots produced by `PlotFR` showing how mean firing rates for E and I populations change as a function of the two varied parameters.

The DynaSim `SimulateModel` function offers three important options for increasing the speed of simulation. The speed of any simulation can be increased by a factor of 10x to 100x by setting the `compile_flag` option to 1:

```
data=SimulateModel(s,'vary',vary,'compile_flag',1);
```

which directs `SimulateModel` to compile the simulation into C code before numerical integration. Furthermore, the time required to run a set of simulations can be increased by parallelizing separate simulations. This can be achieved using different cores on the same machine by setting the `parallel_flag` option to 1:

```
data=SimulateModel(s,'vary',vary,'parallel_flag',1);
```

Additionally, multiple simulations can be executed simultaneously on different nodes of a compute cluster supporting the "qsub" command by setting the `cluster_flag` option to 1, the `study_dir` option to a directory where jobs should save results, and then using the DynaSim `ImportData` function to load all simulation results:

```
D=pwd; % where cluster jobs should save simulation results
SimulateModel(s,'vary',vary,'cluster_flag',1,'study_dir',D)
data=ImportData(D);
```

All three options (`compile_flag`, `parallel_flag`, and `cluster_flag`) can be used in combination to achieve multiplicative benefits. Together they enable Matlab to achieve reasonable batch simulation speeds in comparison to other neural simulators. These options are described further in the Technical details section.

Example 6: Exploring the weak PING model in DynaSim GUI

In addition to the DynaSim functions available for script-based model building and simulation, DynaSim provides a unique graphical user interface (DynaSim GUI) that enables users to benefit from all features of DynaSim without the need for user programming. DynaSim GUI provides a highly flexible and dynamic environment for interactive, real-time exploration of how model functions and dynamics vary with parameters and how varying model architecture changes the system behavior. Any model can be explored using the GUI by passing its specification to the function `dynasim`. For instance, the GUI can be used to explore the weak PING model by executing: `dynasim(s)`. Fig. A.6 shows how the weak PING model appears in DynaSim GUI.
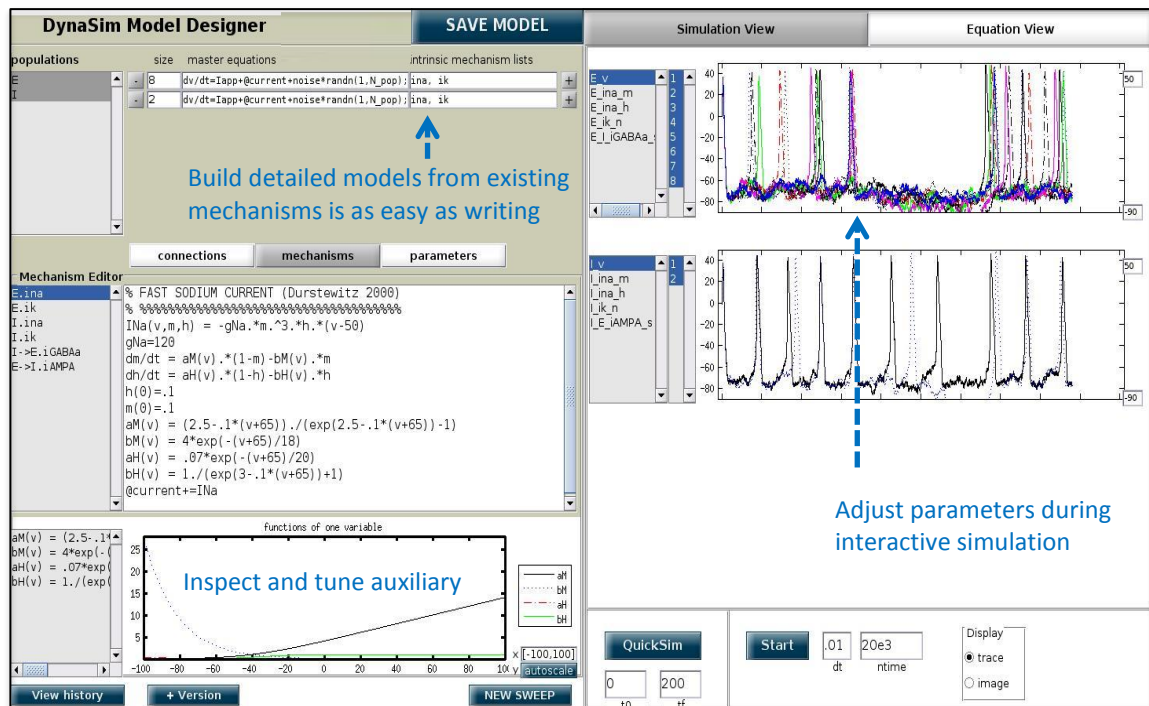
Fig. A.6. DynaSim Graphical User Interface showing the weak PING model.

A special feature of the DynaSim GUI is the ability to interactively modify a model during ongoing simulation and to observe the effects without needing to restart the simulation. This feature is useful for interactively exploring models and manually tuning model parameters. It is enabled by storing the model in an updatable anonymous function that is evaluated at each time step. No other simulator to our knowledge offers this feature.

DynaSim GUI is especially useful as a teaching tool and for researchers without programming experience. Researchers who prefer writing code may still find it useful for prototyping before honing in on a model to investigate further in Matlab scripts using functions of the DynaSim toolbox.

Technical details

Modeling

Models can be specified by the user with a cell array of strings (Examples 1-2), a single string (Example 3), or a `specification` structure (Example 4), based on a combination of master equations (using standard mathematical notation and built-in Matlab functions) and optional model objects from an existing library (Examples 3-4). This provides the user with multiple ways of specifying a model depending on the complexity of the model and the level of mathematical detail the user wishes to provide. Internally, DynaSim converts user-supplied information into a standardized high-level `specification` structure, which is subsequently converted into a lower-level `model` structure. The `model` structure is then used to automatically generate a suitable

implementation (m-file, mex-file, or function handle) based on the desired simulation method. The results of simulation are returned in a DynaSim `data` structure. Simulation in DynaSim always involves sequential processing of the following DynaSim structures:

user specification → standardized specification → model → data
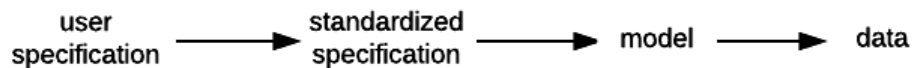
Model objects for populations and mechanisms. Equations define parameters, variables, functions, and ODEs. Model objects are ways of grouping equations to facilitate the rapid construction of larger models. There are two types of objects: populations and mechanisms. Populations represent discrete systems of interest like compartments (e.g., soma, dendrite), cells, or populations of cells. Mechanisms represent smaller-scale components that affect the dynamics of populations (e.g., ion currents); they are called intrinsic mechanisms when they depend only on the state of the population they affect (e.g., sodium and potassium currents), and they are called connection mechanisms when they depend additionally on the state of other populations (e.g., inter-compartmental and synaptic currents). DynaSim comes prepackaged with a library of common model objects. Each object is assigned a unique name to enable the duplication of parameter, variable, and function names in different objects. The same intrinsic mechanism can be reused in different populations, and the same connection mechanism can be reused to connect different pairs of populations. Thus, mechanism objects enable equations to be specified once and reused an arbitrary number of times, and both types of

objects enable equations to be specified without requiring the tedious assignment of unique variable/function names each time the same equations appear in a model.
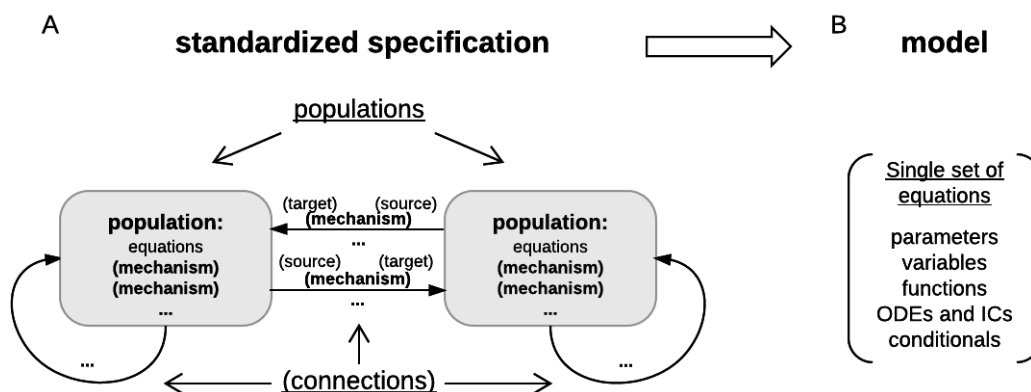
Fig. A.7. Object-based architecture, standardized specification, and DynaSim models.
(A) Object-based architecture and standardized specification. Discrete model objects (populations and mechanisms) are shown in bold; any object can be stored independently in the library and reused as components of larger models. There is no limit on the number of objects in a DynaSim model. Fields of the standardized specification structure are underlined. Each population can have a list of intrinsic mechanisms; each directed pair of source→target populations can have a list of connection mechanisms. Optional objects are enclosed in parentheses. A string-based specification will be internally associated with a default population "pop1" in the standardized specification structure. (B) The standardized specification structure and model objects are parsed to generate a single set of equations describing the full model given the separate sets of equations for each object.

DynaSim structures for higher-level specification, lower-level model definition, and simulated data. Specifiers for the higher-level, more abstract model `specification` structure are grouped into `populations` (each including a `name`, `size`, master `equations`, optional intrinsic `mechanism list`, and `parameters`) and `connections` between populations (each including a `direction`, connection `mechanism list`, and `parameters`) (Fig. A.7A). Connectivity between

populations is specified using connectivity matrices defined in connection mechanisms between presynaptic source and postsynaptic target populations. Models specified by the user with strings are always associated internally with a population (named "pop1" by default). Model specification is divided into `populations` and `connections` to facilitate network modeling. However, a population of multi-compartment neurons can be implemented by specifying different compartments using the `populations` field and connecting them, for instance, using `connections` with the ohmic axial current mechanism from the DynaSim library and an identity connectivity matrix.

The lower-level, more detailed **model** definition structure includes a single set of model elements: `parameters` (scalars, strings), `fixed variables` (matrices and scalar expressions), `functions` (of time and state variables), and `ODEs/ICs` describing system dynamics (i.e., the evolution of state variables over time) (Fig. A.7B). Model elements are always assigned unique names in the lower-level `model` structure by prepending an object-specific namespace identifier (e.g., "pop1_" for population object "pop1"; "pop1_Na_" for mechanism object "Na" in population "pop1") to the reusable names given in the object definition (e.g., "pop1_V" for state variable "V" in population "pop1"; "pop1_Na_m" for state variable "m" in mechanism "Na"). The same unique state variable and function names are used in the output **data** structure storing the results of simulation.

Linking equations across model objects. Once namespace identifiers are used to assign unique names to all parameters, variables, and functions, then the equations from lower-level mechanisms need to be combined with the equations from higher-level

populations and other lower-level mechanisms belonging to the same population. This is trivial for ODEs but requires something extra to indicate how mechanism functions affect the dynamics of population state variables defined outside the mechanism; for instance, how the sodium current "INa," defined in mechanism "Na," affects the voltage "V" of population "pop1". Linking objects can be a difficult concept to grasp at first, and understanding it is not necessary to use DynaSim; however, it does become more intuitive with use.

Linking mechanism elements (functions or variables) to equations defined in other objects is achieved by performing substitution guided by "linkers". A linker is a string that appears in two objects; in one object (e.g., population "pop1") it is a placeholder indicating the location in an equation (e.g., ODE "dV/dt") where an element of a different object (e.g., function "INa") should be inserted; in the second object (e.g., mechanism "Na") it indicates the element (e.g., function "INa") to be inserted into the first object. For instance, the linker "@current" can be used in population-level dynamics "dV/dt=@current" along with the mechanism-level linker statement "@current += INa" to direct DynaSim to perform addition assignment, after prepending namespace identifiers, resulting in "d(pop1_V)/dt=@current+pop1_Na_INa". Compound assignment operators (e.g., "+=" and "-=") enable the same linker to be used in multiple mechanisms; for instance, "@current+=INa" in mechanism "Na" and "@current+=”IK" in mechanism "K" would produce "d(pop1_V)/dt=@current+pop1_Na_INa +pop1_K_IK". All linkers are removed from the resulting ODE system before simulation; e.g., producing the desired final ODE "d(pop1_V)/dt=pop1_Na_INa+pop1_K_IK". The online

documentation explains how to increase modularization by linking objects with mismatched linker identifiers (e.g., "@Currents" in "dV/dt" and "@current" in "Na").

Intrinsic Mechanisms (ina, ik)

```
ina={
    'INa(v,m,h) = -gNa.*m.^3.*h.*(v-50) ; gNa=120';
    'dm/dt = aM(v).*(1-m)-bM(v).*m; m(0)=.1';
    'dh/dt = aH(v).*(1-h)-bH(v).*h; h(0)=.1';
    'aM(v) = (2.5-.1*(v+65))./(exp(2.5-.1*(v+65))-1)';
    'bM(v) = 4*exp(-(v+65)/18)';
    'aH(v) = .07*exp(-(v+65)/20)';
    'bH(v) = 1./(exp(3-.1*(v+65))+1)';
     '@current+=INa';
  };
```

```
ik={
    'IK(v,n) = -gK.*n.^4.*(v+77); gK=36';
    'dn/dt = aN(v).*(1-n)-bN(v).*n; n(0)=0';
    'aN(v) = (.1-.01*(v+65))./(exp(1-.1*(v+65))-1)';
    'bN(v) = .125*exp(-(v+65)/80)';
     '@current+=IK';
  };
```

Populations (E, I)

```
master_equations='dv/dt=Iapp+@current+randn(1,N_pop); {ina,ik}';

s.populations(1).name='E';
s.populations(1).size=80;
s.populations(1).equations=master_equations;
s.populations(2).name='I';
s.populations(2).size=20;
s.populations(2).equations=master_equations;
s.connections(1).direction='I->E';
s.connections(1).mechanism_list={'iGABAa'};
s.connections(2).direction='E->I';
s.connections(2).mechanism_list={'iAMPA'};
s.mechanisms(1).name='ina';
s.mechanisms(1).equations=ina;
s.mechanisms(2).name='ik';
s.mechanisms(2).equations=ik;
data=SimulateModel(s);
```

Fig. A.8. Linking equations across population and mechanism objects.
Mechanism linker statements with addition assignment (e.g., @current+=IK) direct DynaSim to substitute functions INa and IK into population-level dynamics "dv/dt," where the linker appears (i.e., @current). In this example, intrinsic mechanisms are defined in script and added to `specification` structure in a `mechanisms` field.

Linking objects is the most unconventional aspect of modeling in DynaSim, and it enables the flexible, modular construction of arbitrary dynamical systems, not only neural models. Fortunately, in practice, it is not necessary to understand linkers to build models in DynaSim when working with existing objects from the library. For instance, "@current+=" is used in all prepackaged ionic mechanisms; thus, for conductance-based neural models, users only need to list the ionic mechanisms they wish to include in a population or connection between populations with suitable dynamics. Additional mechanisms can be flexibly added or removed simply by updating the appropriate mechanism list without being concerned with linkers. This frees the modeler to focus on the mechanisms that are most relevant for their models and the parameters of those mechanisms.

Simulation batches. Simulation batches are sets of simulations that systematically vary some aspect of a base model; each simulation in a batch involves some set of modifications to the base model. More precisely, `modifications` are ways of modifying specifiers (most commonly parameter values) in the base model's high-level `specification`. Simulation batches are specified using the SimulateModel `vary` option, which is expanded into a set of `modifications` for each simulation (see Example 4 and the tutorial for additional details). A "study" in DynaSim is a processing chain that includes a simulation batch plus downstream analysis and visualization.

Simulation

Models are simulated in DynaSim by passing the user's model specification to the `SimulateModel` function along with options specifying details of the simulation. `SimulateModel` provides options to control the solver and machine(s) used for numerical integration, the location of outputs, and the details of batch simulation. Depending on the options specified, `SimulateModel` automates the construction of the full system of equations, as described above, and the generation of Matlab functions that perform the numerical integration. DynaSim supports custom fixed-step integration (Euler, 2nd-order Runge-Kutta, and 4th-order Runge-Kutta) as well as Matlab's built-in variable-step solvers (e.g., ode23, ode45). The integration method is specified by the `solver` option. When fixed-step simulation is desired, DynaSim generates and executes an m-file that explicitly integrates the system of equations using the desired method. When built-in solvers are used, DynaSim generates an m-file with the appropriate format and passes it as a function handle to the desired built-in Matlab function. All m-files generated are saved by default and available for examination and re-use.

A common criticism of simulating computationally intensive models in Matlab is the time required for simulation. An important method of increasing the simulation speed is available for users with the Matlab Coder toolbox. When available, the `compile_flag` option can be used to instruct `SimulateModel` to compile the automatically-generated m-file into a mex-file. Depending on model details, simulating models using compiled mex-files reduces simulation time by a factor of 10x to 100x.

Fig. A.9. Single simulation workflow.
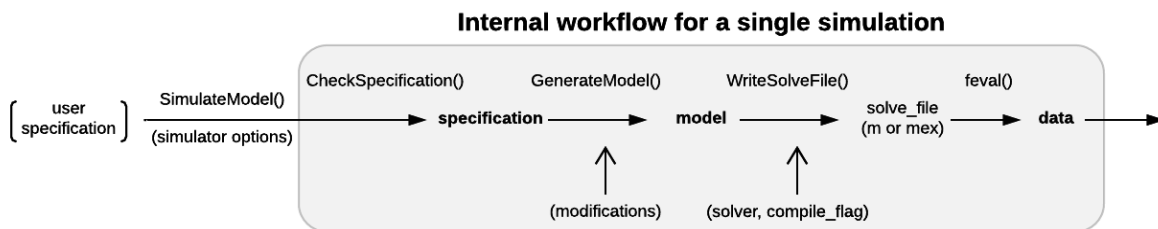
From the user perspective, the functional interface to DynaSim involves specifying a model using strings or a DynaSim `specification` structure, passing it to `SimulateModel`, and obtaining a DynaSim `data` structure with the results of simulation. Internally, `SimulateModel` standardizes the supplied specification using the `CheckSpecification` function. The standardized `specification` structure is converted into a DynaSim `model` structure (Fig. A.7) using the `GenerateModel` function, which prepends object-specific namespace identifiers and links variables and functions across model objects (Fig. A.8). A `solve_file` for numerical integration is automatically generated from the `model` structure by `GetSolveFile` according to simulator options. Simulated data is then obtained by evaluating the `solve_file`. DynaSim structures are shown in bold. Functions are followed by "()". Simulator options are enclosed in parentheses.

Batch management

One advantage of DynaSim over other neural simulators is its extensive support for conducting sets of simulations (i.e., simulation batches). In practice, one is often interested in how behavior changes as some aspect of a model is varied. To facilitate model exploration, DynaSim offers (1) a compact specification of the parameter space to explore, (2) the ability to perform multiple simulations in parallel on different cores of a single machine (using the Parallel Computing toolbox) and different nodes of a compute cluster (using automated job creation and the "qsub" command), (3) functions for analysis and visualization of how behavior varies over parameter space, and (4) automated management of large sets of simulation results. See the tutorial below and online documentation referenced in the DynaSim resources section for details.

Limitations and future directions

At present, DynaSim has two important limitations compared to other simulators: (1) it does not manage physical units, thus making users responsible for ensuring consistency, and (2) it does not provide an explicit spatial representation for model objects, although workarounds exist. These features will be added in future versions of DynaSim. Still, DynaSim is tailored for network modeling more than modeling morphologically complex neurons with many compartments; for instance, it was designed using the name "populations" instead of "compartments" for the `specification` structure field storing information on the sub-systems of interest. Thus, even with explicit spatial representation, simulators like NEURON will remain a better option for modeling morphologically complex neurons.

The ability to export DynaSim models for exploration and further development in other simulators outside of Matlab is under active development. It will be possible to export DynaSim models for further development if evolving models become hindered by limitations of DynaSim. At present, DynaSim models can be exported to XPP, and DynaSim mechanisms can be converted into NEURON MODL files via NeuroML. Further integration with NeuroML will enable converting DynaSim models for simulation in Brian and web-based simulation using Geppeto via Open Source Brain. Support for parameter estimation using data-driven optimization techniques (genetic algorithms and particle filtering) is also under development.

Web-based model repository (InfiniteBrain.org)

Beyond DynaSim, I created a web-based, crowd-sourced model repository, InfiniteBrain.org (Fig. A.10), coupled directly to DynaSim, facilitating collaborative model building. Models created in DynaSim can be uploaded to InfiniteBrain by DynaSim users with InfiniteBrain User accounts. Models derived from earlier models are related in the InfiniteBrain database, enabling the evolution of models to be tracked over time. Fig. A.11 shows the relational structure of entities in the InfiniteBrain database. DynaSim uses database connectors from the Matlab Database toolbox to download models, enabling automated generation of new models from combinations of models stored locally and in the InfiniteBrain repository.

Fig. A.10. Browsing existing models using InfiniteBrain.org.
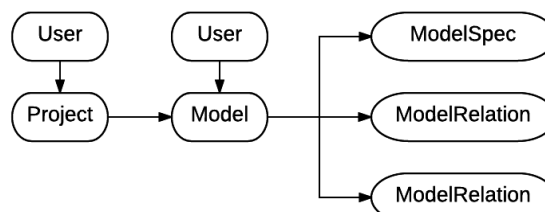
Fig. A.11. InfiniteBrain database entities.

Growing the DynaSim community

I have taken several steps to begin introducing DynaSim to the larger modeling community and to ensure its long-term success: I demonstrated DynaSim for users at the International Neuroinformatics Coordinating Facility (INCF) booth at Society for Neuroscience conference (2015) and for developers at the Janelia Research Campus workshop on Collaborative Development of Data-Driven Models of Neural Systems (2016); I also presented it to MathWorks representatives who have since promoted it at Cosyne (2017) and have plans to feature it on the MathWorks website. I have established a core team of developers to facilitate future developments and building a community of users. All code, documentation, and future developments can be found in the GitHub repository. DynaSim is open-source and licensed under the MIT License. Conversations regarding DynaSim can be followed in the public user mailing list. Articles by MathWorks that feature DynaSim will be linked to the File Exchange. See the Online Resources section below for more details.

Online Resources

DynaSim models for cognitive rhythms

All models in this dissertation were implemented in DynaSim. Equations for cell models can be found in Appendix B. Details on network architecture can be found in the Methods sections of Chapters 2 and 3. Implementation details can be found in the GitHub repositories listed below.

LPFC Network Model (Chapter 2):

https://github.com/jsherfey/PFC_models

ACC Network Model (Chapter 3):

https://github.com/jsherfey/ACd_model

DynaSim community resources

DynaSim GitHub repository:

https://github.com/DynaSim/DynaSim

DynaSim toolbox in the MathWorks File Exchange:

https://www.mathworks.com/matlabcentral/fileexchange/61700-dynasim-dynasim

DynaSim User Mailing List:

https://groups.google.com/forum/#!forum/dynasim-users

InfiniteBrain model repository:

http://infinitebrain.org

DynaSim Tutorial

The following is a Matlab-compatible script that demonstrates the core functionality and

power of the DynaSim toolbox. See the DynaSim documentation available on GitHub for

more demos and details: https://github.com/DynaSim/DynaSim.

```matlab
% %%%%%%%%%%%%%%%%%%%%%%%%%%%%%%%%%%%%%%%%%%%%%%%%%%%%%%%%%%%%%%%%%%%%%%%%%%
%% DynaSim Tutorial
%%%%%%%%%%%%%%%%%%%%%%%%%%%%%%%%%%%%%%%%%%%%%%%%%%%%%%%%%%%%%%%%%%%%%%%%%
%{
Download the DynaSim toolbox from https://github.com/dynasim/dynasim.
  or, download using git: git clone https://github.com/dynasim/dynasim.git
For further documentation, see tutorial.m in the demos directory.
Sign up for user mailing list at:
https://groups.google.com/forum/#!forum/dynasim-users.
Tip: In Matlab, you can obtain more information associated with any function
"FUNCTION_NAME" by entering "help FUNCTION_NAME" in the command window. Use the
"See also" list at the end of the help section to browse through related help
documentation.
%}

% Set path to your copy of the DynaSim toolbox
dynasim_path = 'path/to/dynasim';

% add DynaSim toolbox to Matlab path
addpath(genpath(dynasim_path)); % comment this out if already in path

% Set where to save outputs
output_directory = fullfile(demos_path, 'outputs');
% move to root directory where outputs will be saved
cd(output_directory);

% Here we go!

% %%%%%%%%%%%%%%%%%%%%%%%%%%%%%%%%%%%%%%%%%%%%%%%%%%%%%%%%%%%%%%%%%%%%%%%%%%%%
%% DEFINING AND SIMULATING MODELS
% %%%%%%%%%%%%%%%%%%%%%%%%%%%%%%%%%%%%%%%%%%%%%%%%%%%%%%%%%%%%%%%%%%%%%%%%%%%%

%% Lorenz equations with phase plot

% DynaSim makes it easy to simulate arbitrary systems of ordinary
% differential equations. Simply write out the system in a cell array of
% strings, separating equations into different strings or the same string
% separated by semicolons.

eqns={
  's=10; r=27; b=2.666';
  'dx/dt=s*(y-x)';
  'dy/dt=r*x-y-x*z';
  'dz/dt=-b*z+x*y';
};
```

```
data=SimulateModel(eqns,'tspan',[0 100],'ic',[1 2 .5],'solver','rk4');
% tspan: time limits on integration [ms]
% ic: initial conditions
% solver: numerical method to use (default: rk4 = "4th-order Runge-Kutta")

% All models are numerically integrated using a DynaSim solver function
% created uniquely for a given model and stored in a directory named
% "solve". The file that solves the system (i.e,. numerically integrates
% it) is stored in data.simulator_options and can be viewed or rerun:
edit(data.simulator_options.solve_file)

% Every component of the model is assigned to a "population", and the
% population name (default: 'pop1') is prepended to all variable and
% function names.

% Simulated data can be easily plotted using the resulting data structure:
figure; plot(data.pop1_x,data.pop1_z);
title('Lorenz equations'); xlabel('x'); ylabel('z')

%% Izhikevich neuron with noisy drive
% (reference: p274 of "Dynamical Systems in Neuroscience" by Izhikevich)

% The DynaSim data structure always contains the model state variables,
% time vector, and a copy of the DynaSim model structure that was
% simulated. Additionally, functions can be recorded and returned in the
% DynaSim data structure if indicated using the "monitor" keyword.
% Syntax: monitor FUNCTION

eqns={
  'C=100; vr=-60; vt=-40; k=.7; Iapp=70; ton=200; toff=800';
  'a=.03; b=-2; c=-50; d=100; vpeak=35';
  'dv/dt=(k*(v-vr)*(v-vt)-u+I(t))/C; v(0)=vr';
  'du/dt=a*(b*(v-vr)-u); u(0)=0';
  'if(v>vpeak)(v=c; u=u+d)';
  'I(t)=Iapp*(t>ton&t<toff)*(1+.5*rand)'; % define applied input
  'monitor I';                            % indicate to store applied input
};
% note: applied input uses the reserved variable 't' for time

data=SimulateModel(eqns,'tspan',[0 1000]);

% plot the simulated voltage and monitored input function
figure;
subplot(2,1,1); plot(data.time,data.pop1_v); % plot voltage
xlabel('time (ms)'); ylabel('v'); title('Izhikevich neuron')
subplot(2,1,2); plot(data.time,data.pop1_I); % plot input function
xlabel('time (ms)'); ylabel('Iapp');

% note: "t", "dt", and "T" are special variables that can be used in model
% equations. "t" represents the current time point of the simulation.
% "dt" is the fixed time step used for numeric integration. "T" is the full
% simulated time vector defined before simulation begins.

% %%%%%%%%%%%%%%%%%%%%%%%%%%%%%%%%%%%%%%%%%%%%%%%%%%%%%%%%%%%%%%%%%%%%%%%%%%%
%% RUNNING SETS OF SIMULATIONS
% %%%%%%%%%%%%%%%%%%%%%%%%%%%%%%%%%%%%%%%%%%%%%%%%%%%%%%%%%%%%%%%%%%%%%%%%%%%

% 'vary' indicates the variable to vary, the values it should take, and the
% object (population or connection) whose variable should be varied.
```

```
% Syntax 1: vary={{object, variable, value1},{object, variable, value2},...}
%   - this is useful for simulating an arbitrary set of parameter values
% Syntax 2: vary={object, variable, values; ...}
%   - this is useful for varying parameters systematically (described later)

% Izhikevich study of neuro-computational properties (using Syntax 1)
% based on: http://www.izhikevich.org/publications/izhikevich.m
eqns={
  'a=.02; b=.2; c=-65; d=6; I=14';
  'dv/dt=.04*v^2+5*v+140-u+I; v(0)=-70';
  'du/dt=a*(b*v-u); u(0)=-20';
  'if(v>=30)(v=c;u=u+d)';
  };
P='pop1'; % name of population
vary={
  {P,'a',.02; P,'b',.2 ; P,'c',-50; P,'d',2;  P,'I',15} % tonic bursting
  {P,'a',.01; P,'b',.2 ; P,'c',-65; P,'d',8;  P,'I',30} % spike freq adaptation
  {P,'a',.02; P,'b',.2 ; P,'c',-65; P,'d',6;  P,'I',7}  % spike latency
  {P,'a',.03; P,'b',.25; P,'c',-52; P,'d',0;  P,'I',0}  % rebound burst
  {P,'a',1;   P,'b',1.5; P,'c',-60; P,'d',0;  P,'I',-65}% bistability
  {P,'a',.02; P,'b',1  ; P,'c',-55; P,'d',4;  P,'I',1}  % accomodation
  {P,'a',-.02;P,'b',-1 ; P,'c',-60; P,'d',8;  P,'I',80} % inhib-induced spiking
  {P,'a',-.026;P,'b',-1; P,'c',-45; P,'d',0;  P,'I',70} % inhib-induced bursts
  };
data=SimulateModel(eqns,'tspan',[0 250],'vary',vary);
PlotData(data);

% %%%%%%%%%%%%%%%%%%%%%%%%%%%%%%%%%%%%%%%%%%%%%%%%%%%%%%%%%%%%%%%%%%%%%%%%%%%%%
%% QUICKLY BUILDING LARGE MODELS FROM EXISTING "MECHANISMS"
% %%%%%%%%%%%%%%%%%%%%%%%%%%%%%%%%%%%%%%%%%%%%%%%%%%%%%%%%%%%%%%%%%%%%%%%%%%%%%

% Mechanisms are predefined reusable sub-models meant to be incorporated
% in larger complete models. Examples of mechanisms in neuron models include
% ion currents, pumps, etc. Once defined, they can be easily incorporated
% into larger models by simply listing the name of the file containing their
% equations, without the need to re-write any of the mechanism equations.
% This greatly simplifies large model prototyping and re-configuration.

% Hodgkin-Huxley neuron equations (without predefined mechanisms)
eqns={
  'gNa=120; gK=36; Cm=1';
  'INa(v,m,h) = gNa.*m.^3.*h.*(v-50)';
  'IK(v,n) = gK.*n.^4.*(v+77)';
  'dv/dt = (10-INa(v,m,h)-IK(v,n))/Cm; v(0)=-65';
  'dm/dt = aM(v).*(1-m)-bM(v).*m; m(0)=.1';
  'dh/dt = aH(v).*(1-h)-bH(v).*h; h(0)=.1';
  'dn/dt = aN(v).*(1-n)-bN(v).*n; n(0)=0';
  'aM(v) = (2.5-.1*(v+65))./(exp(2.5-.1*(v+65))-1)';
  'bM(v) = 4*exp(-(v+65)/18)';
  'aH(v) = .07*exp(-(v+65)/20)';
  'bH(v) = 1./(exp(3-.1*(v+65))+1)';
  'aN(v) = (.1-.01*(v+65))./(exp(1-.1*(v+65))-1)';
  'bN(v) = .125*exp(-(v+65)/80)';
};
data=SimulateModel(eqns);
figure; plot(data.time,data.(data.labels{1}))
xlabel('time (ms)'); ylabel('membrane potential (mV)');
title('Hodgkin-Huxley neuron')
```

```
% Equivalent Hodgkin-Huxley neuron with predefined mechanisms
data=SimulateModel('dv/dt=10+@current/Cm; Cm=1; v(0)=-65; {iNa,iK}');
figure; plot(data.time,data.(data.labels{1}))
xlabel('time (ms)'); ylabel('membrane potential (mV)');
title('Hodgkin-Huxley neuron')

% View the mechanism files:
[~,eqnfile]=LocateModelFiles('iNa.mech'); edit(eqnfile{1});
[~,eqnfile]=LocateModelFiles('iK.mech');  edit(eqnfile{1});
% Mechanisms can be custom built; however, DynaSim does come pakaged with
% some common ones like popular ion currents (see <dynasim>/models).

% Example of a bursting neuron model using three active current mechanisms:
eqns='dv/dt=5+@current; {iNaF,iKDR,iM}; gNaF=100; gKDR=5; gM=1.5; v(0)=-70';
data=SimulateModel(eqns,'tspan',[0 200]);
figure; plot(data.time,data.(data.labels{1}))
xlabel('time (ms)'); ylabel('membrane potential (mV)');
title('Intrinsically Bursting neuron')

% %%%%%%%%%%%%%%%%%%%%%%%%%%%%%%%%%%%%%%%%%%%%%%%%%%%%%%%%%%%%%%%%%%%%%%
%% BUILDING LARGE MODELS WITH MULTIPLE POPULATIONS AND CONNECTIONS
% %%%%%%%%%%%%%%%%%%%%%%%%%%%%%%%%%%%%%%%%%%%%%%%%%%%%%%%%%%%%%%%%%%%%%%

%% Sparse Pyramidal-Interneuron-Network-Gamma (sPING)

% define equations of cell model (same for E and I populations)
eqns={
  'dv/dt=Iapp+@current+noise*randn(1,N_pop)';
  'monitor iGABAa.functions, iAMPA.functions'
};
% Tip: monitor all functions of a mechanism using: monitor MECHANISM.functions

% create DynaSim specification structure
s=[];
s.populations(1).name='E';
s.populations(1).size=80;
s.populations(1).equations=eqns;
s.populations(1).mechanism_list={'iNa','iK'};
s.populations(1).parameters={'Iapp',5,'gNa',120,'gK',36,'noise',40};
s.populations(2).name='I';
s.populations(2).size=20;
s.populations(2).equations=eqns;
s.populations(2).mechanism_list={'iNa','iK'};
s.populations(2).parameters={'Iapp',0,'gNa',120,'gK',36,'noise',40};
s.connections(1).direction='I->E';
s.connections(1).mechanism_list={'iGABAa'};
s.connections(1).parameters={'tauD',10,'gSYN',.1,'netcon','ones(N_pre,N_post)'}
s.connections(2).direction='E->I';
s.connections(2).mechanism_list={'iAMPA'};
s.connections(2).parameters={'tauD',2,'gSYN',.1,'netcon',ones(80,20)};
data=SimulateModel(s);
PlotData(data);
PlotData(data,'variable',{'E_v','E_I_iGABAa_ISYN'});

% View the connection mechanism file:
[~,eqnfile]=LocateModelFiles('iAMPA.mech'); edit(eqnfile{1});

% %%%%%%%%%%%%%%%%%%%%%%%%%%%%%%%%%%%%%%%%%%%%%%%%%%%%%%%%%%%%%%%%%%%%%%%%%
%% SAVING SIMULATED DATA
% %%%%%%%%%%%%%%%%%%%%%%%%%%%%%%%%%%%%%%%%%%%%%%%%%%%%%%%%%%%%%%%%%%%%%%%%%
```

```
% How to: set 'save_data_flag' to 1
% optionally: set 'study_dir' to /path/to/outputs

%% Save data from a single simulation
% Example using the previous sPING model:
data=SimulateModel(s,'save_data_flag',1,'study_dir','demo_sPING_1');

%% Save data from a set of simulations

% Specify what to vary
% Tip: use 'vary' Syntax 2 to systematically vary a parameter
vary={'E','Iapp',[0 10 20]}; % vary the amplitude of tonic input to E-cells
data=SimulateModel(s,'save_data_flag',1,'study_dir','demo_sPING_2',...
                   'vary',vary);

% load and plot the saved data
data_from_disk = ImportData('demo_sPING_2');
PlotData(data_from_disk);
PlotData(data_from_disk,'variable','E_v');

% Vary a connection parameter
vary={'I->E','tauD',[5 10 15]}; % inhibition decay time constant from I to E

% Vary two parameters (run a simulation for all combinations of values)
vary={
  'E'   ,'Iapp',[0 10 20];      % amplitude of tonic input to E-cells
  'I->E','tauD',[5 10 15]       % inhibition decay time constant from I to E
  };
SimulateModel(s,'save_data_flag',1,'study_dir','demo_sPING_3',...
              'vary',vary,'verbose_flag',1);
data=ImportData('demo_sPING_3');
PlotData(data);
PlotData(data,'plot_type','rastergram');
PlotData(data,'plot_type','power');
PlotFR(data); % examine how mean firing rate changes with Iapp and tauD

% %%%%%%%%%%%%%%%%%%%%%%%%%%%%%%%%%%%%%%%%%%%%%%%%%%%%%%%%%%%%%%%%%%%%%%%%%
%% RUNNING SIMULATIONS ON THE CLUSTER
% %%%%%%%%%%%%%%%%%%%%%%%%%%%%%%%%%%%%%%%%%%%%%%%%%%%%%%%%%%%%%%%%%%%%%%%%%
% How to: set 'cluster_flag' to 1
% Requirement: you must be logged on to a cluster that recognizes 'qsub'

% Run three simulations in parallel jobs and save the simulated data
eqns='dv/dt=@current+I; {iNa,iK}';
vary={'','I',[0 10 20]};
SimulateModel(eqns,'save_data_flag',1,'study_dir','demo_cluster_1',...
  'vary',vary,'cluster_flag',1,'overwrite_flag',1,'verbose_flag',1);

% tips for checking job status:
% !qstat -u <YOUR_USERNAME>
% !cat ~/batchdirs/demo_cluster_1/pbsout/sim_job1.out
data=ImportData('demo_cluster_1');
PlotData(data);

% Repeat but also save plotted data
eqns='dv/dt=@current+I; {iNa,iK}';
vary={'','I',[0 10 20]};
SimulateModel(eqns,'save_data_flag',1,'study_dir','demo_cluster_2',...
  'vary',vary,'cluster_flag',1,'overwrite_flag',1,'verbose_flag',1,...
  'plot_functions',@PlotData);
```

```
% Save multiple plots and pass custom options to each plotting function
eqns='dv/dt=@current+I; {iNa,iK}';
vary={'','I',[0 10 20]};
SimulateModel(eqns,'save_data_flag',1,'study_dir','demo_cluster_3',...
  'vary',vary,'cluster_flag',1,'overwrite_flag',1,'verbose_flag',1,...
  'plot_functions',{@PlotData,@PlotData},...
  'plot_options',{{},{'plot_type','power'}});
% !cat ~/batchdirs/demo_cluster_3/pbsout/sim_job1.out

% Post-simulation analyses can be performed similarly by passing
% analysis function handles and options using 'analysis_functions' and
% 'analysis_options'.

% Note: options will be passed to plot and analysis functions in the order
% given. You can pass handles and options for any built-in, pre-packaged,
% or custom functions.

% %%%%%%%%%%%%%%%%%%%%%%%%%%%%%%%%%%%%%%%%%%%%%%%%%%%%%%%%%%%%%%%%%%%%%%%%%%
%% SPEEDING UP SIMULATION USING THE MATLAB C++ COMPILER
% %%%%%%%%%%%%%%%%%%%%%%%%%%%%%%%%%%%%%%%%%%%%%%%%%%%%%%%%%%%%%%%%%%%%%%%%%%

% Simulating large models can be sped up significantly by compiling the
% simulation before running it. DynaSim makes this easy to do using the
% 'compile_flag' option in SimulateModel. Note: compiling the model can
% take several seconds to minutes; however, it only compiles the first time
% it is run and is significantly faster on subsequent runs.

data=SimulateModel(s,'compile_flag',1);
PlotData(data);

% Now run again:
data=SimulateModel(s,'compile_flag',1);
PlotData(data);
```

APPENDIX B: Model Equations

Deep layer LPFC model

DynaSim implementation

https://github.com/jsherfey/PFC_models

Equations

The deep layer LPFC model consists of principal cells (PCs) and fast spiking interneurons (FS INs) with cell models taken from Durstewitz et al. (2000) and modifications from Durstewitz and Seamans (2002). The original cell models and my modifications to them will be summarized here; network descriptions are given in the Methods section of Chapter 2. See the referenced publications and DynaSim code for more details.

Each cell had voltage dynamics given by $C_m \frac{dV}{dt} = -I_{inp}(t,V) - \sum I_{int} - \sum I_{syn}$. Compartment dimensions and maximal conductance of intrinsic ion channels for PC and FS INs are given in Table 3. The dynamics of ion channel gating variable, *x*, is governed by $\frac{dx}{dt} = \frac{x_\infty(V) - x}{\tau_x(V)}$ where $x_\infty(V)$ is the voltage-dependent steady-state and $\tau_x(V)$ is the voltage-dependent time constant. The kinetics associated with each gating variable is given in Table 4.

Each PC compartment had intrinsic ion channels yielding voltage dynamics governed by

$$C_m \frac{dV}{dt} = -I_{inp}(t,V) - I_{NaF} - I_{NaP} - I_{Ca} - I_{KDR} - I_{Ks} - I_{KCa} - I_{leak} - \sum I_{syn} ,$$

$$C_m \frac{dV}{dt} = -I_{inp}(t,V) - g_{NaF}m^3h(V - E_{Na}) - g_{NaP}mh(V - E_{Na}) - g_{Ca}u^2v(V -$$

$$E_{Ca}) - g_{KDR}n^4(V - E_K) - g_{Ks}ab(V - E_K) - g_{KCa}c^2(V - E_K) - I_{leak} - \sum I_{syn}$$

with E_K and E_{Ca} calculated using the Nernst equation, and E_{Na}=55mV.

FS INs had intrinsic ion channels yielding voltage dynamics governed by:

$$C_m \frac{dV}{dt} = -I_{inp}(t,V) - I_{NaF} - I_{KDR} - I_{leak} - \sum I_{syn}$$

$$= -I_{inp}(t,V) - g_{NaF}m^3h(V - E_{Na}) - g_{KDR}n^4(V - E_K) - I_{leak} - \sum I_{syn}.$$

	l, μm	d, μm	I_{NaF}	I_{NaP}	I_{Ca}	I_{KDR}	I_{Ks}	I_{KCa}	τ_{Ca}	I_{AR}
PC										
soma	28.618	21.84	117	1.8	.4	50	.08	2.1	250	-
dendrite	650	6.5	20	0.8	.8	14	.08	2.1	120	-
FS IN	42	42	45	-	-	18	-	-	-	-
LTS IN	-	-	200	-	-	5	-	-	-	50

Conductance densities are given in mS/cm². τ_{Ca} calcium decay time constants in ms.

Table 3. Dimensions, conductance, and calcium decay in the LPFC model.

Superficial LPFC model

The superficial LPFC model consisted of PCs, FS INs, and low threshold spiking (LTS) INs. PCs and FS INs were the same as in the deep layer LPFC model. LTS cells correspond to CB+/CR+ interneurons providing inhibition onto PC apical dendrites and FS cells. The LTS model is adapted from Kramer et al. (2008) based on the modifications described below. See section 2.5 for network architecture. Maximal conductances and ion channel kinetics are given in Tables 3 and 4, respectively.

Current	Gate x	α	β	x_∞	τ_x, ms
PC					
I_{NaF}	m^3	$\dfrac{-.2816(V+28)}{-1+e^{-(V+28)/9.3}}$	$\dfrac{.2464(V+1)}{-1+e^{-(V+1)/6}}$	$\alpha/(\alpha+\beta)$	$1/(\alpha+\beta)$
	h	$\dfrac{.098}{e^{(V+43.1)/20}}$	$\dfrac{1}{1+e^{-(V+13.1)/10}}$	$\alpha/(\alpha+\beta)$	$1/(\alpha+\beta)$
I_{NaP}	m	$\dfrac{-.2816(V+12)}{-1+e^{-(V+12)/9.3}}$	$\dfrac{.2464(V-15)}{-1+e^{-(V-15)/6}}$	$\alpha/(\alpha+\beta)$	$1/(\alpha+\beta)$
	h	$\dfrac{2.8*10^{-5}}{e^{(V+42.8477)/4.0248}}$	$\dfrac{.02}{1+e^{-(V-413.9)/148.3}}$	$\alpha/(\alpha+\beta)$	**$.5/(\alpha+\beta)$**
I_{Ca}	u^2	-	-	$\dfrac{1}{1+e^{-(V+24.6)/11.3}}$	$1.25\text{sech}(-.031(V+37.1))$
	v	-	-	$\dfrac{1}{1+e^{(V+12.6)/18.9}}$	140
I_{KDR}	n^4	$\dfrac{-.018(V-13)}{-1+e^{-(V-13)/25}}$	$\dfrac{.0054(V-23)}{-1+e^{-(V-23)/12}}$	$\alpha/(\alpha+\beta)$	$1/(\alpha+\beta)$
I_{Ks}	a	-	-	$\dfrac{1}{1+e^{-(V+34)/6.5}}$	6
	b	-	-	$\dfrac{1}{1+e^{(V+65)/6.6}}$	$200+\dfrac{200}{1+e^{-(V+71.6)/6.85}}$
I_{KCa}	c^2	$\dfrac{-.00642(V_s+18)}{-1+e^{-(V_s+18)/12}}$	$1.7e^{-(V_s+152)/30}$, $V_s=V+40\log_{10}([Ca]_i)$	$\alpha/(\alpha+\beta)$	$1/(\alpha+\beta)$
FS IN					
I_{NaF}	m^3	$\dfrac{-.2816(V+38)}{-1+e^{-(V+38)/9.3}}$	$\dfrac{.2464(V+13)}{-1+e^{-(V+13)/6}}$	$\alpha/(\alpha+\beta)$	$1/(\alpha+\beta)$
	h	$2\dfrac{.098}{e^{(V+53.1)/20}}$	$2\dfrac{1}{1+e^{-(V+23.1)/10}}$	$\alpha/(\alpha+\beta)$	$1/(\alpha+\beta)$
I_{KDR}	n^4	$\dfrac{-.018(V-3)}{-1+e^{-(V-3)/25}}$	$\dfrac{.0054(V-13)}{-1+e^{-(V-13)/12}}$	$\alpha/(\alpha+\beta)$	$1/(\alpha+\beta)$
LTS IN					
I_{NaF}	m_∞^3	-	-	$\dfrac{1}{1+e^{-(V+38)/10}}$	-
	h	-	-	$\dfrac{1}{1+e^{(V+58.3)/6.7}}$	$.225+\dfrac{1.125}{1+e^{-(V+37)/15}}$
I_{KDR}	n^4	-	-	$\dfrac{1}{1+e^{-(V+27)/11.5}}$	$.25+4.35e^{-|V+10|/10}$
I_{AR}	w	-	-	$\dfrac{1}{1+e^{(V+75)/5.5}}$	$\dfrac{1}{e^{-(.086V+15)}+e^{(.07V-1.9)}}$

V, membrane potential (mV); [Ca]$_i$, intracellular calcium concentration (µmol/l).

Table 4. Gating variables for all ion channels in the LPFC model.

LTS INs had intrinsic ion channels yielding voltage dynamics governed by:

$$C_m \frac{dV}{dt} = -I_{inp}(t, V) - I_{NaF} - I_{KDR} - I_{AR} - I_{leak} - \sum I_{syn}$$

$$C_m \frac{dV}{dt} = -I_{inp}(t, V) - g_{NaF} m_\infty(V)^3 h(V - 50) - g_{KDR} n^4(V + 100) - g_{AR} w(V + 35) - 6(V + 65) - \sum I_{syn}$$

Modifications to LTS model based on PFC physiology:

The Kramer model is based on somatosensory association cortex. We adapted the model so that it exhibited electrophysiological properties based on PFC recordings of superficial CB+ interneurons. Specifically, we decreased gKDR by 50% to achieve longer action potential duration (Zaitsev et al., 2009), a resting membrane potential of -64mV (Kawaguchi, 1993; Konstantoudaki et al., 2016), and spike threshold of -52mV (Konstantoudaki et al., 2016).

ACC network model

DynaSim implementation

https://github.com/jsherfey/ACd_model

Equations

The same ion channels in the PFC model were adapted using constraints based on rat ACd data to construct the ACC model as described in the Methods section of Chapter 3. See the DynaSim code for implementation details.

BIBLIOGRAPHY

Ainsworth M, Lee S, Cunningham MO, Roopun AK, Traub RD, Kopell NJ, Whittington MA (2011) Dual gamma rhythm generators control interlaminar synchrony in auditory cortex. *Journal of Neuroscience* 31:17040-17051.

Ainsworth M, Lee S, Cunningham MO, Traub RD, Kopell NJ, Whittington MA (2012) Rates and rhythms: a synergistic view of frequency and temporal coding in neuronal networks. *Neuron* 75:572-583.

Akam T, Kullmann DM (2010) Oscillations and filtering networks support flexible routing of information. *Neuron* 67:308-320.

Akam T, Kullmann DM (2014) Oscillatory multiplexing of population codes for selective communication in the mammalian brain. *Nature Reviews Neuroscience* 15:111-122.

Amari, S. I. (1977). Dynamics of pattern formation in lateral-inhibition type neural fields. *Biological cybernetics*, *27*(2), 77-87.

Amiez, C., Joseph, J. P., & Procyk, E. (2005). Anterior cingulate error-related activity is modulated by predicted reward. *European Journal of Neuroscience*, *21*(12), 3447-3452.

Anver H, Ward PD, Magony A, Vreugdenhil M (2011) NMDA receptor hypofunction phase couples independent gamma-oscillations in the rat visual cortex. *Neuropsychopharmacology* 36:519-528.

Ardid S, Vinck M, Kaping D, Marquez S, Everling S, Womelsdorf T (2015) Mapping of functionally characterized cell classes onto canonical circuit operations in primate prefrontal cortex. *Journal of Neuroscience* 35:2975-2991.

Ashby, F. G., Turner, B. O., & Horvitz, J. C. (2010). Cortical and basal ganglia contributions to habit learning and automaticity. *Trends in Cognitive Sciences*, *14*(5), 208–215.

Atkinson, R. C., & Shiffrin, R. M. (1968). Human memory: A proposed system and its control processes. *Psychology of learning and motivation*, *2*, 89-195.

Baddeley, A. D., & Hitch, G. (1974). Working memory. *Psychology of learning and motivation*, *8*, 47-89.

Barbas, H. (2000). Connections underlying the synthesis of cognition, memory, and emotion in primate prefrontal cortices. *Brain Research Bulletin*, *52*(5), 319–330.

Barbas, H. (2015). General cortical and special prefrontal connections: Principles from structure to function. *Annual review of neuroscience*, *38*, 269-289.

Basar-Eroglu, C., Brand, A., Hildebrandt, H., Karolina Kedzior, K., Mathes, B., & Schmiedt, C. (2007a). Working memory related gamma oscillations in schizophrenia patients. *International Journal of Psychophysiology*, *64*(1), 39–45.

Bassett DS, Bullmore E, Verchinski BA, Mattay VS, Weinberger DR, Meyer-Lindenberg A (2008) Hierarchical organization of human cortical networks in health and schizophrenia. *Journal of Neuroscience* 28:9239-9248.

Bastos AM, Usrey WM, Adams RA, Mangun GR, Fries P, Friston KJ (2012) Canonical microcircuits for predictive coding. *Neuron* 76:695-711.

Bastos AM, Vezoli J, Bosman CA, Schoffelen JM, Oostenveld R, Dowdall JR, De Weerd P, Kennedy H, Fries P (2015) Visual areas exert feedforward and feedback influences through distinct frequency channels. *Neuron* 85:390-401.

Bloem, B., Poorthuis, R. B., & Mansvelder, H. D. (2014). Cholinergic modulation of the medial prefrontal cortex: the role of nicotinic receptors in attention and regulation of neuronal activity. *Frontiers in Neural Circuits*, 8(17).

Börgers, C., Epstein, S., & Kopell, N. J. (2005). Background gamma rhythmicity and attention in cortical local circuits: a computational study. *Proceedings of the National Academy of Sciences of the United States of America*, *102*(19), 7002-7007.

Börgers, C., Epstein, S., & Kopell, N. J. (2008). Gamma oscillations mediate stimulus competition and attentional selection in a cortical network model. *Proceedings of the National Academy of Sciences*, *105*(46), 18023-18028.

Brincat SL, Miller EK (2015) Frequency-specific hippocampal-prefrontal interactions during associative learning. *Nature Neuroscience* 18:576-581.

Brown, J. W., Bullock, D., & Grossberg, S. (2004). How laminar frontal cortex and basal ganglia circuits interact to control planned and reactive saccades. *Neural Networks*, *17*(4), 471-510.

Buschman, T. J., Denovellis, E. L., Diogo, C., Bullock, D., & Miller, E. K. (2012). Synchronous Oscillatory Neural Ensembles for Rules in the Prefrontal Cortex. *Neuron*, *76*(4), 838–846.

Buzsáki, G. (2002). Theta oscillations in the hippocampus. *Neuron*, *33*(3), 325-340.

Cannon J, McCarthy MM, Lee S, Lee J, Borgers C, Whittington MA, Kopell N (2014) Neurosystems: brain rhythms and cognitive processing. *European Journal of Neuroscience* 39:705-719.

Cannon, J., & Kopell, N. (2015). The leaky oscillator: Properties of inhibition-based rhythms revealed through the singular phase response curve. *SIAM Journal on Applied Dynamical Systems*, *14*(4), 1930-1977.

Carr DB, Andrews GD, Glen WB, Lavin A (2007) alpha2-Noradrenergic receptors activation enhances excitability and synaptic integration in rat prefrontal cortex pyramidal neurons via inhibition of HCN currents. *Journal of Physiology* 584:437-450.

Chatham, C. H., Frank, M. J., & Badre, D. (2014). Corticostriatal output gating during selection from working memory. *Neuron*, 81(4), 930-942.

Chatham, C. H., & Badre, D. (2015). Multiple gates on working memory. *Current opinion in behavioral sciences*, 1, 23-31.

Cho, R. Y., Konecky, R. O., & Carter, C. S. (2006). Impairments in frontal cortical γ synchrony and cognitive control in schizophrenia. *Proceedings of the National Academy of Sciences*, *103*(52), 19878–19883.

Colgin, L. L., Denninger, T., Fyhn, M., Hafting, T., Bonnevie, T., Jensen, O., ... & Moser, E. I. (2009). Frequency of gamma oscillations routes flow of information in the hippocampus. *Nature*, *462*(7271), 353-357.

Csicsvari, J., Jamieson, B., Wise, K. D., & Buzsáki, G. (2003). Mechanisms of gamma oscillations in the hippocampus of the behaving rat. *Neuron*, *37*(2), 311-322.

Davies, D. L., & Bouldin, D. W. (1979). A cluster separation measure. *IEEE transactions on pattern analysis and machine intelligence*, (2), 224-227.

Dayan, P. (2007). Bilinearity, Rules, and Prefrontal Cortex. *Frontiers in Computational Neuroscience*, *1*.

Dayan, P. (2008). Simple Substrates for Complex Cognition. *Frontiers in Neuroscience*, *2*(2), 255–263.

de Almeida, L., Idiart, M., & Lisman, J. E. (2009). A second function of gamma frequency oscillations: an E%-max winner-take-all mechanism selects which cells fire. *Journal of Neuroscience*, *29*(23), 7497-7503.

Deco G, Rolls ET (2003) Attention and working memory: a dynamical model of neuronal activity in the prefrontal cortex. *European Journal of Neuroscience* 18:2374-2390.

DeFelipe, J. (1997). Types of neurons, synaptic connections and chemical characteristics of cells immunoreactive for calbindin-D28K, parvalbumin and calretinin in the neocortex. *Journal of chemical neuroanatomy*, *14*(1), 1-19.

Del Castillo, J., & Katz, B. (1954). Quantal components of the end-plate potential. *The Journal of physiology*, *124*(3), 560-573.

Dembrow NC, Chitwood RA, Johnston D (2010) Projection-specific neuromodulation of medial prefrontal cortex neurons. *Journal of Neuroscience* 30:16922-16937.

Dembrow N, Johnston D (2014) Subcircuit-specific neuromodulation in the prefrontal cortex. *Frontiers in Neural Circuits* 8:54.

Dong, Y., & White, F. J. (2003). Dopamine D1-class receptors selectively modulate a slowly inactivating potassium current in rat medial prefrontal cortex pyramidal neurons. *Journal of Neuroscience*, *23*(7), 2686-2695.

Donner TH, Siegel M (2011) A framework for local cortical oscillation patterns. *Trends in Cognitive Science* 15:191-199.

Durstewitz, D., Seamans, J. K., & Sejnowski, T. J. (2000). Neurocomputational models of working memory. *Nature Neuroscience*, *3*, 1184–1191.

Durstewitz, D., & Seamans, J. K. (2002). The computational role of dopamine D1 receptors in working memory. *Neural Networks*, *15*(4), 561-572.

Durstewitz D, Vittoz NM, Floresco SB, Seamans JK (2010) Abrupt transitions between prefrontal neural ensemble states accompany behavioral transitions during rule learning. *Neuron* 66:438-448.

Eeckman, F. H., & Freeman, W. J. (1990). Correlations between unit firing and EEG in the rat olfactory system. *Brain research*, 528(2), 238-244.

Ermentrout, B. (2002). Simulating, analyzing, and animating dynamical systems: a guide to XPPAUT for researchers and students. *Society for Industrial and Applied Mathematics*.

Evans, J. S. B. T. (2003). In two minds: dual-process accounts of reasoning. *Trends in Cognitive Sciences*, *7*(10), 454–459.

Evans, J. S. B. T. (2008). Dual-Processing Accounts of Reasoning, Judgment, and Social Cognition. *Annual Review of Psychology*, *59*(1), 255–278.

Ferrante M, Tahvildari B, Duque A, Hadzipasic M, Salkoff D, Zagha EW, Hasselmo ME, McCormick DA (2016) Distinct Functional Groups Emerge from the Intrinsic

Properties of Molecularly Identified Entorhinal Interneurons and Principal Cells. *Cerebral Cortex*, Epub ahead of print.

Fisahn A, Pike FG, Buhl EH, Paulsen O (1998) Cholinergic induction of network oscillations at 40 Hz in the hippocampus in vitro. *Nature* 394:186-189.

Fisahn A. Kainate receptors and rhythmic activity in neuronal networks: hippocampal gamma oscillations as a tool. *Journal of Physiology* 562: 65-72, 2005.

Frank, M. J., Loughry, B., & O'Reilly, R. C. (2001). Interactions between frontal cortex and basal ganglia in working memory: a computational model. *Cognitive, Affective, & Behavioral Neuroscience*, *1*(2), 137-160.

Frank, M. J., & Badre, D. (2015). How cognitive theory guides neuroscience. *Cognition*, *135*, 14-20.

Freeman, W. J. (1975). *Mass action in the nervous system*. Academic Press.

Freeman, W. J. (1979). Nonlinear gain mediating cortical stimulus-response relations. *Biological Cybernetics*, 33(4), 237-247.

Fries P (2005) A mechanism for cognitive dynamics: neuronal communication through neuronal coherence. *Trends in Cognitive Science* 9:474-480.

Funahashi, S., Bruce, C. J., & Goldman-Rakic, P. S. (1989). Mnemonic coding of visual space in the monkey's dorsolateral prefrontal cortex. *Journal of Neurophysiology*, *61*(2), 331–349.

Fusi, S., & Mattia, M. (1998). Collective behavior of networks with linear (VLSI) integrate-and-fire neurons. *Neural Computation*, *11*(3), 633-652.

Fuster, Joaquin M. (1973). Unit activity in prefrontal cortex during delayed-response performance: Neuronal correlates of transient memory. *Journal of Neurophysiology*, *36*(1), 61–78.

Fuster, J. M. (1988). Prefrontal cortex. In *Comparative Neuroscience and Neurobiology* (pp. 107-109). Birkhäuser Boston.

Gabbott PL, Warner TA, Jays PR, Salway P, Busby SJ (2005) Prefrontal cortex in the rat: projections to subcortical autonomic, motor, and limbic centers. *Journal of Computational Neurology* 492:145-177.

Gee S, Ellwood I, Patel T, Luongo F, Deisseroth K, Sohal VS (2012) Synaptic activity unmasks dopamine D2 receptor modulation of a specific class of layer V pyramidal neurons in prefrontal cortex. *Journal of Neuroscience* 32:4959-4971.

Glykos V, Whittington MA, LeBeau FE (2015) Subregional differences in the generation of fast network oscillations in the rat medial prefrontal cortex (mPFC) in vitro. *Journal of Physiology*. 593(3):3597-615.

Goldman-Rakic, P S. (1995). Cellular basis of working memory. *Neuron*, *14*(3), 477–485.

Goodman, D., & Brette, R. (2008). Brian: a simulator for spiking neural networks in Python. *Frontiers in Neuroinformatics*, 2(5).

Goodman, D. F., & Brette, R. (2009). The brian simulator. *Frontiers in neuroscience*, 3, 26.

Gruber, A. J., & McDonald, R. J. (2012). Context, emotion, and the strategic pursuit of goals: interactions among multiple brain systems controlling motivated behavior. *Frontiers in Behavioral Neuroscience*, *6*.

Hajos N, Katona I, Naiem SS, MacKie K, Ledent C, Mody I, and Freund TF. Cannabinoids inhibit hippocampal GABAergic transmission and network oscillations. *European Journal of Neuroscience* 12: 3239-3249, 2000.

Harney, S. C., & Jones, M. V. (2002). Pre-and postsynaptic properties of somatic and dendritic inhibition in dentate gyrus. *Neuropharmacology*, 43(4), 584-594.

Hasselmo ME, Sarter M (2011) Modes and models of forebrain cholinergic neuromodulation of cognition. *Neuropsychopharmacology* 36:52-73.

He C, Chen F, Li B, Hu Z (2014) Neurophysiology of HCN channels: from cellular functions to multiple regulations. *Progress in Neurobiology* 112:1-23.

Herding, J., Spitzer, B., & Blankenburg, F. (2016). Upper beta band oscillations in human premotor cortex encode subjective choices in a vibrotactile comparison task. *Journal of cognitive neuroscience*.

Herrmann CS, Frund I, Lenz D (2010) Human gamma-band activity: a review on cognitive and behavioral correlates and network models. *Neuroscience & Biobehavioral Reviews* 34:981-992.

Hillman KL, Bilkey DK (2010) Neurons in the rat anterior cingulate cortex dynamically encode cost-benefit in a spatial decision-making task. *Journal of Neuroscience* 30:7705-7713.

Hines, M. L., & Carnevale, N. T. (1997). The NEURON simulation environment. *Neural computation*, 9(6), 1179-1209.

Hodgkin, A. L., & Huxley, A. F. (1952). A quantitative description of membrane current and its application to conduction and excitation in nerve. *The Journal of physiology*, *117*(4), 500.

Holroyd, C. B., & Yeung, N. (2011). An integrative theory of anterior cingulate cortex function: Option selection in hierarchical reinforcement learning. *Neural basis of motivational and cognitive control*, 333-349.

Hoover WB, Vertes RP (2007) Anatomical analysis of afferent projections to the medial prefrontal cortex in the rat. *Brain Structure and Function* 212:149-179.

Hopfield, J. J. (1982). Neural networks and physical systems with emergent collective computational abilities. *Proceedings of the national academy of sciences*, *79*(8), 2554-2558.

Hormuzdi SG, Pais I, LeBeau FE, Towers SK, Rozov A, Buhl EH, Whittington MA, and Monyer H. Impaired electrical signaling disrupts gamma frequency oscillations in connexin 36-deficient mice. *Neuron* 31: 487-495, 2001.

Hutcheon B, Yarom Y (2000) Resonance, oscillation and the intrinsic frequency preferences of neurons. *Trends in Neuroscience* 23:216-222.

Hyman JM, Whitman J, Emberly E, Woodward TS, Seamans JK (2013) Action and outcome activity state patterns in the anterior cingulate cortex. *Cerebral Cortex* 23:1257-1268.

Ito S, Stuphorn V, Brown JW, Schall JD (2003) Performance monitoring by the anterior cingulate cortex during saccade countermanding. *Science* 302:120-122.

Jung-Beeman M, Bowden EM, Haberman J, Frymiare JL, Arambel-Liu S, Greenblatt R, Reber PJ, Kounios J (2004) Neural activity when people solve verbal problems with insight. *PLoS Biology* 2:E97.

Kaski, S., & Kohonen, T. (1994). Winner-take-all networks for physiological models of competitive learning. *Neural Networks*, *7*(6), 973-984.

Kawaguchi, Y. A. S. U. O. (1993). Groupings of nonpyramidal and pyramidal cells with specific physiological and morphological characteristics in rat frontal cortex. *Journal of neurophysiology*, *69*(2), 416-431.

Kawaguchi, Y., & Kubota, Y. (1998). Neurochemical features and synaptic connections of large physiologically-identified GABAergic cells in the rat frontal cortex. *Neuroscience*, *85*(3), 677-701.

Kerns, J. G., Cohen, J. D., MacDonald, A. W., Cho, R. Y., Stenger, V. A., & Carter, C. S. (2004). Anterior cingulate conflict monitoring and adjustments in control. *Science*, *303*(5660), 1023-1026.

Keshavarzi S, Sullivan RK, Ianno DJ, Sah P (2014) Functional properties and projections of neurons in the medial amygdala. *Journal of Neuroscience* 34:8699-8715.

Kesner RP, Churchwell JC (2011) An analysis of rat prefrontal cortex in mediating executive function. *Neurobiology of Learning and Memory* 96:417-431.

Komorowski, R. W., Garcia, C. G., Wilson, A., Hattori, S., Howard, M. W., & Eichenbaum, H. (2013). Ventral hippocampal neurons are shaped by experience to represent behaviorally relevant contexts. *Journal of Neuroscience*, *33*(18), 8079-8087.

Konstantoudaki, X., Papoutsi, A., Chalkiadaki, K., Poirazi, P., & Sidiropoulou, K. (2016). Modulatory effects of inhibition on persistent activity in a cortical microcircuit model. *Towards an Integrated Approach to Measurement, Analysis and Modeling of Cortical Networks*.

Kopell N, Kramer MA, Malerba P, Whittington MA (2010) Are different rhythms good for different functions? *Frontiers in Human Neuroscience* 4:187.

Cutsuridis, V., Graham, B. P., Cobb, S., & Vida, I. (Eds.). (2010). *Hippocampal microcircuits: a computational modeler's resource book* (Vol. 5). Springer Science & Business Media.

Kopell NJ, Gritton HJ, Whittington MA, Kramer MA (2014) Beyond the connectome: the dynome. *Neuron* 83:1319-1328.

Kramer, M. A., Roopun, A. K., Carracedo, L. M., Traub, R. D., Whittington, M. A., & Kopell, N. J. (2008). Rhythm generation through period concatenation in rat somatosensory cortex. *PLoS Computational Biology*, 4(9), e1000169.

Kriete, T., Noelle, D. C., Cohen, J. D., & O'Reilly, R. C. (2013). Indirection and symbol-like processing in the prefrontal cortex and basal ganglia. *Proceedings of the National Academy of Sciences*, 110(41), 16390-16395.

Kvitsiani D, Ranade S, Hangya B, Taniguchi H, Huang JZ, Kepecs A (2013) Distinct behavioural and network correlates of two interneuron types in prefrontal cortex. *Nature* 498:363-366.

Lakatos P, Shah AS, Knuth KH, Ulbert I, Karmos G, Schroeder CE (2005) An oscillatory hierarchy controlling neuronal excitability and stimulus processing in the auditory cortex. *Journal of Neurophysiology* 94:1904-1911.

Lapish CC, Durstewitz D, Chandler LJ, Seamans JK (2008) Successful choice behavior is associated with distinct and coherent network states in anterior cingulate cortex. *Proceedings of the National Academy of Sciences* U S A 105:11963-11968.

Lee AT, Gee SM, Vogt D, Patel T, Rubenstein JL, Sohal VS (2014) Pyramidal neurons in prefrontal cortex receive subtype-specific forms of excitation and inhibition. *Neuron* 81:61-68.

Lundqvist, M., Rose, J., Herman, P., Brincat, S. L., Buschman, T. J., & Miller, E. K. (2016). Gamma and beta bursts underlie working memory. *Neuron*, *90*(1), 152-164.

Ma L, Hyman JM, Lindsay AJ, Phillips AG, Seamans JK (2014) Differences in the emergent coding properties of cortical and striatal ensembles. *Nature Neuroscience* 17:1100-1106.

Mai XQ, Luo J, Wu JH, Luo YJ (2004) "Aha!" effects in a guessing riddle task: an event-related potential study. *Human Brain Mapping* 22:261-270.

Markram H et al. (2015) Reconstruction and Simulation of Neocortical Microcircuitry. *Cell* 163:456-492.

Maulik, U., and Bandyopadhyay, S. (2002). Performance evaluation of some clustering algorithms and validity indices. *IEEE Transactions on Pattern Analysis and Machine Intelligence*, *24*(12), 1650-1654.

McCulloch, W. S., & Pitts, W. (1943). A logical calculus of the ideas immanent in nervous activity. *The bulletin of mathematical biophysics*, *5*(4), 115-133.

Medalla, M., & Barbas, H. (2009). Synapses with Inhibitory Neurons Differentiate Anterior Cingulate from Dorsolateral Prefrontal Pathways Associated with Cognitive Control. *Neuron*, *61*(4), 609–620.

Middleton S, Jalics J, Kispersky T, Lebeau FE, Roopun AK, Kopell NJ, Whittington MA, Cunningham MO (2008) NMDA receptor-dependent switching between different gamma rhythm-generating microcircuits in entorhinal cortex. *Proceedings of the National Academy of Sciences* U S A 105:18572-18577.

Miller, E. K., & Cohen, J. D. (2001). An integrative theory of prefrontal cortex function. *Annual review of neuroscience*, *24*(1), 167-202.

Narayanan NS, Cavanagh JF, Frank MJ, Laubach M (2013) Common medial frontal mechanisms of adaptive control in humans and rodents. *Nature Neuroscience* 16:1888-1895.

Neugebauer, V. (2015). Amygdala pain mechanisms. In *Pain Control* (pp. 261-284). Springer Berlin Heidelberg.

Newman, L. A., Creer, D. J., & McGaughy, J. A. (2015). Cognitive control and the anterior cingulate cortex: How conflicting stimuli affect attentional control in the rat. *Journal of Physiology-Paris*, *109*(1), 95-103.

Olufsen, M.S., Whittington, M.A., Camperi, M. & Kopell, N. (2003) New roles for the gamma rhythm: population tuning and preprocessing for the beta rhythm. *Journal of Computational Neuroscience.*, **14**, 33–54.

O'Reilly, R. C., & Frank, M. J. (2006). Making Working Memory Work: A Computational Model of Learning in the Prefrontal Cortex and Basal Ganglia. *Neural Computation*, *18*(2), 283–328.

Orekhova EV, Butorina AV, Sysoeva OV, Prokofyev AO, Nikolaeva AY, Stroganova TA (2015) Frequency of gamma oscillations in humans is modulated by velocity of visual motion. *Journal of Neurophysiology* 114:244-255.

Papoutsi A, Sidiropoulou K, Cutsuridis V, Poirazi P (2013) Induction and modulation of persistent activity in a layer V PFC microcircuit model. *Frontiers in Neural Circuits* 7:161.

Park HJ, Friston K (2013) Structural and functional brain networks: from connections to cognition. *Science* 342:1238411.

Parnaudeau, S., O'Neill, P.-K., Bolkan, S. S., Ward, R. D., Abbas, A. I., Roth, B. L., … Kellendonk, C. (2013). Inhibition of Mediodorsal Thalamus Disrupts Thalamofrontal Connectivity and Cognition. *Neuron*, *77*(6), 1151–1162.

Pennartz, C., van Wingerden, M., & Vinck, M. (2011). Population coding and neural rhythmicity in the orbitofrontal cortex. *Annals of the New York Academy of Sciences*, *1239*(1), 149-161.

Perry G, Randle JM, Koelewijn L, Routley BC, Singh KD (2015) Linear tuning of gamma amplitude and frequency to luminance contrast: evidence from a continuous mapping paradigm. *PLoS One* 10:e0124798.

Phillips WA, von der Malsberg C, Singer W. (2010) Dynamic coordination in the brain. In: '*Dynamic coordination in the brain*'. Eds Von der Malsberg C, Phillips WA, Singer W. MIT press. Pp 1-24.

Pinto L, Dan Y (2015) Cell-Type-Specific Activity in Prefrontal Cortex during Goal-Directed Behavior. *Neuron* 87(2):437-50.

Popescu, A. T., Popa, D., & Paré, D. (2009). Coherent gamma oscillations couple the amygdala and striatum during learning. *Nature neuroscience*, *12*(6), 801-807.

Povysheva, N. V., Zaitsev, A. V., Rotaru, D. C., Gonzalez-Burgos, G., Lewis, D. A., & Krimer, L. S. (2008). Parvalbumin-positive basket interneurons in monkey and rat prefrontal cortex. *Journal of neurophysiology*, *100*(4), 2348-2360.

Randall, F. E., Whittington, M. A., & Cunningham, M. O. (2011). Fast oscillatory activity induced by kainate receptor activation in the rat basolateral amygdala in vitro. *European Journal of Neuroscience*, 33(5), 914-922.

Richardson, M. J., Brunel, N., & Hakim, V. (2003). From subthreshold to firing-rate resonance. *Journal of neurophysiology*, *89*(5), 2538-2554.

Rigotti, M., Ben Dayan Rubin, D. D., Wang, X. J., & Fusi, S. (2010). Internal representation of task rules by recurrent dynamics: the importance of the diversity of neural responses. *Frontiers in computational neuroscience*, *4*, 24.

Roopun AK, Kramer MA, Carracedo LM, Kaiser M, Davies CH, Traub RD, Kopell NJ, Whittington MA (2008a) Temporal Interactions between Cortical Rhythms. *Frontiers in Neuroscience* 2:145-154.

Roopun AK, Kramer MA, Carracedo LM, Kaiser M, Davies CH, Traub RD, Kopell NJ, Whittington MA (2008b) Period concatenation underlies interactions between gamma and beta rhythms in neocortex. *Frontiers in Cell Neuroscience* 2:1.

Roopun AK, Middleton SJ, Cunningham MO, LeBeau FE, Bibbig A, Whittington MA, Traub RD (2006) A beta2-frequency (20-30 Hz) oscillation in nonsynaptic networks of somatosensory cortex. *Proceedings of the National Academy of Sciences* U S A 103:15646-15650.

Rosenblatt, F. (1958). The perceptron: A probabilistic model for information storage and organization in the brain. *Psychological review*, *65*(6), 386.

Roux, F., Wibral, M., Mohr, H. M., Singer, W., & Uhlhaas, P. J. (2012). Gamma-band activity in human prefrontal cortex codes for the number of relevant items maintained in working memory. *Journal of Neuroscience*, *32*(36), 12411-12420.

Schouwenburg, M. R. van, O'Shea, J., Mars, R. B., Rushworth, M. F. S., & Cools, R. (2012). Controlling Human Striatal Cognitive Function via the Frontal Cortex. *The Journal of Neuroscience*, *32*(16), 5631–5637.

Serenevy, A. K., & Kopell, N. J. (2013). Effects of heterogeneous periodic forcing on inhibitory networks. *SIAM Journal on Applied Dynamical Systems*, *12*(3), 1649-1684.

Shenhav A, Botvinick MM, Cohen JD (2013) The expected value of control: an integrative theory of anterior cingulate cortex function. *Neuron* 79:217-240.

Shenhav, A., Cohen, J. D., & Botvinick, M. M. (2016). Dorsal anterior cingulate cortex and the value of control. *Nature Neuroscience*, *19*(10), 1286-1291.

Siegel, M., Warden, M. R., & Miller, E. K. (2009). Phase-dependent neuronal coding of objects in short-term memory. *Proceedings of the National Academy of Sciences*, *106*(50), 21341–21346.

Sohal, V. S., Zhang, F., Yizhar, O., & Deisseroth, K. (2009). Parvalbumin neurons and gamma rhythms enhance cortical circuit performance. *Nature*, *459*(7247), 698-702.

Sosulina L, Meis S, Seifert G, Steinhauser C, Pape HC (2006) Classification of projection neurons and interneurons in the rat lateral amygdala based upon cluster analysis. *Molecular and Cellular Neuroscience* 33:57-67.

Steullet P, Cabungcal JH, Cuenod M, Do KQ (2014) Fast oscillatory activity in the anterior cingulate cortex: dopaminergic modulation and effect of perineuronal net loss. *Frontiers in Cellular Neuroscience* 8:244.

Straube B, Green A, Chatterjee A, Kircher T (2011) Encoding social interactions: the neural correlates of true and false memories. *Journal of Cognitive Neuroscience* 23:306-324.

Tegnér, J., Compte, A., & Wang, X. J. (2002). The dynamical stability of reverberatory neural circuits. *Biological cybernetics*, *87*(5), 471-481.

Teixeira CM, Pomedli SR, Maei HR, Kee N, Frankland PW (2006) Involvement of the anterior cingulate cortex in the expression of remote spatial memory. *Journal of Neuroscience* 26:7555-7564.

Thomson AM, West DC, Hahn J, Deuchars J (1996) Single axon IPSPs elicited in pyramidal cells by three classes of interneurones in slices of rat neocortex. *Journal of Physiology* 496 (Pt 1):81-102.

Traub, R. D., Contreras, D., Cunningham, M. O., Murray, H., LeBeau, F. E., Roopun, A., ... & Whittington, M. A. (2005). Single-column thalamocortical network model exhibiting gamma oscillations, sleep spindles, and epileptogenic bursts. *Journal of neurophysiology*, *93*(4), 2194-2232.

Tzur, G., & Berger, A. (2009). Fast and slow brain rhythms in rule/expectation violation tasks: Focusing on evaluation processes by excluding motor action. *Behavioural Brain Research*, *198*(2), 420–428.

Van Aerde, K. I., Mann, E. O., Canto, C. B., Heistek, T. S., Linkenkaer-Hansen, K., Mulder, A. B., … Mansvelder, H. D. (2009). Flexible spike timing of layer 5 neurons during dynamic beta oscillation shifts in rat prefrontal cortex. *The Journal of Physiology*, *587*(21), 5177–5196.

van Aerde KI, Feldmeyer D (2015) Morphological and physiological characterization of pyramidal neuron subtypes in rat medial prefrontal cortex. *Cerebral Cortex* 25:788-805.

van Burik, M., Knösche, T., Edlinger, G., Neuper, C., Pfurtscheller, G., Peters, M. (1998). Post-movement beta oscillations studied with linear estimation. *Electroencephalography and clinical neurophysiology*, *106*(3), 195-198.

Vogt BA, Paxinos G (2014) Cytoarchitecture of mouse and rat cingulate cortex with human homologies. *Brain Structure and Function* 219:185-192.

Voloh, B., Valiante, T. A., Everling, S., & Womelsdorf, T. (2015). Theta–gamma coordination between anterior cingulate and prefrontal cortex indexes correct attention shifts. *Proceedings of the National Academy of Sciences*, *112*(27), 8457-8462.

Wagner, D. A., Goldschen-Ohm, M. P., Hales, T. G., & Jones, M. V. (2005). Kinetics and Spontaneous Open Probability Conferred by the ϵ Subunit of the GABAA Receptor. *Journal of Neuroscience*, 25(45), 10462-10468.

Walton ME, Bannerman DM, Alterescu K, Rushworth MF (2003) Functional specialization within medial frontal cortex of the anterior cingulate for evaluating effort-related decisions. *Journal of Neuroscience* 23:6475-6479.

Wang, M., Yang, Y., Wang, C. J., Gamo, N. J., Jin, L. E., Mazer, J. A., ... & Arnsten, A. F. (2013). NMDA receptors subserve persistent neuronal firing during working memory in dorsolateral prefrontal cortex. *Neuron*, *77*(4), 736-749.

Wang XJ, Buzsaki G (1996) Gamma oscillation by synaptic inhibition in a hippocampal interneuronal network model. *Journal of Neuroscience* 16:6402-6413.

Wang, X. J. (1999). Synaptic basis of cortical persistent activity: the importance of NMDA receptors to working memory. *The Journal of Neuroscience*, *19*(21), 9587-9603.

Wartman BC, Gabel J, Holahan MR (2014) Inactivation of the anterior cingulate reveals enhanced reliance on cortical networks for remote spatial memory retrieval after sequential memory processing. *PLoS One* 9:e108711.

Whittington MA, Traub RD, Jefferys JG (1995) Synchronized oscillations in interneuron networks driven by metabotropic glutamate receptor activation. *Nature* 373:612-615.

Whittington, M. A., Stanford, I. M., Colling, S. B., Jefferys, J. G., & Traub, R. D. (1997). Spatiotemporal patterns of γ frequency oscillations tetanically induced in the rat hippocampal slice. *The Journal of Physiology*, *502*(3), 591-607.

Whittington MA, Cunningham MO, LeBeau FE, Racca C, Traub RD (2011) Multiple origins of the cortical gamma rhythm. *Developmental Neurobiology* 71:92-106.

Womelsdorf, T., Ardid, S., Everling, S., & Valiante, T. A. (2014). Burst firing synchronizes prefrontal and anterior cingulate cortex during attentional control. *Current Biology*, *24*(22), 2613-2621.

Yamada W, Koch C, Adams P (1998). Multiple channels and calcium dynamics. In: *Methods in neuronal modelling: from ions to networks*. Eds. Koch, C, Segev, I. (pp 137-170) MIT Press.

Yang CR, Seamans JK, Gorelova N (1996) Electrophysiological and morphological properties of layers V-VI principal pyramidal cells in rat prefrontal cortex in vitro. *Journal of Neuroscience* 16:1904-1921.

Yin, H. H., & Knowlton, B. J. (2006). The role of the basal ganglia in habit formation. *Nature Reviews Neuroscience*, *7*(6), 464–476.

Zaitsev, A. V., Povysheva, N. V., Gonzalez-Burgos, G., Rotaru, D., Fish, K. N., Krimer, L. S., & Lewis, D. A. (2009). Interneuron diversity in layers 2–3 of monkey prefrontal cortex. *Cerebral Cortex*, 19(7), 1597-1615.

CURRICULUM VITAE

Jason Samuel Sherfey

sherfey@bu.edu
(423) 316-8275
www.JasonSherfey.com
Year of birth: 1984

EDUCATION
1. PhD Candidate in Computational Neuroscience
   Boston University, Boston, Massachusetts (2017).
2. Bachelor of Engineering in Biomedical Engineering
   Vanderbilt University, Nashville, Tennessee (2006).
3. High school diploma, The McCallie Preparatory School, Chattanooga, Tennessee (2002).
   "*One of the leading secondary institutions in the United States*" (Atlanta Journal-Constitution)

EXPERIENCE
2011-2017 PhD Candidate, Boston University
1. Designed and wrote proposal for $600,000 three-year research grant awarded by the Army Research Office in 2014 to use a combination of experimental and computational modeling techniques to study the functional role of brain rhythms in rule-based decision making. Funds supported grant writer's graduate work with Nancy Kopell, as well as two postdoctoral fellows.
2. ACC dynamics: developed a biophysical model of the anterior cingulate cortex (ACC) to study how rhythmic signals are selected or combined in heterogeneous networks. The model was constrained by rat *in vitro* data, provided by the LeBeau lab at Newcastle University; cellular intrinsic properties were derived from voltage recordings and were used to constrain biophysical model parameters. Simulations revealed that heterogeneity supports combinatorial processing of multiple rhythmic and/or asynchronous inputs, possibly serving evidence accumulation for updating rules that guide action selection. The biophysical model is publicly available at github.com/jsherfey/ACd_model.
3. Superficial PFC dynamics: adapted a biophysical model of prefrontal cortex (PFC) to incorporate multiple types of interneurons, motivated by anatomical findings from the Barbas lab at BU, to study how signals from posterior cortex and ACC interact in PFC to control whether cell assemblies exhibit asynchronous or rule-associated rhythmic activity. These simulations suggest that interneurons specifically targeted by ACC underlie rule-associated rhythmicity whereas a different interneuron class stabilizes working memory representations whether synchronous or asynchronous.
4. Deep layer PFC dynamics: studied how filter characteristics of target networks are shaped by properties of the input population activity. Simulations revealed that modulating spike synchrony and population rhythmicity can be used to select assemblies and suppress noise in deep layer networks. These results demonstrate the functional utility of PFC rhythms for governing which cortical signals are transmitted to subcortical

targets and provide insight into roles for rhythms observed by the Miller lab at MIT in monkeys performing rule-based tasks. The biophysical model is publicly available at github.com/jsherfey/PFC_models.

5. Developed open-source modeling and simulation software for the computational neuroscience community.
    a. DynaSim is a Matlab/Octave toolbox for rapid prototyping of large neural models, batch simulation management, and efficient model sharing. It is designed to speed up and simplify the process of generating, sharing, and exploring network models of neurons with a few compartments. It is publicly available at github.com/DynaSim/DynaSim.
    b. InfiniteBrain.org is a computational model repository to facilitate collaborative model building and simulation studies before they are published. It is coupled to DynaSim using database connectors to enable automated generation of new models from combinations of smaller models stored locally and/or in the InfiniteBrain repository.
6. Completed two preliminary laboratory rotation projects:
    a. Designed, implemented, and ran experiments with two subjects performing a speech decoding task to assess viability of ECoG-based brain-machine-interface for speech production. This work was done in collaboration with the speech lab of Frank Guenther at BU and the epilepsy lab of Syd Cash at MGH. The study revealed that macroelectrode intracranial recordings have insufficient resolution to support decoding imagined speech with high accuracy.
    b. Adapted a biophysical model of somatosensory rhythms to study the molecular basis of abnormal brain rhythms in schizophrenia. Simulations revealed that dysregulation of GAD expression disrupted rhythm-mediated cortical communication by synchronizing activity in different lamina. Obtained a one-year Computational Neuroscience Training from BU for this work.

2008-2011 Neuroimaging Research Associate, Multimodal Imaging Laboratory
1. Developed software modules for a complex data processing stream to analyze MEG, EEG, and intracranial EEG recordings. Designed a set of powerful functions to encapsulate multiple interdependent software packages and present a single user-friendly interface; this eliminated the need for user programming and simplified cluster computing. Developed a graphical interface for the analysis stream with comprehensive user manual and step-by-step tutorials. Trained technicians at MGH, NYUMC, and UCSD to use the program. Contributed to the design, implementation and refinement of wavelet-based time-frequency analysis. Implemented algorithms to compute the spatiotemporal evolution of synchronous clusters based on phase-locking values. Implemented a Monte Carlo statistical permutation test which used spatiotemporal clustering to correct for multiple comparisons. Participated in the validation of a time-frequency estimate of the EEG/MEG inverse solution.
2. Analyzed human intracranial macroelectrode and laminar recordings from epileptic patients and EEG/MEG recordings from healthy subjects during sleep and while performing cognitive tasks such as the Erikson-Flanker and Stroop naming tasks using custom neuroimaging software. Identified spectro-spatio-temporal clusters of significant differences in spectral power between multiple experimental conditions. Optimized time-

frequency analysis protocols for studying event-related changes in power, coherence, and phase-locking for recording systems with hundreds of electrodes. Designed and implemented an efficient slow oscillation detection algorithm and analysis protocol to study gamma power modulation by slow oscillations during slow-wave sleep.
3. Facilitated collaboration between multiple laboratories across the country (NYU, UCSD, MGH) by organizing and directing monthly teleconferences.
4. Managed the archiving of neuroimaging data from several research laboratories. Set up a software version control system to facilitate standardization of analyses and to reduce duplication of efforts.

2008 MATLAB Simulations
Simulated spiking and bursting activity using conductance-based models of cortical and thalamic neurons presented in "Dynamical Systems in Neuroscience" by EM Izhikevich. Performed phase space and perturbation analyses of these mathematical neuron models.

2007-2008 Validation Engineer and Research Scientist, Schering-Plough Corporation
1. Participated in all phases of more than one dozen validation studies for aerosol and drug products. Tasks included protocol preparation, supervision of 100,000-unit manufacturing operations, analysis coordination with chemistry and microbiology laboratories, performing statistical analysis of results, as well as summary report compilation.
2. Participated in the scale-up of new and modified alcohol-based product formulations from the initial process development stage up to full-scale commercial production.
3. Participated in scientific investigations of process deviations and product defects. Directed a complex investigation requiring coordination of multiple departments at different sites, third-party vendors and researchers to investigate the functionality of nearly one million units of an aerosol product.
4. Coordinated in-house acquisition of component materials with a third-party research laboratory to perform high pressure liquid chromatography – mass spectrometry experiments and collaborated with a material science expert to improve product quality.
5. Conducted experiments to quantify metal exposure of liner-coated aluminum surfaces by measuring currents passing from an electrolyte through the aluminum layer. Advised a related investigation regarding a vendor manufacturing process; discovered and corrected the root cause of an important manufacturing problem. The entire investigation salvaged more than $3,000,000 in product value.

2005-2007 Biomedical Engineering Research Assistant, Vanderbilt Institute for Integrative Biosystem Research and Education (VIIBRE)
1. Developed a software package in MATLAB to study the mechanical properties of cancerous cells *in vitro*. The program had the ability to automate video image processing with object tracking and statistical analysis of structural deformations. First, videos were recorded of cells that stretched when magnetic forces were applied using magnetic microspheres. The amount of deformation was employed to characterize cellular mechanics. Videos of cell-bound microspheres were analyzed by bright field filtering, pre-processing parameter estimation, microsphere centroid computation and by linking

centroids to reconstruct cell trajectories. Parameter fitting was applied for each cell trajectory to characterize cellular mechanical properties and the parameters were used to determine statistically significant differences in cellular characteristics between and within populations.

2. Designed photolithographic masks in AutoCAD for the microfabrication of microfluidic devices. Drawings were used to prepare photomasks to pattern bulk substrates. Patterned substrates functioned as molds for the soft lithographic replication of elastomeric microfluidic devices.

3. Designed, fabricated and validated a microsystem to control and measure structural properties of cell membranes. An electromagnet was embedded in a microfluidic device housing epithelial cells bound to a glass slide. Magnetic microspheres with an adhesive coating were bound to cell membranes and transmitted electromagnetic forces to cells as tensile stresses. The experimental apparatus included a LabView program to control a micromanipulator holding the microsystem and a power supply regulating the force.

4. Maintained epithelial cell cultures; designed protocols for microsystem microfabrication, binding microspheres to cells and force calibration. Performed cell-stretching experiments where forces were indirectly applied to cells and videos of the response were recorded.

2005-2007 NEURON Simulations
Simulated rhythmicity in thalamocortical networks using NEURON models made available by the Human Brain Project through the SenseLab ModelDB database. Simulated the Sejnowski-Destexhe-Traub models, modified pre-existent NEURON models and performed simulation experiments using physiological parameter values.

2001 St3, Inc.
Maintained the nationwide activity database of an internet video streaming company and participated in the development of web applications to monitor the activity and performance of internet video streams. Programmed Active Server Pages (ASP) with ActiveX data objects in VBScript to connect to remote servers, download and parse activity logs, and display data in a browser or store it directly to a local database.

1997-2001 Novell Network Administrator
Built two computer laboratories at a secondary school and managed user accounts, security, and network services. Set up networks and provided technical support for the Family Theatre Workshop and the Salvation Army.

COMPUTER SKILLS
Programming Languages: proficient in Matlab, Python, C/C++, object-oriented programming, shell scripting (csh, tcsh, bash), tcl, LabView, Visual Basic, ASP.NET, VBScript, JavaScript/jQuery, JSON, XML, PHP, AJAX, SQL/MySQL, HTML, CSS; familiar with Perl, R, IDL, Java.
Operating Systems: proficient in Windows and Linux (including command line and scripting).

Neuroimaging Software: proficient in Elekta Neuromag software, Neuroscan Data Analysis software, FieldTrip, EEGLAB, TimeSurfer, MNE-Suite; familiar with FreeSurfer, BrainVision. PsychoPy.

Other Applications: proficient in NEURON, Microsoft Office Suite programs; SPSS/PASW, Mathematica, AutoCAD; Adobe Illustrator, CorelDRAW, DreamWeaver, Subversion, Git; familiar with Photoshop, Camtasia.

TRAINING AND SKILLS
1. Experimental techniques: Successfully acquired intracellular voltage recordings from two cells in a rat ACC slice using a micromanipular-controlled glass microelectrode at Newcastle University. Acquired human ECoG recordings at MGH from two patients performing a speech decoding task implemented in PsychoPy.
2. Anatomical network analysis: Aggregated tract tracing data from over 300 studies in the CoCoMac database to construct a primate macro-connectome for quantifying the relative connection strengths between brain areas and for identifying source and target layers. The main challenge in aggregating data across studies is mapping correspondences between areas because standard atlases do not exist for primate neuroanatomy. Developed a simple solution using synonyms to define regions of interest that has produced useful connection density estimates. Analyzed network properties of the resulting macro-connectomes (e.g., network centrality of prefrontal regions).
3. Data-driven biophysical parameter estimation: validated a Bayesian procedure, particle filtering, for adaptively estimating biophysical parameters of a single cell model given an experimental spike train. Tested its ability to fit an Izhikevich model neuron to the spike times of a stellate cell driven by an injected current. The particle filter converged on a parameter value with a narrow confidence interval after processing 5 seconds of data; the simulated voltage trace produced dynamics capturing the real stellate spike times and, surprisingly, the continuous subthreshold oscillation.
4. Multimodal imaging: Analyzed neuroimaging data using a complex software data processing stream. Developed software modules for the TimeSurfer package which incorporate FieldTrip, EEGLAB, Elekta Neuromag Software, and Neuroscan Software. Analyzed MEG/EEG and intracranial EEG data using the stream to perform artifact rejection, waveform averaging, statistical comparisons, and time-frequency analysis.
5. Schering-Plough: Trained in the management of pharmaceutical & health care manufacturing line operators during the execution of commercial-scale validation studies, root-cause investigations, and process demonstrations.
6. Neural pathophysiology: Studied the neural pathophysiology of epilepsy (reduced GABA-A receptor mediated inhibition; increased cholinergic excitation), psychosis (Dopamine hypothesis, Glutamate hypothesis), and depression (Monoamine theory, HPA axis dysregulation). Reviewed current findings in bipolar disorder research including neuroanatomical abnormalities, dysregulation of the HPA axis, neurotransmitter systems, circadian rhythms, and intracellular signaling systems.
7. Computational modeling: Attended the NEURON 2009 Summer Course at UCSD. Modeled neural excitability and analyzed chaotic dynamics in the phase plane. Conducted and presented a simulation study to demonstrate the ability of varying an individual synaptic weight to switch a network between stable, periodic, and chaotic

behaviors in an artificial neural network consisting of three neurons characterized by firing rate models. Completed a modeling and simulation project comparing three FEM models of convective diffusive transport of drugs in the brain. Other topics included principal component analysis (PCA), FEM, BEM, image registration, and MRI. Attended the workshop "Using The NEURON Simulation Environment" presented by Michael Hines, Ted Carnevale, and Gordon Shepherd at the Satellite Symposium Society for Neuroscience Meeting, Atlanta, GA, 2006.

8. Biomedical data analysis: Analyzed historical psychiatric hospitalization rate data to describe the evolution of regional differences in the treatment of mental illness in the United States during the 20th century.

9. Biomedical instrumentation: Built an ECG measurement system consisting of an ECG circuit with electrodes and a LabView data acquisition module; designed and built an accelerometer with digital display. Familiar with transduction and measurement devices.

10. Experimental systems biology: Reviewed journal articles on stochasticity in neurotransmitter release and cell surface receptor density, feedback loops in intracellular signaling pathways, high-dimensional attractors in nonlinear biological systems, and biologically realistic modeling of cell states. Prepared a paper that derived and compared Leaky Integrate-and-Fire model neurons and Hodgkin-Huxley model neurons. Reviewed the merits and limitations of each class, and discussed the role of computational modeling in the search for the pathophysiology of brain disorders.

11. Laboratory techniques. Received training in clean rooms and microfabrication techniques at VIIBRE, including forming SU-8 structures with photolithography and casting polydimethylsiloxane structures using soft lithography. Received training in cell culture epithelial cells including sterile technique and feeding, counting, and splitting cell cultures.

HONORS AND ACHIEVEMENTS

2014 Army Research Office 3-year research grant award (served as grant author) (W911NF1410374).
2013-2014 Computational Neuroscience Training Grant at Boston University (NIH 5R90DA033460-03).
2012 Elected Treasurer of the Computational Neuroscience Student Organization at Boston University.
2009 Elected member of the Vanderbilt chapter of Sigma Xi, The Scientific Research Society.
2007 Passed the Society of Actuaries Exam P – general probability, univariate probability distributions, and multivariate probability distributions.
2005 Summer Research Fellowship at Vanderbilt University in Biomedical Engineering
2004-2006 Named to the Vanderbilt University Dean's List.
2002-2003 Founded and managed Sifter Software, a software business enterprise, providing rapid web design and networking solutions to expedite the startup of new companies.
2002 Performed at Carnegie Hall in New York City with the Select Ensemble Chorus, conducted by John Rutter and accompanied by the New England Symphonic Ensemble, in a program entitled "Pomp and Pageantry," including selections by Walton, Parry, Händel and Rutter.

2001 Selected to the Select Ensemble Chorus of Chattanooga, Tennessee, an honors chorus consisting of singers from each of the top college preparatory schools in the city.
2001 Selected by contest to represent the McCallie School Debate Team at four competitions in various US states.
1998 Novell Adminstrator certification from Novell Inc, for the administration of local area networks running Novell NetWare, a network operating system developed by Novell Inc.
1993-2001 Accomplished pianist: invited to play weekly at local restaurant and venues to provide entertainment and improve ambience with jazz, blues and by improvisation. Most challenging piece: "Flight of the Bumblebee" by Nikolai Rimsky-Korsakov.

COMMUNITY SERVICE
2013 Food Not Bombs – serving free food in Central Square Cambridge.
2006-Present Vanderbilt Alumni Association.
2002-Present McCallie Alumni Association.
2007-2008 Advisory Board/Founding Member, Creative Discovery Museum Young Professionals, Chattanooga, TN.
2007-2008 YPAC (Young Professionals of Chattanooga) Member, Chattanooga, TN.
2007-2008 Community Association of Historic St. Elmo, Chattanooga, TN.
2007-2008 Schering-Plough Bowling League Member, Cleveland, TN.
2001-2002 The McCallie Hague Founding Member – an independent weekly discussion group with 15 members and topics related to Society and Technology organized around weekly presentations.
2001-2002 Family Theatre Workshop – participated in set construction and computer support.
1999-2000 Salvation Army – volunteered computer support and troubleshooting.

PEER-REVIEWED PUBLICATIONS

1. Adams*, N. E., Sherfey*, J. S., Kopell, N. J., Whittington, M. A., & LeBeau, F. E. (2017). Hetereogeneity in Neuronal Intrinsic Properties: A Possible Mechanism for Hub-Like Properties of the Rat Anterior Cingulate Cortex during Network Activity. *eNeuro*, *4*(1), ENEURO-0313. *Both authors contributed equally to this work.

2. Ardid, S., Sherfey, J., McCarthy, M. M., Hass, J., & Kopell, N. (2016). Unraveling action selection and inhibitory control mechanisms in a striatal microcircuit model. *International Journal of Psychophysiology*, (108), 18.

3. Sherfey, J., Ardid, S., Hass, J., Kopell, N. (2017). Resonance enables prefrontal beta and gamma oscillations to bias pathways for thought and action. *eLife* (in preparation).

4. Sherfey, J., Ardid, S., Soplata, A., Kopell, N. (2017). DynaSim: a collaborative simulation platform for biophysically-detailed neural modeling. *Frontiers in Neuroinformatics* (in preparation).

5. Hass, J., Ardid, S., Sherfey, J., Kopell, N. (2017). Constraints on Persistent Activity in a Realistic Network Model of the Prefrontal Cortex with Heterogeneous Neurons. (in preparation).

6. Soplata A., McCarthy M., Sherfey J., Lee S., Purdon P., Brown E., Kopell N. (2017). Thalamocortical control of propofol phase-amplitude coupling. *PLoS Computational Biology* (in preparation).

7. Kovacevic, S., Azma, S., Irimia, A., Sherfey, J., Halgren, E., & Marinkovic, K. (2012). Theta oscillations are sensitive to both early and late conflict processing stages: effects of alcohol intoxication. *PLoS One*, *7*(8).

8. Thesen, T. T., McDonald, C. R., Carlson, C., Doyle, W., Cash, S., Sherfey, J. S., Felsovalyi, O., Girard H., Barr, W., Devinsky, O., Kuzniecky, R., Halgren, E. (2012). Sequential then interactive processing of letters and words in the left fusiform gyrus. *Nature Communications*, *3*, 1284.

9. Halgren, E., Sherfey, J. S., Irimia, A., Dale A. M., & Marinkovic, K. (2010). Sequential Temporo-fronto-temporal activation during monitoring of the auditory environment for temporal patterns. *Human Brain Mapping, 2010 Jul 27.*

10. McDonald, C. R., Thesen, T., Carlson, C., Blumberg, M., Girard, H. M., Trongnetrpunya, A., Sherfey, J. S., Devinsky, O., Kuzniecky, R., Cash, S., Leonard, M. K., Hagler, D. J., Jr., Dale, A. M., & Halgren, E. (2010). Multimodal imaging of repetition priming: Using fMRI, MEG, and intracranial EEG to reveal spatiotemporal profiles of word processing. *Neuroimage,* 53(2):707-17.

CONFERENCE PRESENTATIONS

1. Sherfey JS, Lopell NJ. (2016). Competition versus cooperation in the anterior cingulate cortex. Presented at 2016 Cognitive Rhythms Collaborative Retreat, Boston, MA.

2. Sherfey JS, Kopell NJ. (2014). Prefrontal brain rhythms for rule-based action. Presented at 2014 Gordon Research Seminar, Newry, ME.

3. Sherfey JS, Kopell NJ. (2014). Cortical rhythms and interneurons for reading working memory: a computational study of laminar DLPFC. Presented at 2014 Cognitive Rhythms Collaborative Retreat, Boston, MA.

CONFERENCE POSTERS

1. Sherfey JS. (2016). *DynaSim: a Matlab toolbox for rapidly building and exploring neural models*. 2016 Janelia conference on Collaborative Development of Data-Driven Models of Neural Systems, Ashburn, Virginia.

2. Sherfey, J., Ardid, S., McCarthy, M., Hass, J., Kopell, N. (2016). *Oscillations guide rule-based action in a laminar model of prefrontal cortex*. 2016 Society for Neuroscience Meeting, San Diego, CA.

3. Soplata A, Sherfey J, Purdon P, Brown E, Kopell N. (2016). *Thalamic generation of propofol phase amplitude coupling*. 2016 Society for Neuroscience Meeting, San Diego, CA.

4. Ardid, S., Sherfey, J., McCarthy, M., Hass, J., Kopell, N. (2016). *Alpha oscillatory inputs and short-term depression underlie action inhibitory control in a model of the striatum*. 2016 Society for Neuroscience Meeting, San Diego, CA.

5. Hass J, Ardid S, Sherfey J, Kopell N. (2016). *Constraints on Persistent Activity in a Biophysically Detailed Network Model of the Prefrontal Cortex with Heterogeneous Neurons*. Bernstein conference abstract 2016.

6. Sherfey JS, Adams NE, LeBeau FEN, Kopell NJ. (2015). *Modeling neuronal diversity and fast network oscillations in rat anterior cingulate cortex (ACC)*. 2015 Society for Neuroscience Meeting, Chicago, IL.

7. Ardid S, Sherfey J, McCarthty MM, Kopell N. (2015). *Context-dependent action selection mediated by specific temporal coordination between prefrontal cortex and striatum*. 2015 Society for Neuroscience Meeting.

8. Sherfey JS, Kopell NJ. (2014). *Dynamic Neural Simulator - a simple tool for rapidly building and sharing large neural models*. 2014 Society for Neuroscience Meeting, Washington D.C.

9. Sherfey JS, Kopell NJ. (2014). *Prefrontal brain rhythms for rule-based action*. 2014 Gordon Research Conference, Newry, ME.

10. Sherfey JS, Adams NE, Kopell NJ. (2013). *Cortical rhythms and interneurons for reading working memory: a computational study of laminar DLPFC*. 2013 Society for Neuroscience Meeting, San Diego, CA.

11. Adams, N., Sherfey, J. S., Whittington, M. A., Kopell, N. J. , LeBeau, F. E. N. (2013). *Alpha-2 adrenergic receptor activation and Ih channel blockade modulate fast network oscillations in the rodent prefrontal cortex in vitro.* 2013 Society for Neuroscience Meeting, San Diego, CA.

12. Sherfey, J. S., Yazdanbakhsh, A. (2012). *Fixational eye movements increase acuity in a retinal Bipolar-Amacrine-Ganglion circuit model.* 2012 Society for Neuroscience Meeting, New Orleans, LA.

13. Adams, N., Sherfey, J. S., LeBeau, F. E. N., Whittington, M. A., Kopell, N. J. (2012). *Prolonged decay time for GABA$_A$ receptor-mediated inhibition promotes abnormal interlaminar communication: Implications for altered cortical dynamics in schizophrenia.* 2012 Society for Neuroscience Meeting, New Orleans, LA.

14. Sherfey, J. S., Cash, S., Dehghani, N., Halgren, E. (2010). *Are human cortical slow oscillations during NREM sleep traveling waves or are they synchronized across the cortex?* 2010 Society for Neuroscience Meeting, San Diego, CA.

15. Tuan, A., Cash, S., Eskandar, E., Schomer, D., Sherfey, J., Halgren, E. (2010). *Cortical connectivity and synchrony in human intracranial recordings of sleep spindles.* 2010 National Institute of Biomedical Imaging and Bioengineering Training Grantees Meeting, Bethesda, MD.

16. Travis, K., Ellis, E., Leonard, M., Curran, M., Garvin, A., Sherfey, J., Halgren, E., Evans, J., Elman, J. (2010). *Investigation of N400m brain activity in an 18 month old infant at risk for Specific Language Impairments using anatomically constrained magneto-encephalography (aMEG).* 2010 Symposium on Research in Child Language Disorders, Madison, WI.

17. Travis, K., Ellis, E., Curran, M. M., Garvin, A. N., Leonard, M. K., Sherfey, J., Evans J. L., Halgren, E., Elman, J. (2010). *N400m-like Activity to Auditory Words Observed in 14 to 18 Month old Infants With Varying Language Abilities.* 2010 International Society for Infant Studies, Baltimore, Maryland.

18. Halgren, E., Ulbert, I., Sherfey, J., Dehghani, N., Tuan, A., Irimia, A., Cash, S. (2010). *Divergences between MEG and EEG during sleep rhythms: Neurobiology and biophysics.* 2010 Biomag International Conference on Biomagnetism, Dubrovnik, Croatia.

19. Kovacevic, S., Azma, S., Sherfey, J., Sheldon, S., Irimia, A., Marinkovic, K. (2010). *Effects of alcohol on cognitive control: MEG analysis in temporal and spectral domains*. 2010 Biomag International Conference on Biomagnetism, Dubrovnik, Croatia.

20. Kovacevic, S., Azma, S., Sherfey, J., Sheldon, S., Irimia, A., Halgren, E., Marinkovic, K. (2010). *Alcohol modulates oscillatory activity during cognitive control: Anatomically-constrained magnetoencephalography.* 2010 Society for Neuroscience Meeting, San Diego, CA.

21. McDonald, C. R., Thesen, T., Carlson, C., Blumberg, M., Girard, H. M., Trongnetrpunya, A., Sherfey, J., Devinsky, O., Kuzniecky, R., Cash, S., Leonard, M. K., Hagler, D. J., Jr., Dale, A. M., & Halgren, E. (2010). *Multimodal imaging of repetition priming: Using fMRI, MEG, and intracranial EEG to reveal spatiotemporal profiles of word processing*. 2010 International Society for Magnetic Resonance in Medicine Meeting, Stockholm, Sweden.

22. Sherfey, J., Mecklenborg, J., Lobdell, N., Reynolds, A., Baudenbacher, F., Wikswo, J. (2007). *Force Displacement Measurements Using Magnetic Tweezers to Investigate the Role of E-Cadherins in Cell-Cell Adhesion.* 2007 Biomedical Engineering Society Annual Fall Meeting, Los Angeles, CA.

23. Sherfey, J. (2007). *Magnetic Tweezer System Development.* Poster presented at the Annual Workshop on Building Mathematical Models of Cancer Across Biological Scales of the Vanderbilt Integrative Cancer Biology Center, Vanderbilt University, Nashville, TN.

24. Sherfey, J., Irimia, A., Shanahan, P., Lobdell, N., Reynolds, A., Baudenbacher, F., Wikswo, J. (August 2005). *Investigating the role of E-Cadherins in cell-cell adhesion using magnetic tweezers and particle tracking algorithms.* Poster presented at the Summer Research Fellowship Poster Session, Biomedical Engineering, Vanderbilt University, Nashville, TN.